

# Synthesis of novel 5- $\{[2-(4\text{-fluorobenzyl})-6\text{-arylimidazo}[2,1\text{-}b][1,3,4]\text{thiadiazol-5-yl}\}$ methylene}thiazolidine-2,4-diones as potent Antidiabetic agents

Naveen P.Badiger  
Department of Chemistry,  
Karnatak University  
Dharwad, 580003. Karnataka,  
India

N Shashidhar  
Department of Chemistry,  
Karnatak University  
Dharwad, 580003. Karnataka,  
India

Praveen N Vaidya  
Department of Chemistry,  
Karnatak University  
Dharwad, 580003. Karnataka,  
India

---

## Abstract

A series of novel 5-[2-(4-fluorobenzyl)-6-aryl-imidazo[2,1-b][1,3,4]thiadiazol-5-ylmethylene] thiazolidine-2,4-dione derivatives (4a-d) were synthesized. These final compounds (4a-d) were synthesized by Knoevenagel condensation of 2-(4-fluorobenzyl)-6-arylimidazo[2,1-b][1,3,4]thiadiazole-5-carbaldehydes (3a-d) with thiazolidine-2,4-dione. All the newly synthesized compounds were screened for their *in vivo* hypoglycemic and hypolipidemic activity in male Wistar rats. The Structures of all the newly synthesized compounds were established by analytical and spectral data.

**Keywords :** Imidazothiadiazoles, Thiazolidinediones, Hypoglycemic activity, Hypolipidemic activity, Antidiabetic agents.

---

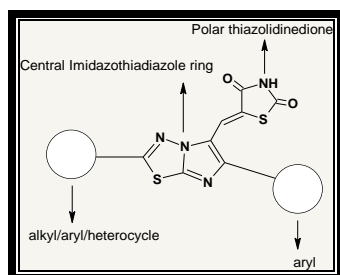
## 1. INTRODUCTION

Thiazolidinediones (TZDs) also known as glitazones, bind to PPAR $\gamma$ , a type of nuclear regulatory protein involved in transcription of genes regulating glucose and fat metabolism. These PPARs act on peroxysome proliferator responsive elements (PPRE). The PPREs influence insulin-sensitive genes, which enhance production of mRNAs of insulin-dependent enzymes. The final result is better use of glucose by the cells. Imidazo[2,1-b][1,3,4]thiadiazole derivatives have attracted the interest of medicinal chemists for many years because of their diverse pharmacological properties such as anticancer[1], antitubercular[2], antibacterial[3], antifungal [4], anticonvulsant, analgesic[5] and antisecretory[6] activities. They have been reported to selectively inhibit several therapeutic receptors and enzymes, extending their applications in modern drug

design. Further, there are reports in the literature about the antidiabetic activity of the derivatives containing thiadiazole ring system[7].

Thiazolidinedione moiety is significant because of its pharmacophoric acidic group in a central flat ring. Structure activity relationship studies have revealed that better activity can be gained by linking a lipophilic fragment such as aromatic/heteroaromatic ring via one or two carbon atom spacer at C<sub>5</sub>-position of the thiazolidinedione moiety. Hence it is proposed to synthesize various thiazolidinedione derivatives by substituting pharmacophorically important group and as a lipophilic fragments like imidazothiadiazoles. Such molecules are expected to exhibit better antidiabetic properties for non-insulin dependent diabetes mellitus (NIDDM) as cited in the literature.

**Fig.1: Representation of designed prototype structure.**



## 2.RESULTS AND DISCUSSION

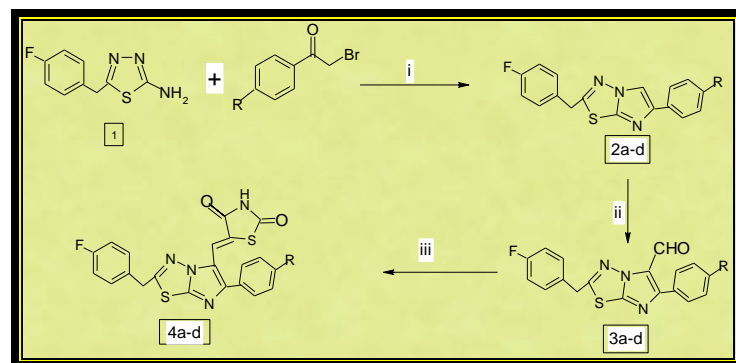
During the present investigation required imidazo[2,1-*b*][1,3,4]thiadiazoles were prepared by the reaction of 2-amino-1,3,4-thiadiazole (**1**) with appropriately substituted  $\alpha$ -haloketones (phenacylbromides) in dry ethanol as hydrobromides, which on neutralization with aqueous sodium carbonate solution gave corresponding free bases (**2a-d**) in good yields. The absence of  $\nu_{N-H}$  band in IR spectra of the resulting compounds confirms the formation of product, which exhibits imidazole ( $C_5-H$ ) proton in the region  $\delta$  7.96-8.31 in  $^1H$  NMR spectra.

Imidazo[2,1-*b*][1,3,4]thiadiazoles (**2a-d**) were further subjected to Vilsmeier Haack reaction, which resulted in the formation of expected imidazo[2,1-*b*][1,3,4]thiadiazole-5-carbaldehydes (**3a-d**). The IR spectra of these compounds displayed the aldehydic carbonyl around  $1674cm^{-1}$  and  $\nu_{C-H}$  around  $2850cm^{-1}$ . The structures were further confirmed by the presence of a signal around  $\delta$  10.00 for aldehydic proton and absence of  $C_5-H$  of imidazole in the  $^1H$  NMR spectra apart from other aromatic protons.

The intermediate imidazo[2,1-*b*][1,3,4]thiadiazole-5-carbaldehydes (**3a-d**) were exploited for the preparation of target molecules (structure analogues of englitazone) by Knoevenagel condensation with thiazolidine-2,4-dione. The formation of 5-[(2-alkyl/aryl-6-aryl)imidazo[2,1-*b*][1,3,4]thiadiazol-5-yl)methylene]-1,3-thiazolidine-2,4-dione (**4a-d**) was confirmed by their IR spectra, which

displayed the  $\nu_{C=O}$  bands around  $1725$  and  $1690cm^{-1}$ . The  $\nu_{N-H}$  was observed in the region  $3112-3320cm^{-1}$ . Further, they were confirmed by  $^1H$  NMR spectra, where aldehydic proton disappeared and the vinylic proton resonated in the region  $\delta$  7.60-7.92 as a singlet. This series of compounds is characterized by the presence of one carbon atom spacer between thiazolidine-2,4-dione moiety and fused heterocyclic ring.

Newly synthesized compounds were analyzed for their C, H and N compositions and the values are within the allowed limits. All the newly synthesized compounds were screened for their hypoglycemic and hypolipidemic activities.



**a: R = Me, b: R = biphenyl, c: R = naphthyl, d: R = coumarinyl**

### Reagents and Conditions:

- Dry ethanol reflux, 18hr,  $Na_2CO_3$ .
- DMF/ $POCl_3$ ,  $Na_2CO_3$ .
- Piperidine acetate, toluene, reflux.

## 3.EXPERIMENTAL SCHEME

### 3.1. MATERIALS

All chemicals & reagents were purchased from Sigma-Aldrich Chemicals Pvt. Ltd India. Melting points were determined in open capillaries. The IR spectra were recorded on Nicolet Impact-FT-IR spectrophotometer, (Model-410, USA) using KBr pellet technique.  $^1H$ NMR experiments were performed on a 300 MHz Bruker AC-300F spectrometer (Model RX-300, Switzerland) using TMS as an internal standard in  $CDCl_3$ .

All chemical shifts were reported as  $\delta$  (ppm) values. All the newly synthesized compounds were analyzed for C, H, N and results were found to be within the range of  $\pm 0.4\%$  of the theoretical value.

### 3.2. METHODOLOGY

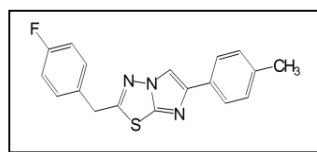
#### 3.2.1. Synthesis of 2-Amino-5-(4-fluorobenzyl)-1,3,4-thiadiazole (1)

**General method:** A mixture of 4-fluorophenylacetic acid (0.1mol) and thiosemicarbazide (9.113g, 0.1mol) in phosphorous oxychloride (30 mL) was refluxed gently for 45 min. The reaction mixture was cooled and quenched (highly exothermic) with cold water (90 mL). The resulting solution was refluxed for additional 4 hrs and filtered hot. The filtrate was cooled and basified with aqueous potassium hydroxide solution. The solid that separated was filtered, washed with water, dried and recrystallized from ethanol.

#### 3.2.2 Synthesis of 2-(4-alkyl/aryl)-6-arylimidazo[2,1-b][1,3,4]thiadiazoles : (2a-d)

**General method:** A mixture of equimolar quantities of 2-amino-5-(4-aryl)-1,3,4-thiadiazole (0.01 mol) and bromoacetyl compound (0.01 mol) was refluxed in dry ethanol for 18 hrs. The excess of solvent was distilled off and the solid hydrobromide salt that separated was collected by filtration, suspended in water and neutralized by aqueous sodium carbonate solution to get free base. It was filtered, washed with water, dried and recrystallized from suitable solvent.

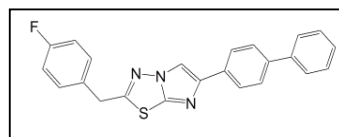
#### 2-(4-Fluoro-benzyl)-6-p-tolyl-imidazo[2,1-b][1,3,4]thiadiazole (2a)



Brown crystalline Solid (ethanol), yield 75%, m.p. 168-170°C; IR (KBr)  $\text{vcm}^{-1}$ : 3124, 2923, 2853, 1602, 1507;  $^1\text{H NMR}$  (300MHz,  $\text{CDCl}_3$ )  $\delta$ : 2.38 (s, 3H,  $\text{CH}_3$ ), 4.29 (s, 2H,  $\text{CH}_2$ ), 7.06-7.44 (m, 6H, Ar-H), 7.83 (d,  $J=7.2\text{Hz}$ , 2H, Ar-H), 7.98 (s, 1H,  $\text{C}_5\text{-H}$ ,

imidazole). Anal. calcd. for  $\text{C}_{18}\text{H}_{14}\text{FN}_3\text{S}$ : C, 66.85; H, 4.36; N, 12.99. Found: C, 66.81; H, 4.32; N, 12.92%.

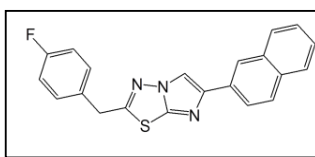
#### 6-Biphenyl-4-yl-2-(4-fluoro-benzyl)-imidazo[2,1-b][1,3,4]thiadiazole (2b)



White solid (ethanol), yield 80%, m.p. 223-225°C; IR (KBr)

$\text{vcm}^{-1}$ : 3015, 2856, 2816, 1604, 1506;  $^1\text{H NMR}$  (300MHz,  $\text{CDCl}_3$ )  $\delta$ : 4.29 (s, 2H,  $\text{CH}_2$ ), 7.16-7.49 (m, 11H, Ar-H), 7.76 (d,  $J=7.5\text{Hz}$ , 2H, Ar-H), 7.98 (s, 1H,  $\text{C}_5\text{-H}$ , imidazole). Anal. calcd. for  $\text{C}_{23}\text{H}_{16}\text{FN}_3\text{S}$ : C, 71.67; H, 4.18; N, 10.90. Found: C, 71.65; H, 4.17; N, 10.83%.

#### 2-(4-Fluoro-benzyl)-6-naphthalen-2-yl-imidazo[2,1-b][1,3,4]thiadiazole (2c)

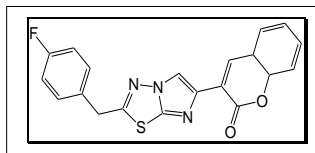


Yellow crystalline solid (ethanol), yield 64%, m.p. 212-214°C; IR (KBr)  $\text{vcm}^{-1}$ : 3107,

2924, 2854, 1603, 1524, 1501;  $^1\text{H NMR}$  (300MHz,  $\text{CDCl}_3$ )  $\delta$ : 4.31 (s, 2H,  $\text{CH}_2$ ), 7.09-7.66 (m, 10H, Ar-H), 8.1 (s, 1H,  $\text{C}_5\text{-H}$ , imidazole), 8.31 (s, 1H,  $\text{C}_1\text{-H}$ , naphthalene). Anal. calcd. for  $\text{C}_{21}\text{H}_{14}\text{FN}_3\text{S}$ : C, 70.18; H, 3.93; N, 11.69. Found: C, 70.12; H, 3.88; N, 11.68%.

#### 3-[2-(4-Fluoro-benzyl)-imidazo[2,1-b][1,3,4]thiadiazol-6-yl]-4a,8a-dihydro-chromen-2-one (2d)

White needles (ethanol), yield 75%, m.p. 151-153°C; IR (KBr)  $\text{vcm}^{-1}$ :



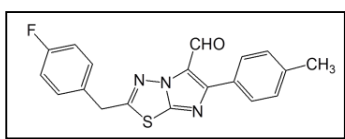
3010, 2834, 2812, 1718, 1610, 1509;  $^1\text{H NMR}$  (300MHz,  $\text{CDCl}_3$ )  $\delta$ :

4.26 (s, 2H,  $\text{CH}_2$ ), 6.93-7.04 (m, 4H, Ar-H), 7.30 (d,  $J=7.6\text{Hz}$ , 2H, Ar-H), 7.74 (d,  $J=8.2\text{Hz}$ , 2H, Ar-H), 8.24 (s, 1H,  $\text{C}_4\text{-H}$ , coumarin), 8.66 (s, 1H,  $\text{C}_5\text{-H}$ , imidazole); Anal. calcd. for  $\text{C}_{20}\text{H}_{14}\text{FN}_3\text{O}_2\text{S}$ : C, 63.31; H, 3.72; N, 11.08. Found: C, 63.30; H, 3.66; N, 11.03%.

### 3.2.3. Synthesis of 2-(4-fluorobenzyl)-6-arylimidazo[2,1-b][1,3,4]thiadiazole-5-carbaldehydes (3a-d):

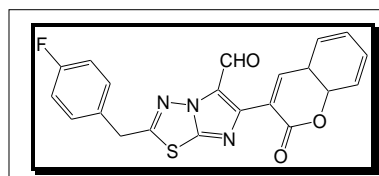
**General method:(Vilsmeier Haack reaction):** Vilsmeier Haack reagent was prepared by adding phosphorous oxychloride (3mL) in dimethylformamide (20mL) at 0°C with stirring. At the same temperature 2-(4-fluorobenzyl)-6-arylimidazo[2,1-b][1,3,4]thiadiazole, (2a-d) (0.01mol) was added to the reagent and stirred at 0-5°C for 30 minutes. The mixture was further stirred for 2 hrs at room temperature and then at 60°C for additional 2 hrs. The reaction mixture was cooled in ice water bath and quenched with water(5mL). The reaction mixture was basified with aq. sodium carbonate (10%) solution with cooling and further stirred at 80-90°C for 2 hrs. After cooling, the mixture was diluted with water, extracted with chloroform (30mLx3). The combined extracts were washed with water (100mLx3), dried over anhydrous sodium sulphate. Solvent was removed by evaporation and solid obtained was recrystallized from suitable solvent to afford colorless to pale yellow crystals in excellent yields.

#### 2-(4-fluoro-benzyl)-6-*p*-tolyl-imidazo[2,1-b][1,3,4]thiadiazole-5-carbaldehyde (3a).



Brown solid (Chloroform), Yield 90%, m.p.165°C; IR (KBr)  $\nu$   $\text{cm}^{-1}$ : 2923, 1512, 1683;  $^1\text{H}$  NMR (300MHz,  $\text{CDCl}_3$ )  $\delta$ : 2.23(s, 3H,  $\text{CH}_3$ ), 4.41(s, 2H,  $\text{CH}_2$ ), 6.9-7.84 (m, 8H, Ar-H), 10.02(s, 1H, CHO); Anal. Calcd. for  $\text{C}_{19}\text{H}_{14}\text{FN}_3\text{OS}$ ; C, 64.94; H, 4.02; N, 11.96%. Found: C, 64.90 ; H, 4.01; N, 11.91%.

#### 2-(4-fluoro-benzyl)-6-(2-oxo-4a,8a-dihydro-2H-chromen-3-yl)-imidazo[2,1-b][1,3,4]thiadiazole-5-carbaldehyde (3d).



White needles (ethanol), yield 86%, m.p. 175-176°C; IR (KBr)  $\nu\text{cm}^{-1}$ : 2834, 2923, 1712, 1678, 1513;  $^1\text{H}$  NMR (300MHz,  $\text{CDCl}_3$ )  $\delta$ : 4.4 (s, 2H,  $\text{CH}_2$ ), 6.93-7.04 (m, 4H, Ar-H), 7.30 (d, =7.6Hz,

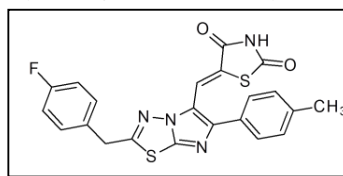
2H, Ar-H), 7.74 (d,  $J=8.2\text{Hz}$ , 2H, Ar-H), 8.34 (s, 1H, C4-H, coumarin), 10.20 (s, 1H, CHO); Anal. calcd. for  $\text{C}_{21}\text{H}_{14}\text{FN}_3\text{O}_3\text{S}$ : C, 61.91; H, 3.46; N, 10.31. Found: C, 61.90; H, 3.41; N, 10.30%.

#### 3.2.4. Synthesis of 5-[[2-(4-alkyl/aryl)-6-arylimidazo[2,1-b][1,3,4]thiadiazol-5-yl]methylene]-1,3-thiazolidine-2,4-dione. (4a-d)

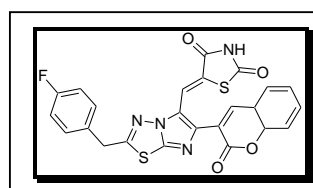
**General method:** A mixture of 2-alkyl/aryl-6-arylimidazo[2,1-b][1,3,4]thiadiazole-5-carbaldehyde (0.001mol) and 1,3-thiazolidine-2,4-dione (0.001mol) was refluxed in toluene (25mL) with catalytic amount of piperidine-acetate for 2 hrs. The yellow solid separated was collected by filtration, washed with hot benzene and methanol. The products were recrystallized from dimethylformamide.

#### 5-[2-(4-fluorobenzyl)-6-*p*-tolyl-imidazo[2,1-b][1,3,4]thiadiazol-5-ylmethylene] thiazolidine-2,4-dione (4a).

yellow granules (DMF), yield 95%, m.p. 295-296°C; IR (KBr)  $\nu\text{cm}^{-1}$ : 3016, 2859, 2817, 1722, 1603, 1504;  $^1\text{H}$  NMR (300MHz,  $\text{DMSO}, d_6$ )  $\delta$ : 2.34 (s, 3H,  $\text{CH}_3$ ), 4.34 (s, 2H,  $\text{CH}_2$ ), 7.31-7.76 (m, 6H, Ar-H), 7.88(d,  $J=7.6\text{Hz}$ , 2H, Ar-H), 7.96 (s, 1H, vinylic proton), 12.20 (s, 1H, NH,  $\text{D}_2\text{O}$  exchangeable), Anal. calcd. For  $\text{C}_{22}\text{H}_{15}\text{FN}_4\text{O}_2\text{S}_2$ : C, 58.65; H, 3.36; N, 12.44. Found: C, 58.63; H, 3.32; N, 12.41%.



#### 5-[2-(4-fluoro-benzyl)-6-(2-oxo-4a,8a-dihydro-2H-chromen-3-yl)-imidazo[2,1-b][1,3,4]thiadiazol-5-ylmethylene]-thiazolidine-2,4-dione (4d).



yellow granules (DMF), yield 85%, m.p. >300°C; IR (KBr)  $\nu\text{cm}^{-1}$ : 3016, 2859, 2817, 1722, 1603, 1504;  $^1\text{H}$  NMR (300MHz,  $\text{DMSO}, d_6$ )  $\delta$ : 4.4 (s, 2H,  $\text{CH}_2$ ), 6.93-7.04 (m, 4H, Ar-H),

7.30 (d,  $\tau$ =7.6Hz, 2H, Ar-H), 7.74 (d,  $J$ = 8.2Hz, 2H, Ar-H), 7.96 (s, 1H, vinylic proton), 8.34 (s, 1H, C<sub>4</sub>-H, coumarin), 12.24 (s, 1H, NH, D<sub>2</sub>O exchangeable). Anal. calcd. for C<sub>24</sub>H<sub>15</sub>FN<sub>4</sub>O<sub>4</sub>S<sub>2</sub>: C, 56.91; H, 2.98; N, 11.06. Found: C, 56.90; H, 2.91; N, 11.01%.

#### 4. PHARMACOLOGICAL EVALUATIONS.

##### 4.1. Hypoglycemic & hypolipidemic activities.

Male Wister rats weighing 150–200 g were used for this study. All animals were maintained under 12 h light and 12 h dark cycle at 25±1°C. All animals were given standard chow (National Institute of Nutrition, India) and water ad libitum. The experiments were designed and conducted in accordance with the guidelines of institutional animal's ethics committee. The acclimatized animals were kept fasting for 24 h with water ad libitum and alloxan monohydrate (120 mg/kg) in normal saline was then administered. Serum glucose level was checked after 72 h. Animals with serum glucose levels >250 mg/dL were considered diabetic and were used for the study. The animals were divided into two groups of six animals each. Group I animals were termed as control or untreated and group II animals were termed as treated. Group II animals were administered with compounds to be screened for euglycemic effect. The suspension of the compound was prepared in water with 1% carboxy methyl cellulose as suspending agent. All the test compounds were orally administered at different doses (10, 30, 100 mg/kg) for 15 days. Pioglitazone was used as standard drug.

On the final day, the blood samples were collected from the tail vein. Plasma was separated from whole blood of each group by centrifugation. Plasma glucose (PG) and triglyceride (TG) levels were estimated using commercial kit [8].

**Table 1: Plasma glucose (PG) level of 4a–d at various drug doses**

Compound	% Decrease in plasma glucose level (PG) at various drug doses (mg/kg bodyweight)		
	10 mg	30 mg	100 mg
Pioglitazone	47.25 ± 5.50	64.59±5.42	75.43±3.40
4a	20.15±1.14	21.78±2.25	22.41±2.36
4b	32.25±3.14	46.68±3.89	56.47±2.96
4c	42.48±3.25	62.24±3.42	70.35±3.14

4d	45.42±1.25	58.36±2.36	68.42±2.16
----	------------	------------	------------

Each value represents the mean ± SEM (n = 6). Percentage reduction was calculated according to the formula:  

$$\frac{[(\text{PG in control} - \text{PG in treated})/\text{PG in control}] * 100}{[(\text{TG in control} - \text{TG in treated})/\text{TG in control}] * 100}$$

**Table 2: Triglyceride (TG) level of 4a–d at various drug doses**

Compound	% Decrease in triglyceride level (TG) at various drug doses (mg/kg body weight)		
	10 mg	30 mg	100 mg
Pioglitazone	35.25± 20.42	40.96 ± 17.59	45.89± 2.24
4a	25.75± 12.32	26.32 ± 11.41	25.89± 1.14
4b	27.79± 18.32	30.32 ± 13.41	39.29± 1.87
4c	33.48±19.24	38.62±16.48	42.28±2.19
4d	32.68±12.36	36.14±14.98	39.45±2.14

Each value represents the mean ±SEM (n = 6). Percentage reduction was calculated according to the formula:  

$$\frac{[(\text{PG in control} - \text{PG in treated})/\text{PG in control}] * 100}{[(\text{TG in control} - \text{TG in treated})/\text{TG in control}] * 100}$$

#### 5. CONCLUSIONS

Thiazolidinediones (TZDs) with naphthyl & coumarinyl substitution ie 5-[2-(4-fluorobenzyl)-6-naphthelen-imidazo[2,1-b][1,3,4]thiadiazol-5-ylmethylene] thiazolidine-2,4-dione (**4c**), 5-[2-(4-fluoro-benzyl)-6-(2-oxo-4a,8a-dihydro-2H-chromen-3-yl)-imidazo[2,1-b][1,3,4]thiadiazol-5-ylmethylene]-thiazolidine-2,4-dione (**4d**) exhibited promising hypoglycemic & hypolipidemic activity.

#### 6. REFERENCES

- [1] Terzioglu N., Gursoy A. (2003) Synthesis and anticancer evaluation of some new hydrazone derivatives of 2,6-dimethylimidazo[2,1-b][1,3,4]thiadiazole-5-carbohydrazide. *Eur J Med Chem*; 38:781–786.
- [2] Gadad A.K., Noolvi M.N., Karpoomath R.V. (2004) Synthesis and antitubercular activity of a series of 2-sulfonamido/trifluoromethyl- 6-substituted imidazo[2,1-b]-1,3,4- thiadiazole derivatives. *Bioorg Med Chem*; 12:5651–5659.
- [3] Gadad A.K., Mahajanshetti C.S., Nimbalkar S., Raichurkar A. (2000) Synthesis and antibacterial activity of some 5-guanylhydrazone/thiocyanato-6-arylimidazo [2,1-b]- 1,3,4-thiadiazole-2-sulfonamide derivatives. *Eur J Med Chem*; 35:853–857.
- [4] Andotra C.S., Langer T.C., Kotha A. (1997) Synthesis and antifungal activity of some substituted 1,3,4-

thiadiazolo[3,2-a]-s-triazin-5-phenyl-7-thiones and imidazo-[2,1-b]-1,3,4-thiadiazol-5-ones. *J Indian Chem Soc*; 74:125–127.

[5] Khazi I.A.M., Mahajanshetti C.S., Gadad A.K., Tarnalli A.D., Sultanpur C.M. (1996) Synthesis, anticonvulsant and analgesic activities of some 6-substituted imidazo [2,1-b][1,3,4]thiadiazole-2-sulfonamides and their 5-bromo derivatives. *Arzneimittel-Forschung/DrugRes*; 46:949–952.

[6] Andreani A., Leonia A., Locatelli A., Morigi R., Rambaldi M., Simon W.A., Senn-Bilfinger J. (2000) Synthesis and antisecretory activity of 6-substituted 5-cyanomethylimidazo[2,1-b]thiazoles and 2,6-dimethyl-5-hydroxymethylimidazo[2,1-b][1,3,4]thiadiazole. *Arzneimittel/Drug Res*; 50:550–553.

[7] Avetisyan A.Kh., Ovsepyan T.R., Stepanyan N.O., Sapondzhyan L.G. (1981) Synthesis and hypoglycaemic activity of sulfonamido-1,3,4-thiadiazoles. *Pharm Chem J*;15:416–418.

[8] Hugget A., Nixon D.A. (1957) Use of glucose oxidase, peroxidase, and O-dianisidine in determination of blood and urinary glucose. *The Lancet*; 270:368–370.

# Creative Economic Building Components For Low-Income Housing

Basil Kamel, PhD

Professor of Architecture and Urban Theory  
American University in Cairo  
Cairo, Egypt

Moaz Mohamed

Practicing Architect  
Cairo, Egypt

**Abstract:** When observing Egypt's method of expansion, one can identify a clear language and distinctive pattern of urban development. The years following 1952, marked by the privatization of agricultural land and the population boom, gave rise to a soon to be urban 'catastrophe'. In order to fulfil the needs of the growing population, buildings were sprouting out everywhere, causing agricultural lands to disappear under a jungle of red bricks, erasing the lines between urban and rural. This phenomenon of informal expansion has spread across the country composing what is commonly known as *Ashwa'eeyat* or informal settlements. In Egypt, these can be identified by a unified method of construction using concrete skeleton structures of concrete slabs and beams along with plain red brick walls; an appearance that does not reflect nor shed light on the Egyptian culture or environmental requirements. The use of bricks and concrete is due to the fact that this construction method is the most commonly used and feasible type of construction; the material is available, the workmanship, even though it is not the most economic method. Egypt is a developing country that possesses numerous resources, being both tangible and intangible ones. The aim of this paper is to research and determine the possibility of creating different elements of construction utilizing available resources and recycling waste material. These elements would be economic and reflective of the Egyptian culture while maintaining the necessary environmental and physical safety requirements sought in residential buildings.

**Keywords:** recycled materials; alternative wall; construction waste; informal; economic construction alternative

## 1. INTRODUCTION

Analyzing the informal urban fabric at the fringes of the city of Cairo, a significant sense of physical uniformity is apparent due to the use of specific materials and construction systems. The use of exposed red bricks with skeleton type concrete structures is the norm of construction although these materials and construction methods are non-economic and do not satisfy environmental requirements (Figure 1 & Figure 2). There are very little studies that address potential of recycling waste material for environmental solutions and as means to enhance economic vitality for community development on the one hand, and better define local identity on the other (MOPIC, 2004).



Figure 1. Informal Settlements of Izbet Khayralla.



Figure 2. Informal Settlements of Dar El Salam.

Figure 3 illustrates that Cairo is considered one of the major concentrations for slums and dilapidated communities (Abu-Lughod & Sims, 2010). Approaches for development and providing for housing should involve creative models that address the resources and potentials of these communities (Revedin, 2012). By identifying these potentials; be they tangible (natural, physical resources such as materials, site conditions, etc..) or intangible ones (craftsmanship, etc..) one can achieve creative models of development. This paper aims to develop creative new wall construction through the use of available resources and recycled waste materials both from the potentials of a local community (taken as a case study) and the nation resources. This model, as developed, shall serve as an exemplary process aimed to be repeated around the country. It shall re-enforce connection at a socio-cultural

level through the use of existing resources on the ground of mutual benefit and collaborative work.

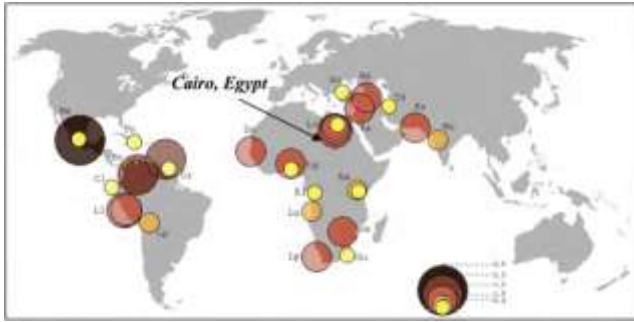


Figure 3. Figure illustrating the 30 mega slums of the world with Cairo amongst the top ranked.

A community site at Khaya-la lying in Fustat area was chosen as the case study. The variable sub-communities within this site possess resources (represented in man power/people, waste bi products and craftsmanship) that gear towards developing a potential economic creative model for building materials concentrating on new wall systems. It also aims to involve the local community through empowerment and raising awareness of potentials for socio-economic development (GIZ & KFW, 2012).

The Khayala site's activity patterns generate a significant amount of wasted bi products that could be otherwise the key to develop alternative construction material (Figure 4). On one hand, AlKhayala site is a zone containing stone workshops that work with Sandstone, Basalt and granite, which are handcrafted to produce various types of wall claddings, flooring and ornamentation. The workers sell the stone they hand carve and craft while disposing all the waste stone out of the site after paying a fee for each loading. On the other hand, there exists a large supply of materials within the nation that are not used to their fullest potential such as palm fronds and rice husk (Jahromi et al, 2007). In fact, a large amount of rice husk is burnt every year by peasants and farmers because they consider it useless (Razavi, 2005).



Figure 4. Waste basalt, sandstone and granite located on site

The basic hypothesis of this research assumes that by conducting research about the different available practices of material use and the potentials born from recycled waste materials both at the level of the community and nationwide, the design and creation of alternate wall components could be proposed. This shall substitute the existing dominant language

(or system) of facades in most informal neighborhoods of Cairo and Egypt, and thus creating a new system that could be a seed for a new socio-cultural local identity. The component is considered one of the approaches of development within a wider scope project, attempting to alter the present schemes, while reviving and redefining tomorrow's heritage.

## 2. METHODOLOGY

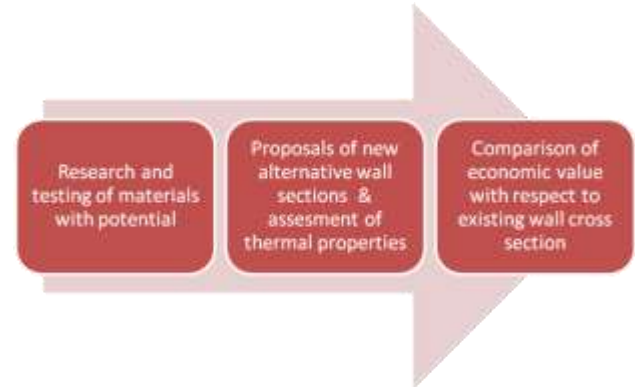


Figure 5. Diagram of methodology (researchers)

The research relied on both a literature review and empirical studies to identify the potentials and material resources and types available in the community. A process of material identification was conducted in order to highlight the strengths, features, characteristics and weaknesses of each material; information such as availability, material strength, source and potentials. This process of identification relied on ASTM standard test methods results.

Based on this information, new alternatives and wall components with the use of waste material identified from different locations and sources were proposed. The proposal phase included the assessment of the wall sections' thermal properties to ensure their physical and environmental qualities. The final phase involved an economic analysis comparing the wall sections with respect to the dominant brick wall commonly used in Egypt. This was conducted to assess the feasibility, economic significance and tendency of the wall components to contend within the local market, especially in informal areas.

## 3. MATERIAL IDENTIFICATION

### 3.1 Briefing

In this sector, the process of identifying the material will take place, revealing the following components:

- Sources of material
- Quantity of material
- Potentials of material
- Properties and features (through research and testing (ASTM))
- Treatments (if required).

### 3.2 Characteristics and Features

#### 3.2.1 Stone

Each workshop on the premises of the site produces a daily average of 350 kg of waste stone. There are 120 different workshops within the site. There are 55 workshops working with basalt, 40 workshops working with Sandstone and 25

workshops working with granite. The site produces an average of 1,260,000 kg (1,340 tons) of waste stone monthly. The stone located on the site is of various types, including Basalt, granite and sandstone (locally known as 'Hashmi').

### 3.2.2 Basalt

Basalt is a dark-colored, fine-grained, igneous rock composed mainly of plagioclase and pyroxene minerals (Subramanian, 2010). Basalt is used as a finishing material embedded on building facades and as finishing material for road networks in high-end residential compounds and districts.

#### Properties - Testing results:

ASTM C 97-02, standard test method for, "Absorption and Bulk, Specific Gravity of Dimension stone"

ASTM C 170-99, standard test method for "Test for Compressive strength of Dimension stone", Dry conditions

ASTM C 99-2000, Standard test method for "Test for Modulus of Rupture of Dimension stone ", Wet Conditions

Table 1. Standard Specification for Basalt Dimension Stone

Compressive strength (n/mm <sup>2</sup> )	Bulk specific Gravity	Water absorption (%)	Modulus of Rupture (n/mm <sup>2</sup> )
108.2	2.7	0.71	20.26

### 3.2.3 Granite

Granite is a light-colored igneous rock with grains large enough to be visible with the unaided eye. Granite is mainly composed of quartz and feldspar. This mineral composition usually gives granite a red, pink, gray or white color with dark mineral grains visible throughout the rock (Robertson, 1988).

#### Properties - Testing results:

ASTM C615 / C615M

Table 2. Standard Specification for Granite Dimension Stone

Compressive strength (n/mm <sup>2</sup> )	Bulk specific Gravity	Water absorption (%)	Modulus of Rupture (n/mm <sup>2</sup> )
131	25	0.40	10.32

### 3.2.4 Sandstone

Sandstone is a sedimentary rock composed of sand-sized grains of mineral, rock or organic material. It also contains a cementing material that binds the sand grains together and may contain silt sized particles that occupy the spaces between the sand grains. Sandstone is often mined for use as a construction material or as a raw material used in manufacturing (Torabi, 2013).

#### Properties - Testing results:

ASTM C616 / C616M

Table 3. Standard Specification for Sandstone Dimension Stone

Compressive strength	Bulk specific	Water absorption	Modulus of

(n/mm <sup>2</sup> )	Gravity	(%)	Rupture (n/mm <sup>2</sup> )
34	3	4	2.91

### 3.2.5 Rice Husk

An available resource widely spread within Egypt specifically within Upper Egypt. Every year, the peasants tend to burn the rice husk into ashes, creating a much-polluted environment. The rice husk is known for its high thermal performance and insulation (Ramezianpour, 1997). It needs to be cured and compressed in order to form usable sheets to be implemented for different uses (Ramezianpour, 2009).



Figure 5. Rice husk is extensively present in Lower Egypt agricultural areas



Figure 6. Rice husk unused and burnt by peasants and farmers

### 3.2.6 Palm Fronds

Egypt is ranked the second worldwide country possessing date palm trees. Around 7,000,000 palm trees are located within the country carrying a large amount of palm fronds. The fronds have been used for years in Upper Egypt for various components and tools. Palm fronds are characterized to be extremely strong, fiber based and durable. It is a widely available and renewable material that has great potentials. This material has been used to produce furniture and containers due to its physical traits but was never pushed further until lately (Suryawanshi, 2013).



Figure 7. Palm fronds being fabricated to small containers in Upper Egypt

### 3.3 Analytical Review

After the process of material identification, it could be concluded that the nation possesses a large quantity and supply of material that is considered waste, however it is not used efficiently. In order to put these materials to good use, a process of empowering and tutoring of people is required, in order for them to understand the 'know how' of using the material and the connections or sources required in order to attain the material (GIZ 2, 2012). The rice husk, stones of different types and the fronds are concluded to have strong insulating properties (Bowman et al, 1992, & Marthong, 2012 & Robertson, 1988). They could be used as filling material or layers in the process of wall creation to attain good thermal conductivity features.

The Basalt and granite have proven to have high compressive strength, feasibly qualifying them to be used as structural components (Hamadallah, 2008 & Sosna, 2013). The palm fronds is a material of very interesting features that could be used in a variety of methods; it has proven to have high compressive strength and a relatively low weight in addition to it being a fiber based component that could be easily manipulated and shaped (Shamsi, 2009).

After understanding the materials and their properties, we work to identify the possible configurations that would assemble wall sections of adequate properties and features.

Proposal 1 is a wall that is composed of palm fronds, rice husk and stone that attempts to produce a lightweight wall that could be used to envelope auxiliary functions and temporary structures.

Proposal 2 is a building block that is composed of stone, rice husk and cement in an attempt to replace the red brick with a building block of higher performance (Mehta, 2004), and has an aesthetical and cultural value represented in the use of stone and the appearance of the block configuration.

Proposal 3 is a decorative component referred to as stone paste and is used to form various shapes due to its fluidity

prior to hardening, and is composed of cement, gypsum and waste crushed stone.

### 3.4 Wall Sections Proposed

#### 3.4.1 Proposal 1- Palm fronds, rice husk and stone

The first proposed wall section uses a combination of the waste stone material located on site along with the use of palm fronds from Upper and Lower Egypt, PVC waste pipes from industrial facilities in 6<sup>th</sup> October city and rice husk from Lower Egypt. The idea is to use the palm fronds and stone as a replacement to reinforced steel bars implemented in structural concrete columns since the basalt stone and granite have a high compressive strength and the palm fronds attain 85% the strength of reinforced steel, making huge savings on cost which will be analyzed later on in the paper. The idea is to create and pour a strong base to the structural column using concrete filled with waste stone aggregates of large sizes while a PVC pipe is imbedded in its core, rising up as a core for the column. The column would then have stone of smaller sizes placed into it with the addition of cement mortar to create a strong column structure. After that the palm fronds will be fabricated and manipulated to create wall outer shells with no filling on the inside. The columns should be maximum 2m apart from each other for issues regarding bracing and lateral stability. The shells will be totally solid and will act as a container. The waste stone material on the other hand after being broken to smaller sizes will be used as the insulating filling material between the interior and exterior palm fronds wall shells.

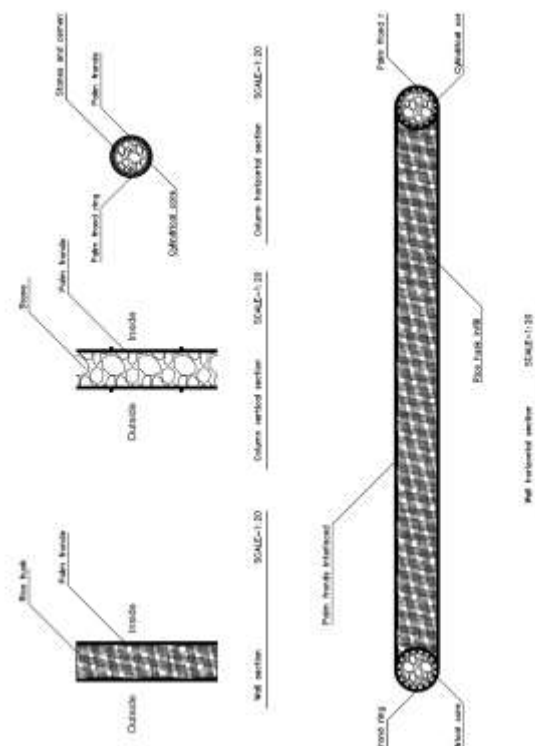


Figure 8. Design details of proposal 1

### 3.4.1.1 Implementation and Construction Methods

#### Steps of implementation

##### Column construction

1. Cut the palm fronds and categorize the different cross sections
2. Add strands of palm fronds and tie to the extruding palm fronds from the column foundation (Ashayer)
3. Use a waste PVC pipe of 10 cm radius or so to act as the core of the column
4. Pour concrete into the PVC core with palm fronds (Ones that have tied with the foundation)
5. Use the thick (highest strength) portion of the palm fronds to encircle the core and tie a strand of the lighter fronds to hold them all together.

##### Wall construction

1. Prepare and work on the intertwining of palm fronds together to create large span palm fronds
2. Use the large span strands to wrap the fronds around the columns
3. Apply several layers ensuring there are no hollow openings between the strands
4. Pour the stone into the shell of palm fronds between two columns.

### 3.4.1.2 Thermal Conductivity

U-Value (W/m <sup>2</sup> .K):	0.120
Admittance (W/m <sup>2</sup> .K):	1.190
Solar Absorption (0-1):	0.531
Visible Transmittance (0-1):	0
Thermal Decrement (0-1):	0.07
Thermal Lag (hrs):	5
[SBEM] CM 1:	0
[SBEM] CM 2:	0
Thickness (mm):	450.0
Weight (kg):	92.000

Figure 9. Ecotect results for Proposal 1 wall section  
The proposed wall section has been built and formulated on Autodesk Ecotect, an analysis sustainable building design software that offers building energy analysis tools for architects. The material was tested to attain the thermal conductivity and properties of the proposed wall section being:

- **U-value:** Measure of heat loss
- **Admittance:** Material's ability to absorb and release heat from a space
- **Solar absorption:** Amount of solar energy absorbed by wall that is neither reflected nor transmitted
- **Thermal lag:** Materials required time to add or remove heat from a mass before it reaches the design set point temperature

Analyzing proposal 1, it could be established that the wall section has a relatively low U-value and admittance of 0.12 due to the very high use of rice husk as a filling material of the wall's core; it has relatively high insulating properties (Zhang & Malhotra, 1996). The wall was also able to achieve a neutral solar absorption ratio of 0.531 and a thermal lag of 5 hours. The wall could be characterized to be light weighted and a very suitable wall component for the construction of light structures. This is due to the limitations of both the palm fronds and the rice husk that are expected to decay within a certain time frame and will need replacement.

### 3.4.2 Proposal 2- Stone Block

The second proposed wall section intends to introduce a building block composed of stone waste, rice husk and cement. The idea is to design a building block to replace the red bricks being used today by a stronger and a more environmental building block. The block will be designed to contain waste stone blocks ranging from 8-12cm diameter along with rice husk and cement mortar with hollow openings in its core to lighten its weight. This proposal requires both the design of the mold and the mix.

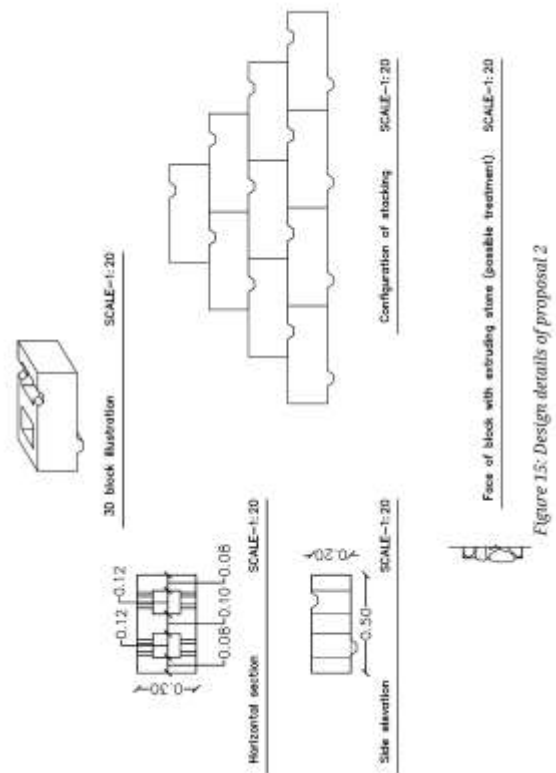


Figure 10. Design details of proposal 2

### 3.4.2.1 Implementation and Construction Methods

Steps of implementation

1. Design and fabricate a mold with openings
2. Sieve the stone to achieve required stone size
3. Place the waste stone in the mold
4. Prepare the mixture of rice husk, cement, sand and water
5. Pour the mixture into the mold over the placed waste stone
6. Leave the mixture in the mold to harden
7. Use the building block in the same method use the thick (highest strength) portion of the palm fronds to encircle the core and tie a strand of the lighter fronds to hold them all together.

### 3.4.2.2 Thermal Conductivity

U-Value (W/m <sup>2</sup> .K):	0.730
Admittance (W/m <sup>2</sup> .K):	0.990
Solar Absorption (0-1):	0.531
Visible Transmittance (0-1):	0
Thermal Decrement (0-1):	0.03
Thermal Lag (hrs):	5
[SBEM] CM 1:	0
[SBEM] CM 2:	0
Thickness (mm):	320.0
Weight (kg):	439.917

Figure 10. Ecotect results for Proposal 2 wall section

The proposed wall section has been built and formulated on Autodesk Ecotect that is an analysis sustainable building design software that offers building energy analysis tools for architects. The material was tested to attain the thermal conductivity and properties of the proposed wall section being:

- U-value: Measure of heat loss
- Admittance: Material's ability to absorb and release heat from a space
- Solar absorption: Amount of solar energy absorbed by the wall that is neither reflected nor transmitted
- Thermal lag: Material's required time to add or remove heat from a mass before it reaches the design set point temperature

Analyzing proposal 2, it could be established that the wall component possesses a low U-Value and admittance values due to the stone's (collectively) high insulating properties. The wall section was able to achieve reasonable solar admittance values along with a 5 hour thermal lag achievement. The wall component is considered relatively heavy in comparison with existing building blocks such as red bricks but however has much higher environmental

performance and an aesthetical component with the extruding stone element.

### 3.4.3 Proposal 3- Stone paste / Decorative

The third proposed wall section uses a combination of waste stone material located on site, gypsum, and white cement. The gypsum and cement are located in Ain El Sira zone within a 2 km radius from the site where workshops and markets of cornices and decorative elements exist (GIZ, 2012). The idea is to crush the stone into very small fragments within the 1 cm range. After that, a combination of the gypsum and white cement is added to the stone fragments to create a paste like component. On the other hand, there is an approach of creating molds of various forms into which the paste can be poured into. The shapes do not have to be linear or regular and could provide limitless designs, patterns and shapes. The shapes could also include the embedding of external components such as flower boxes within the wall. The molds could contain extruding members that would be used to interlock and attach to neighboring blocks like Lego parts (tongue and groove connections). Palm fronds could be implemented within the walls to add to its strength depending on the use and nature of the wall design.

#### 3.4.3.1 Implementation and Construction Methods

Steps of implementation

1. Crush small size stone using stone crushing machine
2. Sieve stone particles to achieve maximum size of 1cm radius
3. Create mold with intended design either engraved or intrusions or extrusions, etc.....
4. Prepare the mixture of white cement and gypsum
5. Mix the stone particles with the mixture prepared to create paste
6. Pour the paste into the mold
7. Leave paste to harden
8. Move block to specified location (Cast in place if selected block is one with connection with floor slab)
9. Move block to attach to other blocks through tongue and groove connections created in the poured block.
10. Apply desired finishes to interior and exterior (if preferred).

#### 3.4.3.2 Thermal Conductivity

U-Value (W/m <sup>2</sup> .K):	4.340
Admittance (W/m <sup>2</sup> .K):	4.600
Solar Absorption (0-1):	0.531
Visible Transmittance (0-1):	0
Thermal Decrement (0-1):	0.96
Thermal Lag (hrs):	5
[SBEM] CM 1:	0
[SBEM] CM 2:	0
Thickness (mm):	100.0
Weight (kg):	248.850

Figure 11. Ecotect results for Proposal 3 wall section

The proposed wall section has been built and formulated on Autodesk Ecotect that is an analysis sustainable building design software that offers building energy analysis tools for architects. The material was tested to attain the thermal conductivity and properties of the proposed wall section being:

- U-value: Measure of heat loss
- Admittance: Material's ability to absorb and release heat from a space
- Solar absorption: Amount of solar energy absorbed by the wall that is neither reflected nor transmitted
- Thermal lag: Material's required time to add or remove heat from a mass before it reaches the design set point temperature

Analyzing proposal 3, it could be concluded that the wall section has achieved average U-Value of 4.340, Admittance of 4.6, solar absorption of 0.531 and a thermal lag of 5 hours. The results are relatively low due to the fact that this building element possesses a small cross section. The component is intended to be used as a decorative element.

#### 4. Analytical and Comparative Review

In order to be able to assess the thermal properties of the proposed wall sections, a comparative review should be constructed to compare the proposed with the existing wall sections commonly used and sought to be replaced..

U-Value (W/m <sup>2</sup> .K):	1.950
Admittance (W/m <sup>2</sup> .K):	4.550
Solar Absorption (0-1):	0.495
Visible Transmittance (0-1):	0
Thermal Decrement (0-1):	0.39
Thermal Lag (hrs):	7.8
[SBEM] CM 1:	0
[SBEM] CM 2:	0
Thickness (mm):	230.0
Weight (kg):	452.500

Figure 12. Ecotect results for double brick wall

U-Value (W/m <sup>2</sup> .K):	2.620
Admittance (W/m <sup>2</sup> .K):	4.380
Solar Absorption (0-1):	0.418
Visible Transmittance (0-1):	0
Thermal Decrement (0-1):	0.7
Thermal Lag (hrs):	3
[SBEM] CM 1:	0
[SBEM] CM 2:	0
Thickness (mm):	130.0
Weight (kg):	245.000

Figure 13. Ecotect results for double brick wall.

#### 5. Economic Analysis & Conclusion

In order to achieve a successful component that would actually be able to attain success and replace the existing building block of red bricks, the economic value of the product and component should be intriguing and competitive. The economic aspect is the main factor that people seek since their aim is to reduce the building expenses as much as possible.

Below is a table including the prices of the various construction materials to be used in the analysis and comparison of the proposed components:

Material	Price
Sand	30 LE per m <sup>3</sup>
Cement	500-600 LE per 50 kg
Stones	0
Rice husk	(transportation fee)
Steel	5100-5700 LE per ton
Aggregates	100 per m <sup>3</sup>
Red Bricks	300 per 1000 bricks
Palm fronds	100 LE per ton
Gypsum	375 LE

Figure 13. Table illustrating the market value of the different building components and materials

##### 5.1.1 Methodology of Comparison

In order to correctly measure the true value of each wall component, it was only relevant to calculate the value of construction of a whole wall. The comparison process will take place between the proposed wall section of the building block and the existing commonly used wall cross section of single layered and double layered red brick since they will be within the same category. The wall that will be built and economically weighed is a 3X4m wall. Furthermore, analysis and cost of the two other remaining proposed components will be presented to test their feasibility and tendency to contribute as a contender in the present market.

##### 5.1.1.1 Existing Brick wall

Questioning market and method of payment:

Observing and surveying engineers and personnel involved in the Egyptian market and construction industry, it was analyzed and concluded that the price of purchasing 1000 bricks would range from 300 LE to 350 LE.

Price of bonding material:

Price of cement mortar required to bond 1000 bricks can account for an extra 75 LE.

Number of blocks required:

$3\text{m} / 0.07\text{m}$  (accounting for cement mortar 1cm)= 42.86 = 43 rows of brick

$4\text{m} / 0.13\text{m}$  (accounting for cement mortar 1cm)= 30.76 = 31 bricks per row

$43 \times 31 = 1333$  bricks are required to build the wall of area (4X3m)

Price of wall:

Single wall:

$(1333 / 1000) \times 425$  (price of bricks and mortar)= 566.52 LE

Double wall:

$(2666 / 1000) \times 425$  (price of bricks and mortar)= 1133 LE

### 5.1.1.2 Palm fronds, rice husk and stone

The required quantity of material to compose this proposed wall will acquire the following:

- Around 300 palm fronds will be needed to be components of wall shell and column reinforcement, weighing around 750kg
- Volume of  $3\text{m}^3$  of rice husk
- Volume of  $0.36\text{m}^3$  of stone
- 3 PVC waste pipes

Prices:

- Palm fronds = 30 LE
- Rice husk = 0 LE (transportation and compression fee of 100-150 LE)
- Stone = 0 LE (72 LE price of crafted stone they sell)
- Waste PVC pipes = 20 LE

The total value required to construct the proposed wall section is 200-250 LE of material, excluding the cost of labor and neglecting the price of stone.

#### 1. Proposal 2 - Stone block

Given that the wall requires  $12\text{m}^2$  coverage, the calculation of the number of blocks required takes place. The coverage (elevation) of the stone block is (20X30cm):

Price of single building block:

- **Alternative 1** (Assuming that the waste left over the stone is sold with the same price of the stone crafted) :

The first step is to calculate the volume of the block:

$(\text{Block} = 0.5\text{m} \times 0.2\text{m} \times 0.3\text{m} = 0.3\text{m}^3) - (\text{Voids} = 2(0.12\text{m} \times 0.12\text{m} \times 0.2\text{m}) = 0.0028\text{m}^3) = 0.0272\text{m}^3$

The volume of a single block that accounts for  $0.0272\text{m}^3$  is then subdivided to contain 70% stone and 30% cement mortar. This means that  $0.019\text{m}^3$  of the volume will be composed of stone and  $0.00816\text{m}^3$  of the volume composed of cement mortar components of sand, cement and water.

By multiplying the volume of stone by the price of stone (200 LE for  $\text{m}^3$ ), it could be concluded that the price of the stone component in a single building block is 3.80 LE.

By dividing the ratio of cement mortar into its three components and multiplying them by their respective market values we could conclude that the prices of these elements for a single building block are as follows:

Cement: 3.06 LE

Sand: 0.17 LE

Water: (Assumed exaggerated value of 0.05 LE)

It could then be summed up that the value of composing a single building block is 7.08 LE.

- **Alternative 2** (Assuming that the waste left over stone is of no value since it is thrown away):

It could then be summed up that the value of composing a single building block is 3.82 LE.

Price of bonding material:

No bonding material is required for the assembly; the wall is connected by a tongue and groove embedded in the building blocks.

Number of blocks required:

$3\text{m} / 0.2\text{m}$ (length of block)= 15 rows of blocks

$4\text{m} / 0.5\text{m}$ (width of block)= 8 bricks per row

$15 \times 8 = 120$  stone blocks are required to build the wall of area (4 X 3m)

Price of wall:

**Alternative 1:**

$7.08\text{ LE} \times 120 = 849.60\text{ LE}$

**Alternative 2:**

$3.80\text{ LE} \times 120 = 456\text{ LE}$

Logically speaking, Alternative 2 of calculation would be the price of the product with no profit value.

#### 2. Proposal 3 - Stone paste | Decorative

The required quantity of material to compose  $1\text{m}^3$  of this proposed wall will acquire the following:

- Stone:  $0.45\text{m}^3$
- White cement mortar:  $0.15\text{m}^3$
- Gypsum:  $0.20\text{m}^3$
- Rice husk:  $0.20\text{m}^3$

Prices:

- Stone: 0 LE (90 LE price of crafted stone they sell)
- White cement mortar: 120 LE
- Gypsum: 75 LE
- Rice husk: 0 LE (transportation and compression fee of 10-15 LE)

The total value required to construct the proposed wall section is 90 LE of material, excluding the cost of labor and neglecting price of the stone and the mold fabrication.

## 6. Conclusion

The assessment of the proposed wall sections on both the physical and economic levels, reveals that the proposed wall cross sections represent a good approach to treating the projected problem as stated; overcoming the vanishing cultural and architectural language that has been replaced with the informal and “random” construction spreading in our nation. The following confirms these findings:

Proposal 1 presents a lightweight structural component. It can be observed that the use of palm fronds in buildings bestows a strong structural component and a cultural essence, involving a long living labor of skill and craftsmanship in Upper Egypt. The material displays strength of fabric in addition to the material’s tendency to be shaped and intertwined. The use of the material achieves a strong connection to Upper Egypt’s sub-communities and maintains common ground of interest through material exchange in a process of expanding and developing an unappreciated and unused waste material. The proposed wall section will also introduce a strong bond to the lower Egyptian sub-communities and villages, forming another platform based on common interest and exchange of material; developing and spreading a structural component of low cost and a highly environmental performance.

Proposal 2 introduces a building block that uses the Khayala site’s waste stone to generate a high performance environmental building component that does not require the use of bonding material, and connects using a method of interlocking. Moreover, the material is of high strength and could be used as a self-sustaining structural element. Introducing this building block will build a connection with suppliers of materials such as cement and sand and will present to the community a building block that could be aesthetically utilized besides its functional and structural capabilities in an attempt to initiate a new movement towards “natural material” facades. The material in comparison with the dominant existing building material of red brick provides higher environmental and physical performance. Regarding the cost of using this block to form walls, the composition has proven to be economical within the price range of both the single brick and double brick. The weakness of the material lies in its bulkiness; 50 cm length, 20 cm height and 30 cm depth, which limits the component’s flexibility in building and design.

Proposal 3, offers the stone paste wall configuration, accordingly, it is observed that the developed methodology and mixture component will open doors to unordinary designs, with the ability of the component to form endless configurations due to its fluidity and smoothness prior to hardening. The component could be characterized as tough, and is able to compose solid elements that are classified as aesthetical decorative elements, giving it an advantage over gypsum decorative products due to its toughness and durability. The production of this component will create a connection between the site with the neighboring sub-community of Ain El Sira that works with gypsum to create decorative cornices and components. The material could be classified as economic and has a high propensity to compete in the local market.

To conclude, Egypt is a land that possesses a wide range of resources that are unused and barely fulfilling their great potentials. It is the role of thinkers and scientists to connect the dots and work on finding adequate approaches of building common grounds of interest and connecting people through the available resources. Egypt today is a divided nation due to

reasons that as seen could be categorized as socio-political but in the roots lies an economic query for prosperity and livelihood. In order to rise and unite, one must start with simple solutions, that do not intimidate or discourage the intended beneficiaries with extreme changes and modifications, but rather present them with efficient methods and tools of treatment that allow them to be both the “actors and the viewers” of development. The model envisioned in the Khayala site is merely a starting point; by the development of the available resources and empowerment of people, the Khayala site would hopefully expand and develop its craft, gain profit, make connections and on the long run, re-shape the heritage of tomorrow by altering the dominant form of construction and opening doors to innovation.

Note: Prices used are based on prices in the year 2014.

## 7. REFERENCES

- Bowman, M., Ahmad, A.E., Alyhassan, O.S. and Khalil, M.M. (1992). Surveying of some date palm parameters and properties to be utilized in date palm mechanization. *Agricultural mechanization in Asia and Africa and Latin America*, 23(2), 67-69.
- A. Ramezaniapour, F. Gafarpour, M.H. Majedi, Use of rice husk in the production of masonry cements, *Building and Housing Research Center (BHRC)*, September 1997.
- Al-Baijat, Hamadallah. "The Use of Basalt Aggregates in Concrete Mixes in Jordan ." *Jordan Journal of Civil Engineering*. 2.1 (2008): 63-70. Print. <<http://elearning.just.edu.jo/jjce/issues/paper.php?p=40.pdf>>.
- Jana, Revedin. Empowerment by Participative Design The Urban Laboratory Zabbaleen. Locus Foundation.org. UNESCO, 2012. Web. 15 Oct. 2013.
- “DVV | Adult Illiteracy, Brain Architecture, and Empowerment of the Poor.” Dvv International. N.p., n.d. Web. 06 Dec. 2013.
- GIZ, and KfW. *Participatory Upgrading of Informal Areas: A Decision-makers’ Guide for Action*. Participatory Development Programme in Urban Areas in Egypt. Cairo: Participatory Development Programme in Urban Areas (PDP) in Egypt, 2012. Print
- GIZ. *Knowing Local Communities: Guide*. Cairo: Participatory Development Programme in Urban Areas (PDP) in Egypt, 2012. Print.
- GIZ (2). *Maximizing Use Value: Action Guide for Informal Areas*. Participatory Development Programme in Urban Areas in Egypt. Cairo: Participatory Development Programme in Urban Areas (PDP) in Egypt, 2012. Print
- Kerama Jahromi, M., Jafari A., Rafiee S. and Mohtasebi, S.S. (2007). A survey on some physical properties of the Date Palm tree. *Journal of Agricultural Technology*, 3(2): 317-322.
- Khoddam Razavi, S. R, “Rice husk ash a mineral admixture for high performance concrete”, Msc Thesis, Amirkabir University of Technology Press, 2005.
- Marthong, C. "Effect of Rice Husk Ash (RHA) as Partial Replacement of Cement on Concrete Properties." *International Journal of Engineering Research & Technology (IJERT)*. 1.6 (2012): n. page. Web. 18 Dec. 2013.
- Mehta, P.K., "High-performance, high-volume fly ash concrete for sustainable development", Proceedings of the

International Workshop on Sustainable Development and Concrete Technology, Beijing, China, May 20–21, 2004.

M. Zhang, V. M. Malhotra, "High-Performance Concrete Incorporating Rice Husk Ash as a Supplementary Cementing Material", *ACI Materials Journal*, November-December 1996, Tittle no. 93-M72, PP. 629-636.

MOPIC, "Participatory Development Programme in Urban Areas." Participatory Development Programme in Urban Areas RSS. Egyptian Ministry of Planning and International Cooperation (MOPIC), Spring 2004. Web. 21 Sept. 2013. <<http://egypturban.net/about-pdp>>.

Ramezaniapour, A.A. "The Effect of Rice Husk Ash on Mechanical Properties and Durability of Sustainable Concretes." *International Journal of Civil Engineerng*. 7.2 (2009): n. page. Web. 18 Dec. 2013.

Robertson, Eugene. United States. United States Department of The Interior Geological Survey. *Thermal Properties of Rocks*. 1988. Print. <<http://pubs.usgs.gov/of/1988/0441/report.pdf>>.

Shamsi, M. "Some physical and mechanical properties of date palm trees related to cultural operations industry mechanization ." *Journal of Agricultural Technology* . 5.

(2009): 17-31. Web. 18 Dec. 2013. <[http://ijat-aatsea.com/pdf/June\\_v5\\_n1\\_09/3-10-IJAT2008\\_37F.pdf](http://ijat-aatsea.com/pdf/June_v5_n1_09/3-10-IJAT2008_37F.pdf)>.

Sims, David, and Janet L. Abu-Lughod. *Understanding Cairo: The Logic of a City out of Control*. Cairo: American University in Cairo, 2010. Print.

Sosna, K. "Laboratory determination of the mechanical properties of granite rocks ." *ARCADIS Geotechnika Inc*. 988.4 n. page. Web. 18 Dec. 2013. <<http://www.kiviniria.nl/eygec/papers/49 DS Sosna.pdf>>.

Subramanian, N. "Sustainability of RCC Structures Using Basalt Composite Rebars S." *Masterbuilder*. (2010): 156-164. Web. 18 Dec. 2013. <<http://www.sefindia.org/?q=system/files/Sustainability of RCC using Basalt composite Rebars-MasterBuilder-Sept2010.pdf>>.

Suryawanshi, D.G. India. National Research Laboratory for Conservation of Cutral Property. *Basic Studies on the Properties of Palm Leaf*. Lucknow: Paper, Web 13 December 2013.

Torabi, Anita. "Insight into petrophysical properties of deformed sandstone reservoirs." *AAPG Bulletin*. 97.4 (2013): 619-637. Web. 18 Dec. 2013. <<http://folk.uib.no/nglhe/Papers/AAPG 2013 Torabi, Fossen & Braathen.pdf>>.

# Issues and Concerns In Software Component Selection

Nitish Madaan  
Department of CSE and IT  
ITM University  
Gurgaon, India

Jagdeep Kaur  
Department of CSE and IT  
ITM University  
Gurgaon, India

---

**Abstract:** The increasing availability of COTS (commercial-off-the-shelf) components in the market of software development has concretized the opportunity of building whole systems based on previously built components. Component-Based Software Engineering (CBSE) is an approach which is used to improve efficiency and productivity of software system with the help of reusability. CBSE approach improves software development productivity and software quality by selecting pre-existing software components. Reusability in Component-Based Software Development (CBSD) not only reduces the time to market in development but also brings the cost down of development heavily. This paper represents the challenges which are faced by software developer during component selection like reliability, time, components size, fault tolerance, performance, components functionality and components compatibility. This paper also summarizes algorithms used for component retrieval according to availability of component subset.

**Keywords:** Component Based Software Development (CBSD), Software Component Selection, Case Based Reasoning, Component Based Software Engineering (CBSE), Software selection process.

---

## 1. INTRODUCTION

As compared with traditional approach, Component-based software engineering (CBSE) helps in developing a quality software system with less time and less resources. It is necessary to identify the software component and must be evaluated in order to check if they able to provide the requisite functionality or not for the system under the development. Most of the problems in the component based software development are considered to be solved as the efficient component selection.

In the early 1990's, researchers and practitioners choose to shift towards the component technology because it became visible to both researchers and practitioners that object-oriented technologies were not enough to manage with the rapidly changing requirements of real-world software systems. If we had a collection of reusable software components, we could build applications by simply plugging existing components together. In Component Based Software Component, a complex system is build with the help of assembling the simpler and small pieces obtained in various manner. By using different approaches research efforts have been made to make the process of reusability of component based software more effective, predictable and less expensive as compare with simple software reusability. CBSD and Component-Based Software Reusability (CBSR) approaches of software engineering is not similar to traditional engineering domain. CBSD and CBSR at last provide solution to all complex problems and help not only to reduce the time to market but also help in bring down the development cost significantly [1]. During reuse of pre-existing software components, components selection factors play an important role. CBSE is an approach which is used to enhance the reusability from the pre-existing software components. Already built software component selection process identifies methods to extract software requirements in the general sense, but they

do not explicitly address how to specify security requirements [4].

Another challenge is Security requirements specification because requirements cover both functional and non-functional aspects and many software developers may not be familiar with the scope of security issues needing to be addressed. This paper presents analysis of challenges faced throughout the software component selection.

## 2. SOFTWARE COMPONENT SELECTION ISSUES

In components selection, a number of software components selected from a subset of components or from components repository in a manner so that their composition satisfies the specifications. In CBSE component selection factors plays an important role. Client may get very good quality software, if researcher and Practitioners keeps all the challenges in mind at the time of selection of components.

### 2.1. Software Quality Evaluation

There are a number of quality attributes are concerned for the development of a software system. We may define the overall system quality measure (Q), based on a set of quality attributes (A) as proposed by Vows and Arrest [2]. The set attributes (A) includes reliability, performance, fault tolerance, safety, security, availability, testability, and maintainability. In a straightforward manner some other measurable quality attributes considered as important may also be included.

Overall software quality may be understood as weighted linear combination of the values for each of these attributes:

$$Q = w_R R + w_P P + w_F F + w_{S_a} S_a + w_{S_e} S_e + w_{A_v} A_v + w_T T + w_M M \quad (1)$$

Where,

R = Reliability

P = Performance

F = Fault tolerance

Sa = Safety

Se = Security

Av = Availability

T = Testability

M = Maintainability

The values  $w_R$ ,  $w_P$ ,  $w_F$ ,  $w_{Sa}$ ,  $w_{Se}$ ,  $w_{Av}$ ,  $w_T$ ,  $w_M$  denote the weights assigned to the corresponding quality attribute. The summation of all the weights assigned to all the quality attributes is equal to 1. This approach facilitates a simple, flexible, and consistent way to evaluate and compare the total software quality of proposed designs based on the needs of the stakeholders. The type of software describes the weighting for each attribute. The weight for security would probably be higher for a financial system than that for safety while the weight may be less for testability. The weighted key attributes for a safety critical system, would maybe be reliability, performance, safety, fault tolerance, and availability. The key weighted attributes for an ecommerce system would be reliability, performance, availability, security, and maintainability. If we understand each candidate component to contribute a certain amount of value toward each individual quality attribute then this approach may be extended for use within a component-oriented context. However, each quality attribute has its own unit of measurement.

Comparison of different types of measurement of units is not able to be compared in a significant manner. In order for the weighting scheme described above to make meaningful comparisons it is necessary for all quality metrics must be able to be of equal scale. For example, Maintainability complete of 4.5 and a Reliability score of 4.5 should both contribute equally toward the overall software quality if their weights are equal. To measure all quality attributes for the component to compare appropriately, it is necessary to standardize all quality attributes.

## 2.2. Components selection factors

Selection of a components are dependent on some factors that are identified as performance, time, size of component, fault tolerance, functionality of components, reliability, compatibility of components and also considered the availability of component subset.

### a) Performance

At the time of selection of component performance is the main challenge. Performance of a system cannot be expressed in terms of the performance of its individual component. Performance is the extent to which a system or component accomplish its designed function within given constrains such as accuracy, availability, efficiency, response time, recovery time, resource usage, speed etc. Performance cannot be calculated for the individual component, rather than it is calculated for the completed system after integration of the system. To increase the performance of the system select those software components containing high modules cohesion, less module coupling, and less number of interfaces of components.

### b) Time

Development time and testing time saves when we use COTS components and it also improves the quality of our software.

### c) Size of Component

Size of the components completely depends upon the programming language and the code of components that may be written in low level or high level languages. User of the system always wants that the size of the system should be less. So to achieve this it is important point to be noticed that on high level language written components must be used because the requires lesser size.

### d) Fault Tolerance

Increase in Mean Time to Failure (MTTF) helps in increasing the fault tolerance. Capability of a component or module to run continuously without having any fault in any type of software or hardware[3]. Fault-tolerance or graceful degradation is the property that enables a system to continue operating properly in the event of the failure of some of its components.

### e) Reliability

The capability of component or system to execute its required functions under stated conditions for a specified period of time [3]. Reliability metrics helps in the measurement of the reliability like MTTF, MTTR, MTBF, ROCOF and availability. Reliability and availability are directly proportion to each other, where performance and availability of the components are improved by reliability.

### f) Reusability

The degree to which a software component can be used in more than one computer program or software system [3] is a main challenge to select a good quality software component. CBSE is an approach which is used to enhance the reusability with the development of CBS from the preexisting software components and reusability save the development time, effort and cost.

### g) Components Functionality and Architecture

The most serious challenges of an already built component is that functionality of the component and the architecture of component cannot be reused anywhere without change. According to the functionality and architecture of the component needs to be matched of newly develop component with the existing components that are already built. Some of the changes may require in the existing component functions and component architecture along with some extra features to develop the new component.

### h) Compatibility of Components

Checking compatibility between various versions of the components is most important challenge in the successful reusability of component. Already built component can be easily replaced or can be added in a new part easily if it is compatible with the previous version. For many years, the compatibility requirements are essential for running software system. Compatibility issues are relative simple when changes introduced in the software systems are of maintenance and improvement nature only. In a reasonable extent it is necessary to test plans, including regression tests, functional compatibility.

*i) Available Component Subset*

Available component subset inside the repository is also a main challenge during component selection according to the component requirements for a specific application domain. Available component subset may be small, moderate and large which create a problem for selection of algorithm for component retrieval.

**2.3.Common Steps of Component Selection Methods**

Although there is no commonly accepted method for component selection, all methods share some key steps that can be iterative and overlapping [4]. These steps are described as follows:

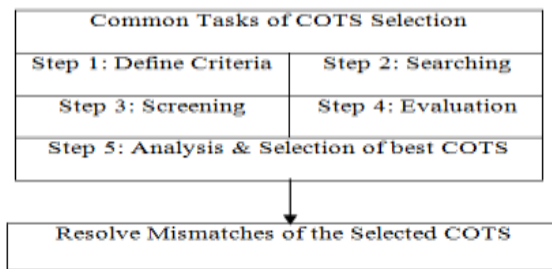


Figure 1. The general COTS selection process [5]

Step1: Define the evaluation criteria

Step2: Search for components.

Step3: Filter the search results based on a set of must have requirements. This results in defining a short list of most promising component candidates which are to be evaluated in more detail.

Step4: Evaluate components.

Step5: Analyze the evaluation data and select the components that have the best fitness with the criteria.

**3. CONCLUSION**

This work emphasizes on how to address the issue of component selection based on component costs and quality dimensions. Selection of optimal set of components not only improves selection process of component but also has a positive impact on the searching a good quality software component for software development. Addressing Components selection factors in an effective way will not only improve the optimal component selection and productivity but also put a positive impact on the quality and maintainability of software products. Initially, the software engineers analyze these challenges to select optimal components from pre-existing reusable component repository. In addition, a repository should address the problem of available component subset that are of different in term quantity, therefore according to the analysis this paper discusses, which algorithm is best for optimal component retrieval according to the availability of component subset.

**4. FUTURE SCOPE**

The field of quality attribute determination of component-based system is extensive and more research should be performed in this field. Future work in the development of component-based technologies could include determination

of more quality metrics for components that are easy to calculate and more feasible to use. It is important to devise a formal methodology for determining the relative weights to be assigned to the different quality metrics based on stakeholder input. In this regard, a potential approach may be to use the analytic hierarchy process. In real-world COTS selection problem, the decision maker may generate suitable possibility distributions based on subjective judgments and/or historical data. Thus, it would be interesting to apply trapezoidal, bell-shaped, triangular or other possibility distribution patterns for representing imprecise numbers in solving COTS selection model using the fuzzy logic approach.

**REFERENCES**

- [1]. Gill, N. S. and Tomar, "Software Component Technology: An Easy Way to Enhance Software Reusability", proceedings of 94<sup>th</sup> Indian Science Congress Conference, Annamalai University, Tamilnadu, INDIA, pp. 18-19 in 2007.
- [2]. Voas, J. and Agresti, W. W. 2004. Software quality from a behavioral perspective. IT Professional, 6,4 (July 2004), 46-50.
- [3]. IEEE Standards Board (1990). "IEEE Standard Glossary of Software Engineering Terminology", Computer Society of the IEEE.
- [4]. G. Ruhe, "Intelligent Support for Selection of COTS Products", LNCS, Springer, vol. 2593 2003. pp. 34-45
- [5]. Mohamed, Abdallah Sami Abbas Shehata. Decision support for selecting COTS software products based on comprehensive mismatch handling. Diss. University of Calgary, 2007.
- [6]. Pande, Jeetendra, Christopher J. Garcia, and Durgesh Pant. "Optimal component selection for component based software development using pliability metric." ACM SIGSOFT Software Engineering Notes 38.1 (2013): 1-6.
- [7]. Kaur, A. and Mann, K.S. 2010. Component selection for component based software engineering. International Journal of Computer Applications, 2, 1(2010),109-114.

# An Innovative Ultra Wideband Microstrip Phase Shifter Based on the LANGE Coupler

Soghra Sarkooyeh  
Department of ECE  
Isfahan University of Technology  
Isfahan, Iran

Mohammad Salimi  
School of ECE  
University of Tehran  
Tehran, Iran

**Abstract:** The method presented in this paper is based on coupled line in the standard schiffman phase shifters structure and replace it with lange coupler. To having a wider bandwidth, the stronger coupling is required. One way to achieve strong coupling is using of the parallel coupled lines that this property exist in the lange coupler. So this paper discusses the design of fixed broadband phase shifter by using the lange coupler and a novel phase shifters will be introduced according to the standard schiffman phase shifters. Finally optimal parameters to achieve the desired performance will be shown.

**Keywords:** Standard Schiffman Phase Shifters, Lang Coupler, Phase Deviation, Coupled Lines, Microstrip Lines.

## 1. INTRODUCTION

Differential phase shifters are four-port passive networks that their primary function is signal phase shift between input and output ports, with a slight practical weakening (ideally zero), at a fixed frequency band.

Phase shifter known as a microwave key component and it has various applications in microwave devices and systems, modulators, power divider, radar systems (fuzzy scanning, scan delay, electronic scanning radar arrays), communication systems, microwave systems, automatic control and industrial applications, microwave radio equipment (such as wide band phased antenna arrays).

Using the coupled lines is the most common method to making the phase shifters. Best known phase shifter is standard schiffman phase shifters. But the main problem of this method is its weak coupling. On the other hand, for a bandwidth of about 80%, this phase shifter shows large phase error ( $\pm 10^\circ$ ) [1]. In [2], the analysis of standard schiffman phase shifters studied, also design curves is provided. In [3, 4], to achieve a wider bandwidth with acceptable phase error, edge-coupled lines approach has been used. In structures of the edge-coupled lines, the coupling coefficient depends on distance of two coupled lines as well dielectric constant in the substrate. In some cases, since dielectrics used in substrate have low relative dielectric constant, phase shifter may not work properly. So to solve this problem, the coupled lines are used with high input impedance and are connected in parallel [4]. A number of authors have proposed the use of multi-row coupled segments that many phase shifters under schiffman phase shifters has been obtained [5-12]. In [13], a wide band fixed phase shifter, 60 and 90 degrees, is designed. In [14], using a saw tooth microstrip and ground, a strong coupling is obtained. As a result, a constant phase shift of 90 degrees on a wide bandwidth is obtained. This phase shifter shows a phase difference of  $90 \pm 5$  in 5/79 present of the bandwidth.

In general, obtaining 3 and 6 dB coupling through coupled lines is not easily achieved. One way to increase the coupling between edge-coupled lines is using multiple parallel coupled lines with each other. In this situation, the external fields on both edges of the line sides participate in the coupling. The easiest way to accomplish this situation is using the lange coupler [15].

Compared with branch-line couplers, the main advantages of lange coupler is the small size and a relatively wide

bandwidth. Branch-line couplers show bandwidth of about 20%, while its substrate area is also higher. Lange coupler has low loss and wide bandwidth. It is the best option in small and compact size [16]. In this coupler, four connected coupled line is used to obtaining strong coupling. Also the coupling of 3 dB bandwidth in 1 octave is easily possible. In [17] velocity compensation of the even and odd modes in lange coupler is attempted. This compensation will help to increasing the bandwidth.

## 2. MODELING

Replacing coupled lines with lange coupler in standard schiffman phase shifters leads to new coupler that by connecting the two ends together, we have a new phase shifter will be called lange phase shifter. This structure is shown in Figure 1. In the Lange coupler, there are narrow coupled lines which are about a quarter wavelengths and are in parallel with each other. This way, the external fields on both sides of the lines are allowed to participate.

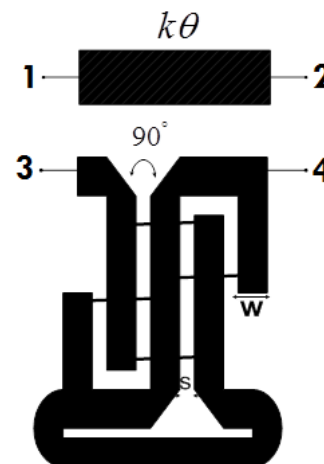


Figure 1. Structure of Lange Phase Shifter

To increase the coupling, it is necessary to use very small gaps. So coupler will have a very wide bandwidth about 1 octave. One of the disadvantages of the Lange coupler is suspended wires, which this is due to the geometric symmetry and voltage balance. Characteristic impedances in even and odd modes of the Lange coupler, based on the characteristic

impedance of the line with two conductors, expressed as follows [17]:

$$Z_{e4} = Z_{0e} \frac{Z_{0e} + Z_{0o}}{3Z_{0o} + Z_{0e}} \quad (1)$$

$$Z_{o4} = Z_{0o} \frac{Z_{0e} + Z_{0o}}{3Z_{0e} + Z_{0o}} \quad (2)$$

$Z_{0e}$  and  $Z_{0o}$  are characteristic impedances of even and odd modes, respectively. The characteristic impedance is equal to:

$$Z_0 = \sqrt{Z_{e4} Z_{o4}} = \sqrt{\frac{Z_{0e} Z_{0o} (Z_{0e} + Z_{0o})^2}{(3Z_{0e} + Z_{0o})(Z_{0e} + 3Z_{0o})}} \quad (3)$$

And coupling coefficient of voltage is equal to:

$$C = \frac{Z_{e4} - Z_{o4}}{Z_{e4} + Z_{o4}} = \frac{3(Z_{0e}^2 + Z_{0o}^2)}{3(Z_{0e}^2 + Z_{0o}^2) + 2Z_{0e} Z_{0o}} \quad (4)$$

In designing for measuring the distance between the arms, the even and odd mode impedances must be calculated. The even and odd mode characteristic impedance is a function of the characteristic impedance and coupling coefficients.

$$Z_{0e} = Z_0 \frac{4C - 3 + \sqrt{9 - 8C^2}}{2C\sqrt{1 - C} + C} \quad (5)$$

$$Z_{0o} = Z_0 \frac{4C + 3 - \sqrt{9 - 8C^2}}{2C\sqrt{1 + C} - C} \quad (6)$$

### 3. SIMULATION

In this section, to obtain the optimum performance of a phase shifter using Lange coupler, by a gradient optimization method for 6 dB Coupling, proper design parameters will be achieved. At least 3° phase error is defined as objective function in the fixed frequency band. In the simulation, the Duroid5880 substrate in the range 2 to 18 GHz with the specifications listed in Table 1 was used.

Table 1. Specifications of used substrate in the simulation

$f_0$ (GHz)	$\epsilon_r$	$h$ (mil)	$t$ ( $\mu m$ )	$\tan \delta$
10	2.2	25	17	0.0009

Table 2. Optimized value of Lange lines parameters

Parameters	Before Optimization	After Optimization
Distance (mm)	0.548	0.521
Length (mm)	0.317	0.178
Width (mm)	5.549	5.664

Table 2 shows the optimal values, including distance, length and width of the Lange lines, which have been obtained by gradient optimization. These parameters are chosen so as to create a center frequency of 180 degrees phase. The size of

proposed circuit is 15 to 25 mm. Table 3 compares the standard schiffman and Lange phase shifter. As can be seen, for coupling 3 dB, the deviation in the standard schiffman phase shifter is about 10 degrees, but in the phase shifter using the Lange coupler this amount is reduced to 5 degrees. Also the bandwidth is increased.

In figure 2, differential phase response in two phase shifter, standard schiffman and using the optimized parameters in Lange phase shifter, by the bandwidth of 7 to 13 GHz and the phase error of 3° is shown. Using the structure of the Lange coupler where the lines are parallel, strong coupling is obtained. And given the strong coupling, more bandwidth is obtained. Therefore, in the phase shifter using the Lange coupler, bandwidth is increased for a lesser phase error. Comparing of the phase difference from the phase shifter using Lange coupler and double schiffman phase in [4] shows differential phase response in double schiffman is asymmetric around the center frequency and bandwidth is narrower. But compared with the standard schiffman phase shifter, coupling coefficient is weaker. Other phase shifters proposed in [4] has a similar function of standard schiffman phase shifter. Differential phase response obtained is asymmetrical and narrower.

Table 3. Parameters comparison between standard schiffman and using the Lange coupler

Parameters	Using Lange Coupler	Standard Schiffman
Even mode impedance ( $\Omega$ )	120.914	120.914
Odd mode impedance ( $\Omega$ )	20.6759	20.6759
Characteristic impedance ( $\Omega$ )	50	50
Electrical length ( $^\circ$ )	40.1731	88.8622
Coupling coefficient (dB)	-3	-3
Phase deviation ( $^\circ$ )	5	10
Line width (mm)	0.327649	0.718763
Line distance (mm)	0.036037	0.005566
Line length (mm)	2.54615	5.846

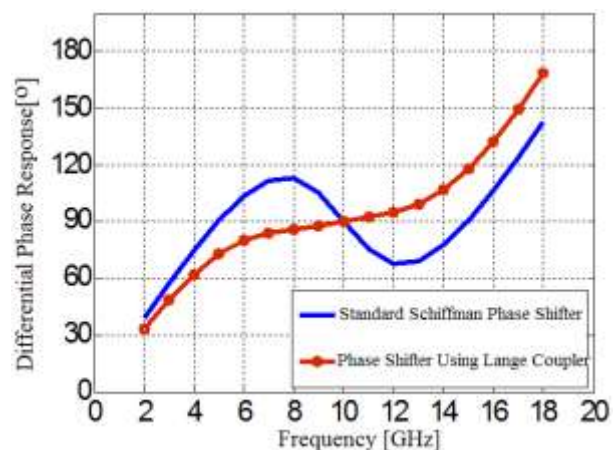


Figure 2. Comparison of differential phase response between standard schiffman and using the Lange coupler

Transmission and return loss in phase shifter using Lange coupler is compared by standard schiffman phase shifter in Figure 3 and Figure 4, respectively. As can be seen, using the

Lange coupler, transmission and return loss is much better than the coupled lines.

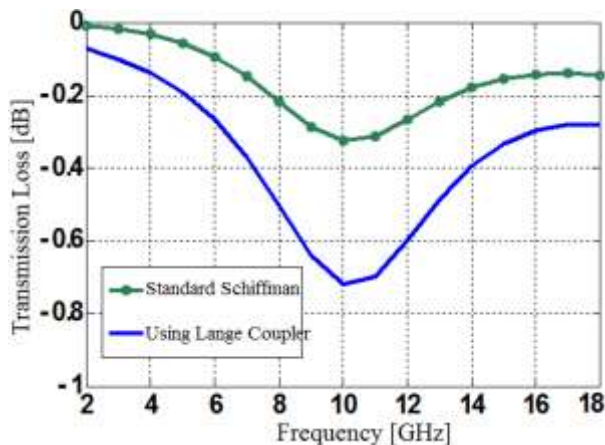


Figure 3. Comparison of transmission loss between standard schiffman and using the Lange coupler

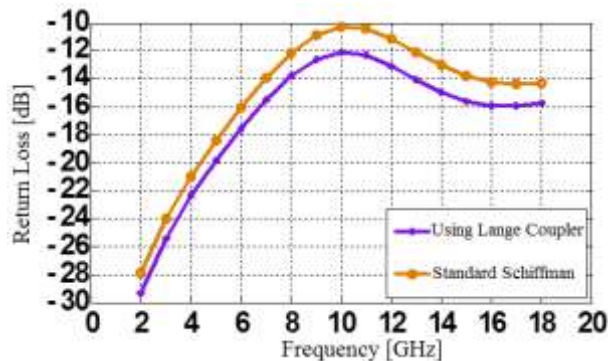


Figure 4. Comparison of return loss between standard schiffman and using the Lange coupler

#### 4. Conclusion

In this paper, the design problem of ultra-wideband microstrip phase shifter by using of the Lange coupler proposed. In general, to achieving strong coupling by using microstrip coupled lines in standard schiffman phase shifter is not easily achieved. Simulation results also showed that the use of a Lange coupler, in addition to creating a stronger coupling, in terms of manufacturing, it is also a much greater advantage (spacing of coupled lines to each other is further). Lange coupler caused transmission and return losses decrease about 0.4 dB in central frequency and 20%, respectively.

As suggested further research, using straight lines coupled instead of the non-uniform coupled lines caused the new more appropriate structure. The use of non-uniform line with smooth edges is not applicable. However, if internal lines changed to saw tooth, an ultra-bandwidth can be obtained.

#### 5. REFERENCES

[1] B. M. Schiffman, "A New Class of Broad-Band Microwave 90-Degree Phase Shifters" Microwave Theory and Techniques, IRE Transactions on, Vol. 6, pp. 232-237, 1958.  
[2] J. L. R. Quirarte and J. P. Starski, "Synthesis of Schiffman Phase shifters" IEEE Transaction on

Microwave Theory and Techniques, Vol. 39, pp. 486-492, June 1975.

[3] B. M. Schiffman, "Multisection Microwave Phase-Shift Network (Correspondence)" Microwave Theory and Techniques, IEEE Transactions on, Vol. 14, pp. 209, 1966.  
[4] J. L. R. Quirarte and J. P. Starski, "Novel Schiffman Phase Shifters" IEEE Transaction on Microwave Theory and Techniques, Vol. 41, pp. 9-14, 1993.  
[5] B. Schiek and J. Kohler, "A Method for Broad-Band Matching of Microstrip Differential Phase Shifters" Microwave Theory and Techniques, IEEE Transactions on, Vol. 25, No. 8, pp. 666-671, August 1977.  
[6] E.G. Cristal, "Analysis and Exact Synthesis of Cascaded Commensurate Transmission-Line C-Section All-Pass Networks" Microwave Theory and Techniques, IEEE Transactions on, Vol. 14, No. 6, pp. 285-291, June 1966.  
[7] K. Mohammadpour-Aghdam and N. Komjani and G. Vandenbosch and W. De raedt, "A Broadband Modified Differential Phase Shifter for Microwave Applications" Proceedings of the 39th European Microwave Conference, pp. 69-72, October 2009.  
[8] M. Naser-Moghadasi and G. R. Dadashzadeh and A. M. Dadgarpour and F. Jolani and B. S. Virdee, "Compact ultra-wideband phase shifter" Progress In Electromagnetics Research Letters, pp. 89-98, 2010.  
[9] J. P. Shelton and Mosko, "Synthesis and Design of Wide-Band Equal-Ripple TEM Directional Couplers and Fixed Phase Shifters" IEEE Trans. Microw. Theory Tech, Vol. MTT-14, No. 10, pp. 246-252, Oct. 1966.  
[10] W. J. D. Steenaart, "The Synthesis of Coupled Transmission Line All-Pass Network in Class of 1 ton" Microwave Theory and Techniques, IEEE Transactions on, pp. 23-29, 1963.  
[11] R. Mongia and I. Bahl, and P. Bharatia, RF and Microwave Coupled-Line Circuits. Artech House, 1999.  
[12] H. Oraizi and A. Shamsafar, "Design and Optimization of Wideband Multi Section Coupled-line Phase Shifters with Impedance Matching," PIERS Proceedings, Moscow, Russia, pp. 1450-1453, August 2009.  
[13] A. Abbosh, "Broadband Fixed Phase Shifters," IEEE microwave and wireless components letters, vol. 21, no. 1, pp. 22-24, January 2011.  
[14] Z. Zhange, Y. C. Jiao, S. F. Cao, X. M. Wange and F. S. Zhang, "Modified Broadband Schiffman Phase Shifter Using Dentate Microstrip and Patterned Ground Plane," Progress In Electromagnetics Research Letters, vol. 24 pp. 9-16, 2011.  
[15] J. Lange, "Interdigitated Strip-Line Quadrature Hybrid" Microwave Symposium, 1969 G-MTT International, pp. 10-13, 1969.  
[16] S. Uysal, Nonuniform Line Microstrip Directional Couplers and Filters. Artech House, 1993.  
[17] D. M. Pozar, Microwave Engineering. John Wiley & Sons, 2005.

## Effect of Titanium Oxide on Structure, Bearing Properties of Tin-Antimony-Lead and Tin-Aluminum Alloys

Abu Bakr El- Bediwi  
Metal Physics Lab., Physics  
Department, Faculty of Science,  
Mansoura University  
Mansoura, Egypt

Abbas Al- Bawee  
Faculty of engineering, University of  
Diayala  
Diayala, Iraq

Mustafa Kamal  
Metal Physics Lab., Physics  
Department, Faculty of Science,  
Mansoura University  
Mansoura, Egypt

**Abstract:** Effect of adding titanium oxide nanoparticles ( $\text{TiO}_2$ ) on structure, elastic moduli, Vickers hardness, internal friction, electrical resistivity and thermal properties of tin-antimony-lead and tin-aluminum bearing alloys have been investigated. Elastic modulus, Vickers hardness and thermal diffusivity of  $\text{Sn}_{87}\text{Sb}_{10}\text{Pb}_3$  and  $\text{Sn}_{80}\text{Al}_{20}$  alloys increased after adding  $\text{TiO}_2$  nanoparticles. Internal friction, thermal conductivity and specific heat of  $\text{Sn}_{87}\text{Sb}_{10}\text{Pb}_3$  and  $\text{Sn}_{80}\text{Al}_{20}$  alloys varied after adding  $\text{TiO}_2$  nanoparticles. Adding titanium oxide nanoparticles improved bearing properties, such as strengthens and internal friction of  $\text{Sn}_{87}\text{Sb}_{10}\text{Pb}_3$  and  $\text{Sn}_{80}\text{Al}_{20}$  alloys. The  $\text{Sn}_{85.5}\text{Sb}_{10}\text{Pb}_3(\text{TiO}_2)_{1.5}$  alloy has best properties for automotive industry. Also  $\text{Sn}_{78.5}\text{Al}_{20}(\text{TiO}_2)_{1.5}$  alloy has best properties for marine applications.

**Key words:** titanium oxide, internal friction, thermal properties, structure, hardness, resistivity, bearing alloys

### Introduction

Bearings are used to prevent friction between parts during relative movement. In machinery they fall into two primary categories: anti-friction or rolling element bearings and hydrodynamic journal bearings. Today, the term Babbitt covers a collection of "white metal" alloys consisting generally of a tin or lead base accompanied by antimony and copper. Babbitt metal is used as the lining for bearing shells of cast iron, steel and bronze. Fry manufactures two basic types of babbitt, high-tin alloys and high-lead alloys. Both are relatively low melting materials consisting of hard compound in a soft matrix. Al-Sn alloys have a very long history (Forrester 1960) to be used as bearing materials [1]. These alloys provide a good combination of strength and surface properties [2]. The fatigue strength of cold worked and heat treated Al-20%Sn-1%Cu alloy having reticular structure is close to that of Cu-30%Pb alloy with higher seizure resistance [3]. Aluminium has a low modulus of elasticity and apart from indium, lead has the lowest modulus of elasticity of all the soft phases alloying with aluminium [4]. Al-Sn based alloys are widely used as sliding bearing materials in automobile and shipbuilding industry [5, 6]. HVOF spray process has been introduced by McCartney to prepare Al-Sn-Si bearing alloy coatings. Post heat treatment of the HVOF sprayed coating at 300 °C proved the coarsening of tin and precipitate of Si in the coating [7, 8]. Based on the feasibility of preparing oxygen sensitive metal coatings, cold spray was also introduced to deposit Al-Sn binary alloy coatings [9]. Al-5Sn coating can be deposited by high pressure cold spray with nitrogen while Al-10Sn can only be deposited by low pressure cold spray with helium gas. Both Al-5Sn and Al-10Sn coatings present dense structures. The coarsening and/or migration of Sn phase in the coatings were observed when the annealing temperature exceeds 200 °C. Furthermore, the microhardness of the coatings decreased significantly at the annealing temperature of 250 °C [10]. Aluminium tin and leaded aluminium alloys slightly differ in mechanical properties. Frictional states created during sliding against steel shaft under oil lubrication were not much different. Leaded aluminium alloy bushes show marginally lower friction than the conventional ones [11]. Adding Cu/Pb to Sn-Sb alloy improve their

elastic modulus, internal friction, hardness and thermal conductivity [12]. The friction coefficients of Sn-20.2%Sb-16.6%Pb-2.6%Cu are lower than that of Sn-7.2%Sb-0.4%Pb-3%Cu under all scratch test conditions [13]. Structure, hardness, mechanical and electrical transport properties of  $\text{Sn}_{90-x}\text{Sb}_{10}\text{Bi}_x$  ( $x = 0$ , or  $x \geq 1$ ) alloys have been studied and analyzed [14]. The effects of solidification rate and microadditions on mechanical properties and micromorphology of  $\text{SnSb}_{10.4}$  alloy have been studied [15]. Creep behaviour, elastic modulus and internal friction of  $\text{SnSb}_{10}\text{Cu}_2\text{X}_2$  ( $\text{X}=\text{Pb, Ag, Se, Cd}$  and  $\text{Zn}$ ) alloys have been investigated also stress exponent values have been determined using Mulhearn-Tabor method [16]. The aim of this research was to investigate the effect of adding titanium oxide nanoparticles ( $\text{TiO}_2$ ) on structure, elastic moduli, Vickers hardness, internal friction and thermal properties of tin-antimony-lead and tin-aluminum bearing alloys.

### Experimental work

Two groups of quaternary bearing alloys, tin- antimony-lead- titanium oxide and tin- aluminum- titanium oxide, were used. These groups' alloys were molten in the muffle furnace using (high purity more than 99.95%) tin, antimony, lead, aluminum and titanium oxide. The resulting ingots were turned and re-melted several times to increase the homogeneity of the ingots. From these ingots, long ribbons of about 3-5 mm width and ~ 70  $\mu\text{m}$  thickness were prepared as the test samples by directing a stream of molten alloy onto the outer surface of rapidly revolving copper roller with surface velocity 31 m/s giving a cooling rate of  $3.7 \times 10^5$  K/s. The samples then cut into convenient shape for the measurements using double knife cutter. Structure of used alloys was performed using a Shimadzu X-ray Diffractometer (Dx-30, Japan) of  $\text{Cu-K}\alpha$  radiation with  $\lambda=1.54056 \text{ \AA}$  at 45 kV and 35 mA and Ni-filter in the angular range  $2\theta$  ranging from 0 to 100° in continuous mode with a scan speed 5 deg/min. Electrical resistivity of used alloys was measured by double bridge method. The melting endotherms of used alloys were obtained using a SDT Q600 V20.9 Build 20 instrument. A digital Vickers micro-hardness tester, (Model-FM-7- Japan), was used to measure Vickers hardness values of used alloys.  $Q^{-1}$ , the elastic modulus E and

thermal diffusivity  $D_{th}$  of used alloys were determined using the dynamic resonance method [17- 19].

$$\left(\frac{E}{\rho}\right)^{1/2} = \frac{2\pi L^2 f_0}{kz^2}$$

$$Q^{-1} = 0.5773 \frac{\Delta f}{f_0}$$

$$D_{th} = \frac{2d^2 f_0}{\pi}$$

Where  $\rho$  is the density of the sample under test,  $L$  is the length of the vibrated part of the sample,  $k$  is the radius of gyration of cross section perpendicular to its plane of motion,  $f_0$  is the resonance frequency and  $z$  is the constant depends on the mode of vibration and is equal to 1.8751.  $\Delta f$  is the half width of the resonance curve.

## Results and discussions

### Effect of adding $TiO_2$ nanoparticles on structure of Sn-Sb-Pb alloy

X-ray diffraction patterns of  $Sn_{87-x}Sb_{10}Pb_3(TiO_2)_x$  ( $x=0.5, 1$  and  $1.5$  wt. %) rapidly solidified alloys have lines corresponding to  $\beta$ - Sn, Pb/or Sb and SbSn intermetallic phases as shown in Figure 1. X-ray analysis show that, adding  $TiO_2$  to  $Sn_{87}Sb_{10}Pb_3$  alloy caused a change in Sn matrix structure such as lattice parameters and formed crystal structure (crystallinity, crystal size and the orientation) as seen in Table 1(a and b). That is because  $TiO_2$  nanoparticles dissolved in Sn matrix formed a solid solution and other accumulated particles formed a traces of phases.

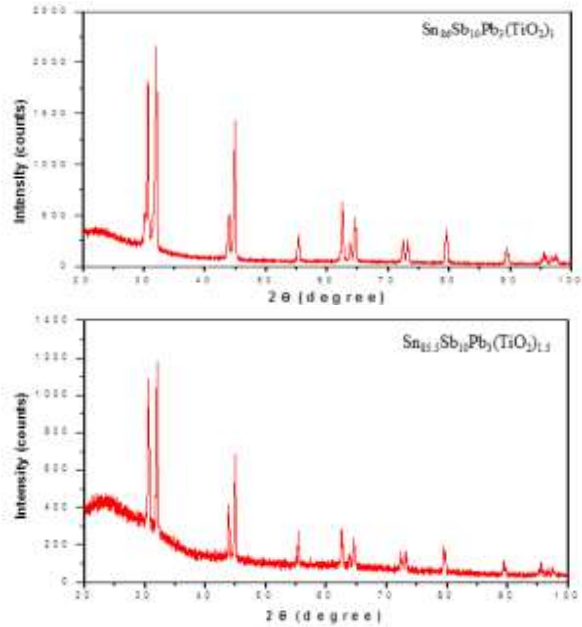
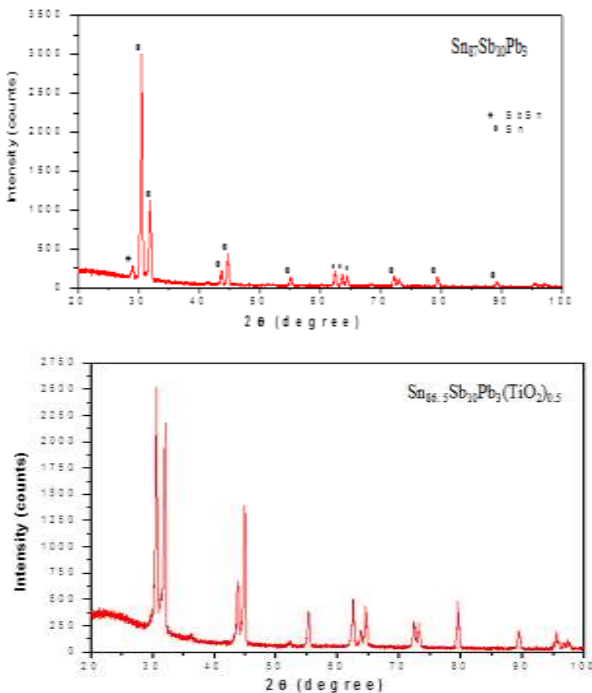


Figure 1:- x-ray diffraction patterns of  $Sn_{87-x}Sb_{10}Pb_3(TiO_2)_x$  alloys

Table 1a:- x-ray diffraction analysis of  $Sn_{87-x}Sb_{10}Pb_3(TiO_2)_x$  alloys

$Sn_{87}Sb_{10}Pb_3$					
$2\theta$	$d \text{ \AA}$	Int.%	FWHM	Phase	hkl
29.0695	3.07186	4.37	0.2755	SbSn	101
30.4985	2.92868	100	0.2400	Sn	200
30.6095	2.92557	69.41	0.0720	Sn	200
31.9779	2.796439	34.11	0.1920	Sn	101
41.5347	2.17246	0.77	0.5760	SbSn	012
43.6580	2.07160	5.13	0.4320	Sn	220
44.7618	2.02304	12.29	0.3360	Sn	211
55.1013	1.66539	3.75	0.3360	Sn	301
62.4237	1.48648	5.81	0.3360	Sn	112
63.6354	1.46106	4.05	0.3840	Sn	400
64.3731	1.44609	3.59	0.4320	Sn	321
68.2871	1.37243	0.41	0.5760	SbSn	113
72.1128	1.30874	3.63	0.2880	Sn	420
72.9123	1.29635	2.75	0.2880	Sn	411
79.3161	1.20698	3.59	0.2880	Sn	321
89.0610	1.09840	2.05	0.2400	Sn	432
95.3295	1.04205	1.46	0.3840	Sn	103
96.3177	1.03396	0.64	0.4800	Sn	330
97.0846	1.02783	0.75	0.4800	Sn	521



89.3181	1.09682	7.16	0.1771	Sn	432
95.4954	1.04154	7.27	0.1771	Sn	103
97.4966	1.02458	2.88	0.576	Sn	521

Sn <sub>86.5</sub> Sb <sub>10</sub> Pb <sub>3</sub> (TiO <sub>2</sub> ) <sub>0.5</sub>					
2θ	d Å	Int.%	FWHM	Phase	hkl
30.6118	2.92052	100	0.2558	Sn	200
32.0305	2.79433	80.39	0.2558	Sn	101
36.1764	2.48304	1.74	0.4723	Pb	220
43.7948	2.06715	25.53	0.3346	Sn	220
44.8366	2.02152	56.58	0.2952	Sn	211
52.2999	1.74926	1.68	0.3936	SbSn	021
55.2681	1.66214	13.94	0.2755	Sn	301
62.4854	1.48639	18.62	0.2558	Sn	112
63.759	1.45974	5.28	0.2755	Sb	107
64.5448	1.44385	16.61	0.2165	Sn	321
72.3498	1.30611	10.53	0.2165	Sb	018
73.1307	1.29409	8.95	0.2558	Sn	411
79.4279	1.20656	16.98	0.1968	Sn	321
89.2927	1.09706	6.94	0.1968	Sn	432
95.4951	1.04154	6.04	0.1968	Sn	103
96.6061	1.0325	1.82	0.2362	Sn	440
97.2882	1.02622	3.09	0.24	Sn	521

Table 1b:- lattice parameters and crystal size of β-Sn in Sn<sub>87-x</sub>Sb<sub>10</sub>Pb<sub>3</sub>(TiO<sub>2</sub>)<sub>x</sub> alloys

Alloys	a Å	c Å	V Å <sup>3</sup>	τ Å
Sn <sub>87</sub> Sb <sub>10</sub> Pb <sub>3</sub>	5.857	3.174	108.883	355.44
Sn <sub>86.5</sub> Sb <sub>10</sub> Pb <sub>3</sub> (TiO <sub>2</sub> ) <sub>0.5</sub>	5.841	3.18	108.62	514.283
Sn <sub>86</sub> Sb <sub>10</sub> Pb <sub>3</sub> (TiO <sub>2</sub> ) <sub>1</sub>	5.841	3.2	109.15	508.035
Sn <sub>85.5</sub> Sb <sub>10</sub> Pb <sub>3</sub> (TiO <sub>2</sub> ) <sub>1.5</sub>	5.843	3.19	108.83	529.678

Scanning electron micrographs, SEM, of Sn<sub>87-x</sub>Sb<sub>10</sub>Pb<sub>3</sub>(TiO<sub>2</sub>)<sub>x</sub> (x=0 and 1.5 wt. %) alloys show heterogeneity structure as shown in Figure 2. SEM micrographs of Sn<sub>87-x</sub>Sb<sub>10</sub>Pb<sub>3</sub>(TiO<sub>2</sub>)<sub>x</sub> alloys show β-Sn matrix and other accumulated particles formed traces of phases and that is agreed with x-ray results.

Sn <sub>86</sub> Sb <sub>10</sub> Pb <sub>3</sub> (TiO <sub>2</sub> ) <sub>1</sub>					
2θ	d Å	Int.%	FWHM	Phase	hkl
30.6133	2.92038	86.52	0.2558	Sn	200
32.0016	2.79679	100	0.2558	Sn	101
43.8373	2.06525	22.17	0.2755	Sn	220
44.8304	2.02178	66.02	0.2362	Sn	211
55.2842	1.66169	12.86	0.3346	Sn	301
62.4583	1.48697	25.71	0.2558	Sn	112
63.7276	1.46038	7.61	0.2165	Sb	107
64.4749	1.44525	17.75	0.2165	Sn	321
72.3608	1.30594	10.42	0.1771	Sb	018
73.0899	1.29471	10.52	0.1771	Sn	411
79.4307	1.20552	15.71	0.264	Sn	321
79.7468	1.20453	8.87	0.192	Sn	321
89.3151	1.09594	7.47	0.264	Sn	432
89.6708	1.09523	4.46	0.192	Sn	431
95.0358	1.04449	1.75	0.24	Sn	103
95.5155	1.04051	5.28	0.216	Sn	103
95.8764	1.04013	3.21	0.216	Sn	332
96.6134	1.03158	3.09	0.24	Sn	440
97.3745	1.02554	4.55	0.24	Sn	521

Sn <sub>85.5</sub> Sb <sub>10</sub> Pb <sub>3</sub> (TiO <sub>2</sub> ) <sub>1.5</sub>					
2θ	d Å	Int.%	FWHM	Phase	hkl
30.6023	2.9214	88.93	0.2755	Sn	200
32.0244	2.79485	100	0.2558	Sn	101
43.8265	2.06574	31.18	0.1968	Sn	220
44.9301	2.01753	60.27	0.2362	Sn	211
55.2598	1.66237	16.36	0.1771	Sn	301
62.4719	1.48668	20.78	0.1968	Sn	112
63.8004	1.45889	5.73	0.3149	Sb	107
64.5084	1.44458	14.03	0.1968	Sn	321
72.3331	1.30638	8.85	0.1574	Sb	018
73.1077	1.29444	10.06	0.1771	Sn	411
79.417	1.2067	12.82	0.1771	Sn	321

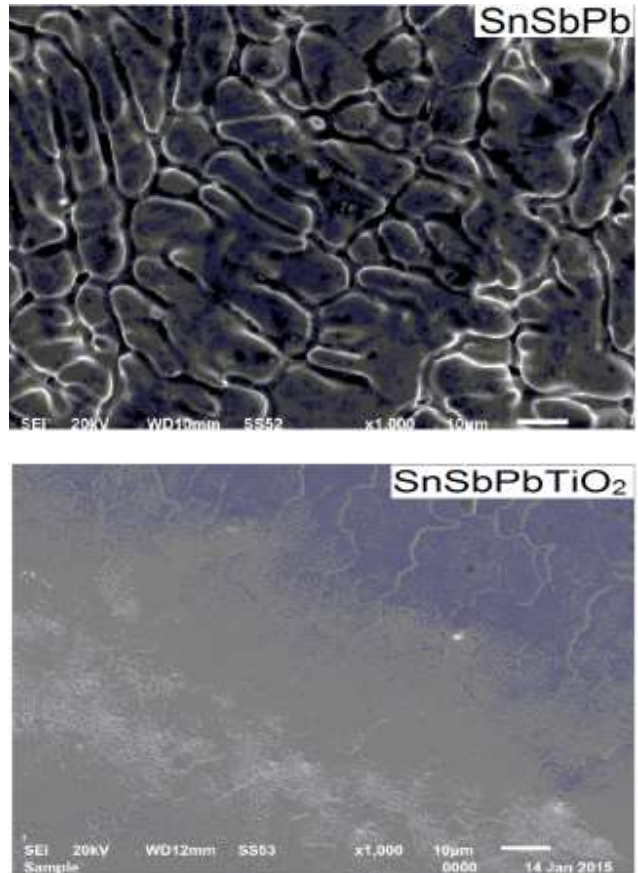


Figure 2:- SEM of Sn<sub>87</sub>Sb<sub>10</sub>Pb<sub>3</sub> and Sn<sub>85.5</sub>Sb<sub>10</sub>Pb<sub>3</sub>(TiO<sub>2</sub>)<sub>1.5</sub> alloys

**Effect of adding TiO<sub>2</sub> nanoparticles on mechanical properties of Sn-Sb-Pb alloy**

The elastic constants are directly related to atomic bonding and structure. Elastic moduli of Sn<sub>87-x</sub>Sb<sub>10</sub>Pb<sub>3</sub>(TiO<sub>2</sub>)<sub>x</sub> alloys are listed in Table 2. Elastic modulus of Sn<sub>87</sub>Sb<sub>10</sub>Pb<sub>3</sub> alloy increased after adding different ratio from TiO<sub>2</sub> nanoparticles. The Sn<sub>85.5</sub>Sb<sub>10</sub>Pb<sub>3</sub>(TiO<sub>2</sub>)<sub>1.5</sub> alloy has highest elastic modulus.

Table 2:- elastic moduli, internal friction and thermal diffusivity of Sn<sub>87-x</sub>Sb<sub>10</sub>Pb<sub>3</sub>(TiO<sub>2</sub>)<sub>x</sub> alloys

Alloys	E GPa	μ GPa	B GPa	Q <sup>-1</sup>	D <sub>th</sub> x10 <sup>-8</sup> m <sup>2</sup> /sec
Sn <sub>87</sub> Sb <sub>10</sub> Pb <sub>3</sub>	33.02	12.15	39.15	0.025	9.43
Sn <sub>86.5</sub> Sb <sub>10</sub> Pb <sub>3</sub> (TiO <sub>2</sub> ) <sub>0.5</sub>	38.3	14.1	45.3	0.031	27.36
Sn <sub>86</sub> Sb <sub>10</sub> Pb <sub>3</sub> (TiO <sub>2</sub> ) <sub>1</sub>	39.1	14.4	46.1	0.024	21.43
Sn <sub>85.5</sub> Sb <sub>10</sub> Pb <sub>3</sub> (TiO <sub>2</sub> ) <sub>1.5</sub>	47.2	17.4	55.4	0.018	41.87

The resonance curves Sn<sub>87-x</sub>Sb<sub>10</sub>Pb<sub>3</sub>(TiO<sub>2</sub>)<sub>x</sub> alloys are shown in Figure 3. Calculated internal friction and thermal diffusivity of Sn<sub>87-x</sub>Sb<sub>10</sub>Pb<sub>3</sub>(TiO<sub>2</sub>)<sub>x</sub> alloys are listed in Table 2. Internal friction of Sn<sub>87</sub>Sb<sub>10</sub>Pb<sub>3</sub> alloy varied after adding different ratio from TiO<sub>2</sub> nanoparticles. The Sn<sub>85.5</sub>Sb<sub>10</sub>Pb<sub>3</sub>(TiO<sub>2</sub>)<sub>1.5</sub> alloy has lowest internal friction.

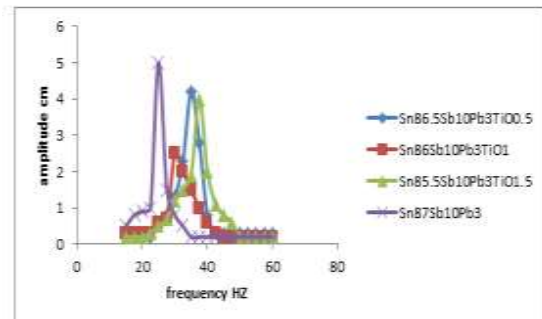


Figure 3:- resonance curves of Sn<sub>87-x</sub>Sb<sub>10</sub>Pb<sub>3</sub>(TiO<sub>2</sub>)<sub>x</sub> alloys

The hardness is the property of material, which gives it the ability to resist being permanently deformed when a load is applied. Vickers hardness of Sn<sub>87-x</sub>Sb<sub>10</sub>Pb<sub>3</sub>(TiO<sub>2</sub>)<sub>x</sub> alloys at 10 gram force and indentation time 5 sec are shown in Table 3. The minimum shear stress (τ<sub>m</sub>) value of Sn<sub>87-x</sub>Sb<sub>10</sub>Pb<sub>3</sub>(TiO<sub>2</sub>)<sub>x</sub> alloys was calculated using the equation [9], where ν is Poisson's ratio of the elements in the alloy and then listed in Table 3.

$$\tau_m = \frac{1}{2} H_v \left\{ \frac{1}{2} (1 - 2\nu) + \frac{2}{9} (1 + \nu) [2(1 + \nu)]^{\frac{1}{2}} \right\}$$

Vickers hardness of Sn<sub>87</sub>Sb<sub>10</sub>Pb<sub>3</sub> alloy increased after adding TiO<sub>2</sub> nanoparticles. That is because TiO<sub>2</sub> dissolved in Sn matrix formed a hard inclusion increased its hardness. Sn<sub>85.5</sub>Sb<sub>10</sub>Pb<sub>3</sub>(TiO<sub>2</sub>)<sub>1.5</sub> alloy has highest hardness.

Table 3:- Vickers hardness and minimum shear stress of Sn<sub>87-x</sub>Sb<sub>10</sub>Pb<sub>3</sub>(TiO<sub>2</sub>)<sub>x</sub> alloys

Alloys	H <sub>v</sub> kg/mm <sup>2</sup>	μ <sub>s</sub> kg/mm <sup>2</sup>
Sn <sub>87</sub> Sb <sub>10</sub> Pb <sub>3</sub>	28.52±1.8	9.41
Sn <sub>86.5</sub> Sb <sub>10</sub> Pb <sub>3</sub> (TiO <sub>2</sub> ) <sub>0.5</sub>	31.68±2.7	10.45
Sn <sub>86</sub> Sb <sub>10</sub> Pb <sub>3</sub> (TiO <sub>2</sub> ) <sub>1</sub>	36.53±3.3	12.05
Sn <sub>85.5</sub> Sb <sub>10</sub> Pb <sub>3</sub> (TiO <sub>2</sub> ) <sub>1.5</sub>	38.83±2.4	12.81

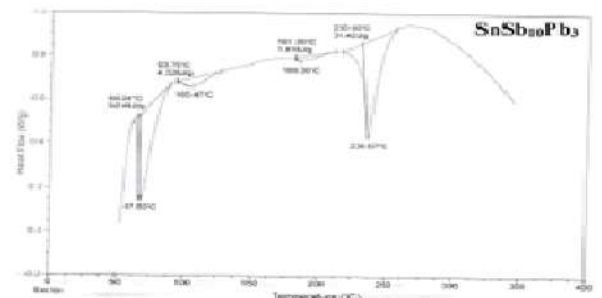
**Effect of adding TiO<sub>2</sub> on thermal properties and electrical resistivity of Sn- Sb- Pb alloy**

Thermal analysis is often used to study solid state transformations as well as solid-liquid reactions. Figure 4 shows DSC thermographs for Sn<sub>87-x</sub>Sb<sub>10</sub>Pb<sub>3</sub>(TiO<sub>2</sub>)<sub>x</sub> alloys. Little variation occurred in exothermal peak of Sn<sub>87</sub>Sb<sub>10</sub>Pb<sub>3</sub> alloy. The melting temperature and other thermal properties of Sn<sub>87-x</sub>Sb<sub>10</sub>Pb<sub>3</sub>(TiO<sub>2</sub>)<sub>x</sub> alloys are listed in Table 4. Melting temperature of Sn<sub>87</sub>Sb<sub>10</sub>Pb<sub>3</sub> alloy decreased after adding TiO<sub>2</sub> nanoparticles.

Crystalline defects serve as scattering center for conduction electrons in metals, so the increase in their number raises the imperfection. Electrical resistivity and calculated thermal conductivities of Sn<sub>87-x</sub>Sb<sub>10</sub>Pb<sub>3</sub>(TiO<sub>2</sub>)<sub>x</sub> alloys are shown in Table 4. Electrical resistivity of Sn<sub>87</sub>Sb<sub>10</sub>Pb<sub>3</sub> alloy varied after adding TiO<sub>2</sub> nanoparticles. That is because TiO<sub>2</sub> nanoparticles dissolved in the Sn matrix playing as scattering center for conduction electrons caused a change in matrix structure.

Table 4:- electric resistivity and other thermal properties of Sn<sub>87-x</sub>Sb<sub>10</sub>Pb<sub>3</sub>(TiO<sub>2</sub>)<sub>x</sub> alloys

Alloys	ρ x 10 <sup>-6</sup> Ω.cm	K W m <sup>-1</sup> K <sup>-1</sup>	C <sub>p</sub> x 10 <sup>3</sup> J/kg.k	Melting point °C
Sn <sub>87</sub> Sb <sub>10</sub> Pb <sub>3</sub>	67.3	2.30	1.84	236.87
Sn <sub>86.5</sub> Sb <sub>10</sub> Pb <sub>3</sub> (TiO <sub>2</sub> ) <sub>0.5</sub>	59.04	2.55	1.88	223.38
Sn <sub>86</sub> Sb <sub>10</sub> Pb <sub>3</sub> (TiO <sub>2</sub> ) <sub>1</sub>	65.19	2.32	3.93	229.52
Sn <sub>85.5</sub> Sb <sub>10</sub> Pb <sub>3</sub> (TiO <sub>2</sub> ) <sub>1.5</sub>	77.78	1.94	3.29	229.33



Scanning electron micrographs, SEM, of  $\text{Sn}_{80-x}\text{Al}_{20}(\text{TiO}_2)_x$  alloys show heterogeneity structure as shown in Figure 6. SEM micrographs of  $\text{Sn}_{80-x}\text{Al}_{20}(\text{TiO}_2)_x$  alloys show  $\beta$ - Sn matrix with other accumulated particles formed traces of phases and that agree with x-ray results

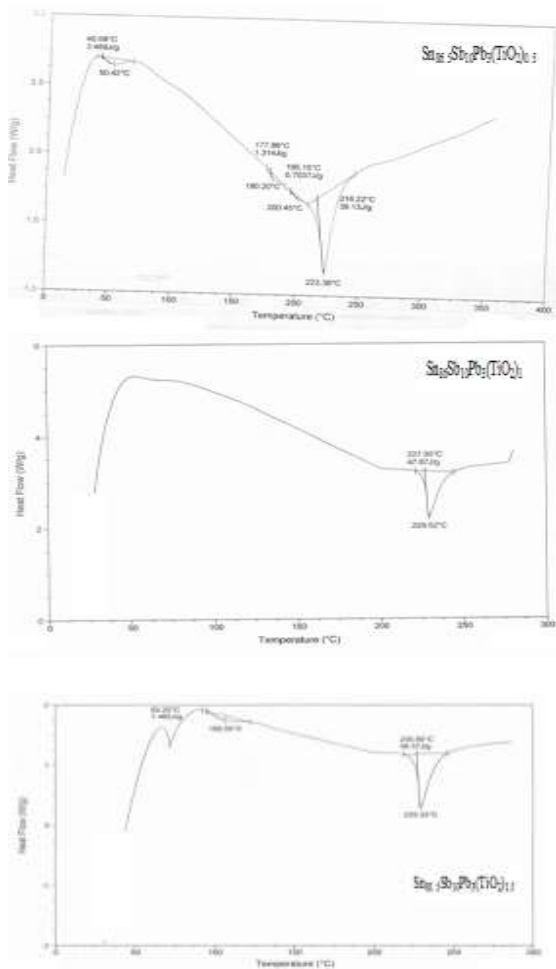


Figure 4:- DSC of  $\text{Sn}_{87-x}\text{Sb}_{10}\text{Pb}_3(\text{TiO}_2)_x$  alloys

**Effect of adding  $\text{TiO}_2$  nanoparticles on structure of Sn-Al alloy**

X-ray diffraction patterns of  $\text{Sn}_{80-x}\text{Al}_{20}(\text{TiO}_2)_x$  ( $x=0.5, 1$  and  $1.5$  wt. %) alloys have lines corresponding to  $\beta$ - Sn and Al phases as shown in Figure 5. X-ray analysis show that, adding  $\text{TiO}_2$  to  $\text{Sn}_{80}\text{Al}_{20}$  alloy caused a change in Sn matrix such as lattice parameters and formed crystal structure (crystallinity, crystal size and the orientation) as seen in Table 5 (a and b). That is because  $\text{TiO}_2$  nanoparticles dissolved in Sn matrix formed a solid solution and other accumulated particles formed a traces of phases.

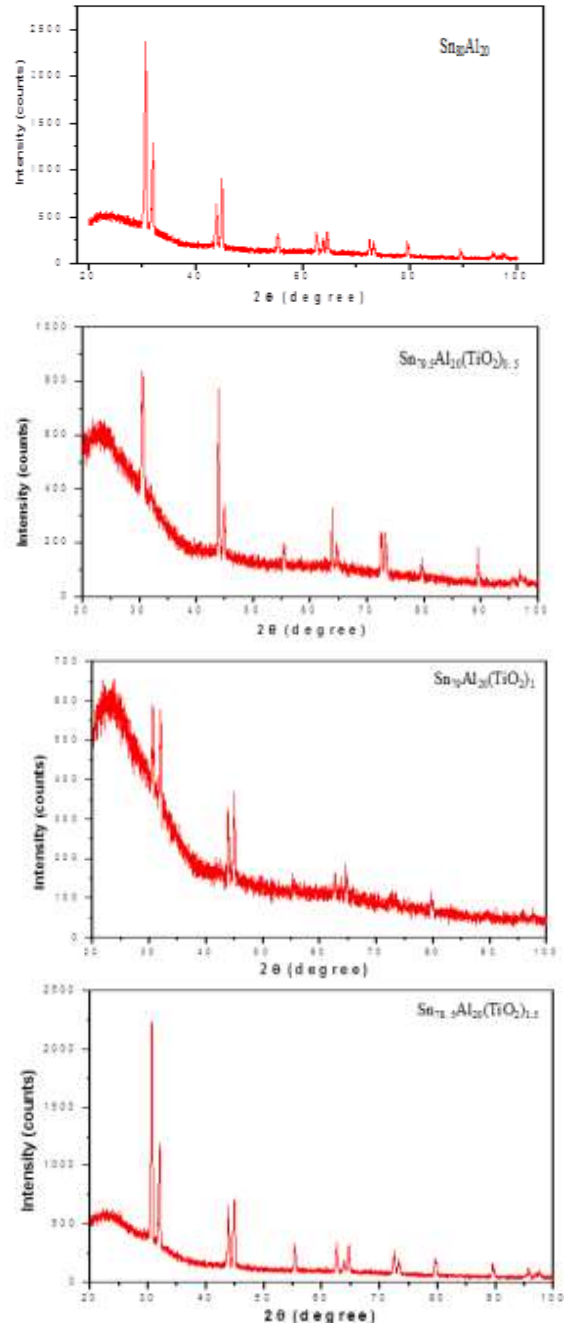


Figure 5:- x-ray diffraction patterns of  $\text{Sn}_{80-x}\text{Al}_{20}(\text{TiO}_2)_x$  alloys

73.45	1.28925	6.09	0.09	Sn	411
79.7057	1.20206	11.97	0.576	Sn	321
89.61	1.094	4.68	0.09	Sn	432
95.67	1.0401	3.28	0.09	Sn	103
97.69	1.02391	7.02	0.09	Sn	521

Table 5a:- x-ray diffraction analysis of  $\text{Sn}_{80-x}\text{Al}_{20}(\text{TiO}_2)_x$  alloys

$\text{Sn}_{80}\text{Al}_{20}$					
2 $\theta$	d Å	Int.%	FWHM	Phase	hkl
30.5888	2.92025	100	0.12	Sn	200
30.6656	2.92035	84.96	0.096	Sn	200
31.9935	2.79516	46.62	0.216	Sn	101
43.7803	2.0661	22.91	0.168	Sn	220
44.8271	2.02025	33.94	0.12	Al	200
55.2821	1.66037	9.25	0.432	Sn	301
62.448	1.48596	9.2	0.24	Sn	112
63.7441	1.45883	6.57	0.288	Sn	400
64.4962	1.44363	10.04	0.24	Al/Sn	220/321
72.3591	1.30489	7.2	0.192	Sn	411
73.0968	1.29353	6.01	0.336	Sn	411
79.4138	1.20574	7.3	0.24	Sn	312
89.3336	1.09576	4.52	0.192	Sn	431
95.6292	1.03957	1.42	0.768	Sn	103
97.3885	1.02543	2.57	0.288	Sn	521

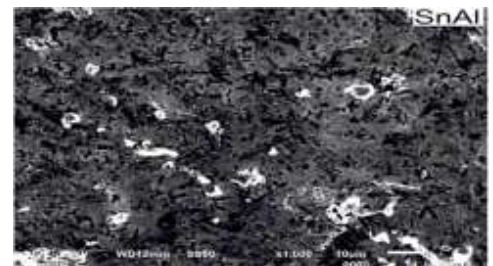
$\text{Sn}_{78.5}\text{Al}_{20}(\text{TiO}_2)_{1.5}$					
2 $\theta$	Åd	Int.%	FWHM	Phase	hkl
30.6183	2.91991	100	0.2558	Sn	200
32.0071	2.79632	45.14	0.2362	Sn	101
43.9365	2.06082	23.02	0.2558	Sn	220
44.8952	2.01901	30.74	0.2952	Al	211
55.3468	1.65996	10.96	0.2558	Sn	301
62.5078	1.48591	11.37	0.2362	Sn	112
63.8614	1.45764	4.34	0.1968	Sb	107
64.6256	1.44224	10.87	0.2165	Al/Sn	220/321
72.3939	1.30543	8.51	0.1968	Sb	018
73.2067	1.29293	5.95	0.1771	Sn	411
79.4578	1.20618	6.76	0.1771	Sn	321
89.3848	1.09617	4.78	0.1968	Sn	432
95.5964	1.04071	3.69	0.1771	Sn	103
97.5817	1.02391	1.68	0.576	Sn	521

$\text{Sn}_{79.5}\text{Al}_{20}(\text{TiO}_2)_{0.5}$					
2 $\theta$	d Å	Int.%	FWHM	Phase	hkl
30.378	2.94246	63.71	0.2362	Sn	200
31.9942	2.79742	31.75	0.5987	Sn	101
43.8632	2.06409	100	0.2165	Sn	220
44.8424	2.02127	28.31	0.3542	Al	211
55.3888	1.6588	12.76	0.3542	Sn	301
62.57	1.48458	4.01	0.09	Sn	112
63.8227	1.45843	25.99	0.1771	Sn	400
64.6647	1.44146	12.5	0.3149	Al/Sn	220/321
72.4103	1.30409	22.83	0.192	Sn	420
73.158	1.29367	22.73	0.1771	Sn	411
79.5208	1.20538	9.17	0.3149	Sn	321
89.4656	1.09539	17.47	0.1771	Sn	431
95.6294	1.04043	2.83	0.4723	Sn	103
96.8422	1.02975	4.62	0.576	Sn	521

$\text{Sn}_{79}\text{Al}_{20}(\text{TiO}_2)_1$					
2 $\theta$	Åd	Int.%	FWHM	Phase	hkl
30.6095	2.92074	100	0.2755	Sn	200
31.9936	2.79747	97.65	0.2362	Sn	101
43.9771	2.05901	67.42	0.2165	Sn	220
45.0299	2.01329	74.49	0.3346	Sn	211
55.41	1.65822	11.24	0.09	Sn	301
62.6126	1.48368	22.27	0.2362	Sn	112
64.6723	1.44131	25.72	0.2362	Al/Sn	220/321
72.67	1.30115	10.3	0.09	Sn	420

Table 5b:- lattice parameters and crystal size of  $\beta$ -Sn in  $\text{Sn}_{80-x}\text{Al}_{20}(\text{TiO}_2)_x$  alloys

Alloys	a Å	c Å	V Å <sup>3</sup>	$\tau$ Å
$\text{Sn}_{80}\text{Al}_{20}$	5.841	3.19	108.65	461.64
$\text{Sn}_{79.5}\text{Al}_{20}(\text{TiO}_2)_{0.5}$	5.88	3.10	106.42	390.49
$\text{Sn}_{79}\text{Al}_{20}(\text{TiO}_2)_1$	5.84	3.16	107.69	689.284
$\text{Sn}_{78.5}\text{Al}_{20}(\text{TiO}_2)_{1.5}$	5.84	3.17	108.08	432.55



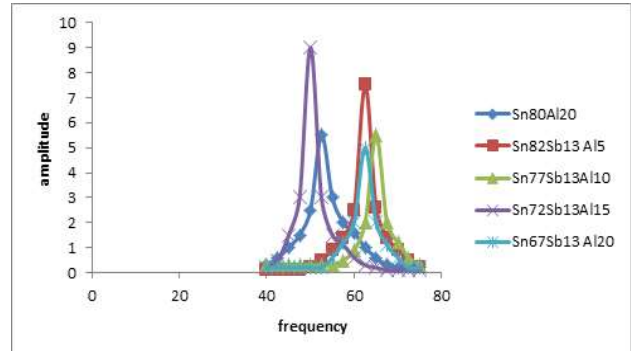
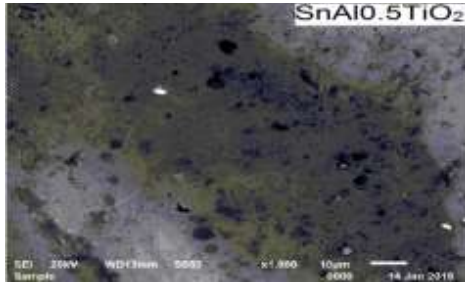


Figure 7:- resonance curves of  $\text{Sn}_{80-x}\text{Al}_{20}(\text{TiO}_2)_x$  alloys

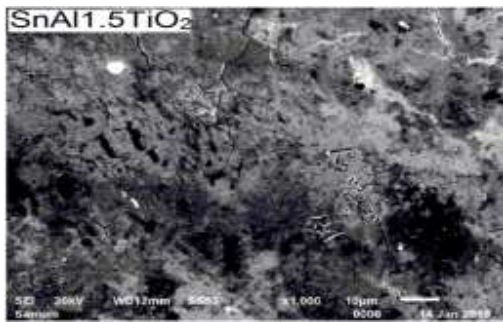


Figure 6:- SEM of  $\text{Sn}_{80-x}\text{Al}_{20}(\text{TiO}_2)_x$  alloys

### Effect of adding $\text{TiO}_2$ nanoparticles on mechanical properties of Sn- Al alloy

Elastic moduli of  $\text{Sn}_{80-x}\text{Al}_{20}(\text{TiO}_2)_x$  alloys are listed in Table 6. Elastic modulus of  $\text{Sn}_{80}\text{Al}_{20}$  alloy increased after adding different ratio from  $\text{TiO}_2$  nanoparticles. The  $\text{Sn}_{78.5}\text{Al}_{20}(\text{TiO}_2)_{1.5}$  alloy has highest elastic modulus.

The resonance curves  $\text{Sn}_{80-x}\text{Al}_{20}(\text{TiO}_2)_x$  alloys are shown in Figure 7. Calculated internal friction and thermal diffusivity of  $\text{Sn}_{80-x}\text{Al}_{20}(\text{TiO}_2)_x$  alloys are listed in Table 6. Internal friction of  $\text{Sn}_{80}\text{Al}_{20}$  alloy increased after adding different ratio from  $\text{TiO}_2$  nanoparticles. The  $\text{Sn}_{78.5}\text{Al}_{20}(\text{TiO}_2)_{1.5}$  alloy has high internal friction value.

Table 6:- elastic moduli, internal friction and thermal diffusivity of  $\text{Sn}_{80-x}\text{Al}_{20}(\text{TiO}_2)_x$  alloys

Alloys	E GPa	$\mu$ GPa	B GPa	$Q^{-1}$	$D_{th} \times 10^7$ ( $\text{m}^2/\text{sec}$ )
$\text{Sn}_{80}\text{Al}_{20}$	31.85	11.73	37.38	0.011	10.89
$\text{Sn}_{79.5}\text{Al}_{20}(\text{TiO}_2)_{0.5}$	37.6	13.9	44	0.024	24.6
$\text{Sn}_{79}\text{Al}_{20}(\text{TiO}_2)_1$	38.9	14.3	45.4	0.0227	60.97
$\text{Sn}_{78.5}\text{Al}_{20}(\text{TiO}_2)_{1.5}$	40.8	15	47.4	0.0228	9.60

Vickers hardness of  $\text{Sn}_{80-x}\text{Al}_{20}(\text{TiO}_2)_x$  alloys at 10 gram force and indentation time 5 sec are shown in Table 7. The minimum shear stress ( $\tau_m$ ) value of  $\text{Sn}_{80-x}\text{Al}_{20}(\text{TiO}_2)_x$  alloys was calculated then listed in Table 7. Little variation occurred in Vickers hardness of  $\text{Sn}_{80}\text{Al}_{20}$  alloy after adding  $\text{TiO}_2$  nanoparticles.

Table 7:- Vickers hardness and minimum shear stress of  $\text{Sn}_{80-x}\text{Al}_{20}(\text{TiO}_2)_x$  alloys

Alloys	$H_v$ $\text{kg}/\text{mm}^2$	$\mu_n$ $\text{kg}/\text{mm}^2$
$\text{Sn}_{80}\text{Al}_{20}$	$36.43 \pm 2.7$	14.33
$\text{Sn}_{79.5}\text{Al}_{20}(\text{TiO}_2)_{0.5}$	$35.77 \pm 1.9$	11.80
$\text{Sn}_{79}\text{Al}_{20}(\text{TiO}_2)_1$	$37.88 \pm 2.2$	12.50
$\text{Sn}_{78.5}\text{Al}_{20}(\text{TiO}_2)_{1.5}$	$38.92 \pm 3.1$	12.84

### Effect of adding $\text{TiO}_2$ on thermal properties and electrical resistivity of Sn-Al alloy

Figure 8 shows DSC thermographs for  $\text{Sn}_{80-x}\text{Al}_{20}(\text{TiO}_2)_x$  alloys. Little variation occurred in exothermal peak of  $\text{Sn}_{80}\text{Al}_{20}$  alloy. The melting temperature and other thermal properties of  $\text{Sn}_{80-x}\text{Al}_{20}(\text{TiO}_2)_x$  alloys are listed in Table 8. Melting temperature of  $\text{Sn}_{80}\text{Al}_{20}$  alloy increased after adding  $\text{TiO}_2$  nanoparticles.

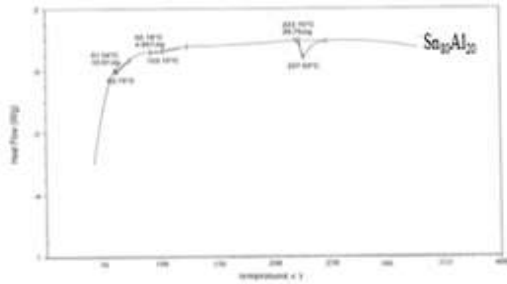
Electrical resistivity and calculated thermal conductivities of  $\text{Sn}_{80-x}\text{Al}_{20}(\text{TiO}_2)_x$  alloys are listed in Table 8. Electrical resistivity of  $\text{Sn}_{80}\text{Al}_{20}$  alloy varied after adding  $\text{TiO}_2$  nanoparticles. That is because  $\text{TiO}_2$  nanoparticles dissolved in the Sn matrix playing as scattering center for conduction electrons caused a change in Sn matrix.

Table 8:- electric resistivity and other thermal properties of  $\text{Sn}_{80-x}\text{Al}_{20}(\text{TiO}_2)_x$  alloys

Alloys	$\rho \times 10^{-6}$ $\Omega \cdot \text{cm}$	K W $\text{m}^{-1}\text{K}^{-1}$	$C_p \times 10^3$ J/g. $^\circ\text{C}$	$\Delta S$ J/g. $^\circ\text{C}$	Melting point $^\circ\text{C}$
$\text{Sn}_{80}\text{Al}_{20}$	67.3	1.21	0.723	0.122	227.03

$\text{Sn}_{79.5}\text{Al}_{20}(\text{TiO}_2)_{0.5}$	137.30	2.1	3.74	0.198	228.22
$\text{Sn}_{79}\text{Al}_{20}(\text{TiO}_2)_1$	77.76	2.31	2.85	0.190	228.92
$\text{Sn}_{78.5}\text{Al}_{20}(\text{TiO}_2)_{1.5}$	68.40	3.27	3.34	0.2	229.63

Figure 8:- DSC of  $\text{Sn}_{80-x}\text{Al}_{20}(\text{TiO}_2)_x$  alloys

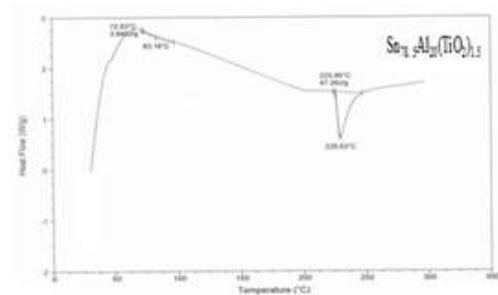
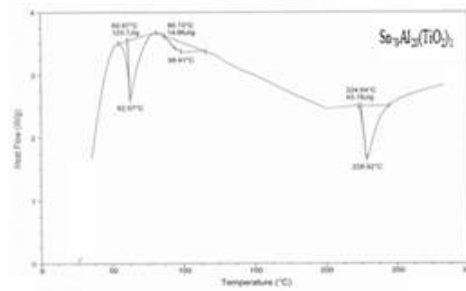
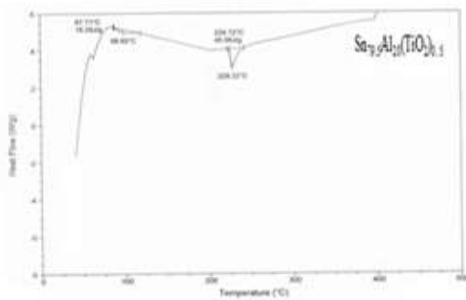


## Conclusion

Structure of  $\text{Sn}_{87}\text{Sb}_{10}\text{Pb}_3$  and  $\text{Sn}_{80}\text{Al}_{20}$  alloys changed after adding  $\text{TiO}_2$  nanoparticles. Elastic modulus and Vickers hardness of  $\text{Sn}_{87}\text{Sb}_{10}\text{Pb}_3$  and  $\text{Sn}_{80}\text{Al}_{20}$  alloys increased after adding  $\text{TiO}_2$  nanoparticles. Internal friction and melting temperature of  $\text{Sn}_{87}\text{Sb}_{10}\text{Pb}_3$  alloy decreased but internal friction and melting temperature of  $\text{Sn}_{80}\text{Al}_{20}$  alloy increased after adding  $\text{TiO}_2$  nanoparticles. The  $\text{Sn}_{85.5}\text{Sb}_{10}\text{Pb}_3(\text{Ti}_2\text{O})_{1.5}$  alloy has best properties for automotive industry. Also  $\text{Sn}_{78.5}\text{Al}_{20}(\text{Ti}_2\text{O})_{1.5}$  alloy has best properties for marine applications.

## References

- [1] Forrester P. G, Met. Rev. 5 (1960) 507
- [2] Pratt G. C, Int. Met. Rev. 18 (1973) 62
- [3] Forrester P. G, Curr. Engg. Pract 3 (1961) 4
- [4] Tegart W. I. M, Elements of mechanical metallurgy (New York: The MacMillan Co.) (1966) 91
- [5] Desaki T, Goto Y, Kamiya S, JSAE Rev. 21 (2000) 321
- [6] Lepper K, James M, Chashechkina J, Rigney D. A, Wear 46 (1997) 203
- [7] Perrin C, S. Harris, McCartney D. G, Syngellakis S, Reed P. A, in: J.F. Morton, B.C. Muddle (Eds.), Mater. Forum 28 (2004) 1371
- [8] Kong C. J, Brown P. D, S, Harris J, McCartney D. G, Mater. Sci. Eng. A 403 (2005) 205
- [9] Ning X. J, Jang J. H, Kim H. J, Li C. J, C. Lee, Surf. Coat. Technol. 202 (2008) 1681
- [10] Ning X. J, Kim J. H, Kim H. J, Lee C, Applied Surface Science 255 (2009) 3933
- [11] Pathak J. P and Mohan S, Bull. Mater. Sci. 26:3 (2003) 315
- [12] Kama M, El-Bediwi A and El-Shobaki M, Radia. Eff. Def. Sol. 161 (2006) 549
- [13] Bora M. O, Coban O, Sinmazcelik T, Gunay V, Zeren M, Mater. Design 31 (2010) 2707
- [14] El- Bediwi A. B, El Said Gouda, Kamal M, AMSE, 65, n° 1, Modeling C- 2004
- [15] Kamal M, Abdel-Salam A, Pieri J. C, J. Mater. Sci. 19 (1984) 3880
- [16] El-Bediwi A, Lashin A, Mossa M, Kamal M, Mater. Sci. Eng. A 528 (2011) 3568
- [17] E Schreiber, Anderson O. L and Soga N, Elastic constant and their measurements, McGraw-Hill, New York, (1973) 82
- [18] Timoshenko S and Goddier J. N, "Theory of elasticity, 2<sup>nd</sup> Ed", McGraw-Hill, New York, (1951) 277
- [19] Nuttall K, J. Inst. Met. 99 (1971) 266



# Optimization of Thermal Friction Drilling Process Based on Taguchi Method and Fuzzy Logic Technique

Sara A. El-Bahloul  
Mansoura University  
Faculty of Engineering  
Mansoura, Egypt

Hazem E. El-Shourbagy  
Mansoura University  
Faculty of Engineering  
Mansoura, Egypt

Tawfik T. El-Midany  
Mansoura University  
Faculty of Engineering  
Mansoura, Egypt

**Abstract:** The main purpose of this research is to study the optimal process parameters for thermal friction drilling process on AISI 304 stainless steel. The experiments were conducted based on Taguchi experimental design method, and the multiple performance characteristics correlated with the resultant axial force, radial force, hole diameter dimensional error, roundness error, and bushing length, were investigated by fuzzy logic technique. The significant process parameters that most intensively affected the multiple performance characteristics and the optimal combination levels of process parameters were determined through the analysis of variance and the response graph. A test rig was manufactured at Shoman Company – Egypt to perform the experimental work, and the tools were offered by Flowdrill Company – Germany. Experimental results confirm that this approach is simple, effective and efficient for simultaneous optimization of multiple quality characteristics in thermal friction drilling process, as the bushing length produced is more than five times the workpiece thickness.

**Keywords:** Thermal friction drilling; Optimization; Process parameters; Taguchi; Fuzzy logic; Bushing length

## 1. INTRODUCTION

Taguchi method is one of the simplest and effective solution for parameter design and experimental planning [1, 2]. It analyzes the influence of parameter variation to performance characteristics. Thereby, an optimal result can be obtained so that the sensitivity of performance characteristics in respect to parameter variation. Several research works have successfully applied this method to investigate the performance characteristics of processes. However, Taguchi method has shown some drawbacks in dealing with the problems of multiple performance characteristics [3, 4].

The theory of fuzzy logics, initiated by Zadeh in 1965 [5], has proven to be useful for dealing with uncertain and vague information. Since the definition of performance characteristics used for this research such as lower-the-better, higher-the-better, and nominal-the-better contains a certain degree of uncertainty and vagueness. Therefore, in the present work fuzzy logics can be a proper basis to perform the optimization procedure with complicated multiple performance characteristics.

Thermal friction drilling is a nontraditional drilling method that utilizes the heat generated from the friction interface between a rotating conical tool and the workpiece, and the heat will soften the workpiece and facilitate the tool to penetrate into the workpiece plate. Since it is no-chip process, the surface of the drilled hole would not be damaged by the burr extrusion during the drilling process. Therefore, tool service life could be increased, and the processing elapsed time and drilling cost would be intensively reduced. Another important feature of thermal friction drilling is that it could form a bushing that can provide a longer contact area, which can bear a shaft firmly as well as taped to create an internal screw without welding a nut. This is a unique feature which cannot be achieved by common drilling processes [6].

Following recent technological developments, stainless steel materials with anti-oxidizing, anticorrosive, and shiny surface features and outstanding characteristics like high toughness, high work-hardening coefficient, and low temperature conductivity have been applied in electronic, biochemical, and medical instrumentation equipment. Although these outstanding features reveal the distinguished advantages to extend its applications in

modern industries, stainless steel is hard to process and results in a serious tool wear and a rough surface of a part in machining process. The novel thermal friction drilling process needs a further and comprehensive study to understand the effects of drilling performance on stainless steels [7].

Referred to thermal friction drilling, there are recently few related research works. In this respect, Miller et al. [8] applied friction drilling to characterize the microstructures and indentation hardness changes in the friction drilling of carbon steel, alloy steel, aluminum, and titanium. Miller et al. [9] suggested that pre-heating the brittle material (cast metal) workpiece and using high speed drilling condition could generate a cylindrical shaped bushing without significant radial fracture. Lee et al. [10] had successfully applied friction drilling for machining cast superalloy IN-713LC to assess the roundness, the surface roughness, and the hardness of machined-hole-wall. Lee et al. [11] utilized tungsten carbide drills to investigate the benefits of coating on machining AISI 304 stainless steel, and the experimental results showed that the coated drills revealed less tool wear than uncoated ones. Chow et al. [12] conducted the experiments to explore the optimal tool friction angle and friction contact area ratio on AISI304 stainless steel correlated with surface roughness and bushing length. From those works, the optimal machining parameters combination for friction drilling process neither explored nor discussed the important issues such as the geometric shape of the drills and cutting parameters that will have effects on the resultant axial force, radial force, hole diameter dimensional error, roundness error, or bushing length.

The main purpose of this paper is to present the optimization of the thermal friction drilling process parameters; namely, tool cylindrical region diameter ( $d$ ), friction angle ( $\beta$ ), friction contact area ratio (FCAR), workpiece thickness ( $t$ ), feed rate (FR), and rotational speed (RS), on austenite stainless steel (AISI 304). Thus, the axial force (AF), radial force (RF), hole diameter dimensional error (DE), roundness error (RE), and bushing length (BL) together were measured, and the optimal combination levels of process parameters were also explored and proved by a confirmation test. Thus, the performance of thermal friction

drilling process on difficult-to-machine materials such as stainless steel would be ascertained to fit requirements of modern industrial applications.

## 2. EXPERIMENTAL APPARATUS AND DESIGN

Figure 1 shows the test rig that is designed to carry out the experimental work. The test rig is manufactured at Shoman Company – Egypt. It has two induction motors, one for performing high rotational speed up to 4500 rpm, and the other to get feed rate up to 200 mm/min. The tool is held by standard collets. Total of 18 thermal friction tools are used to perform all experiments. The tools are offered by Flowdrill Company – Germany. They are made of uncoated tungsten carbide.

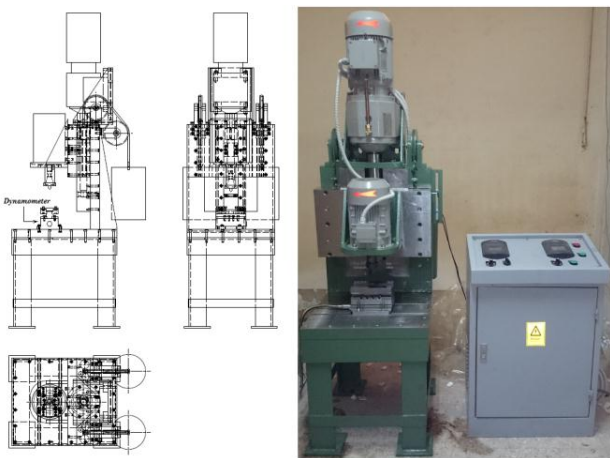


Figure. 1 The test rig

Three values for each of the six parameters are selected, as shown in Table 1. In this respect, no research work had combined six parameters together. In this study, an orthogonal array L18 [13] is applied to design the experiments. Each process parameter is assigned to a column and 18 process parameter combinations are required, as shown in Table 2.

Table 1. Process parameters and their levels

Process Parameter	Unit	Level 1	Level 2	Level 3
d	mm	5.4	7.3	9.2
$\beta$	degree	30°	45°	60°
FCAR	—	50 %	75 %	100 %
t	mm	1	2	3
RS	rpm	1500	2500	3500
FR	mm/min	60	100	140

The AF and RF were measured by a multi-component dynamometer (type 9257B). The DE and RE were measured by a coordination measuring machine (Status CMM). The BL was measured by a micro Vernier.

## 3. ANALYSIS AND DISCUSSION

Figure 2 illustrates the optimal process parameters determination steps according to Taguchi method and fuzzy logic technique.

### 3.1. Taguchi Method

To obtain the optimal machining performance, the minimum values of AF, RF, DE, and RE is desired. Hence, the smaller-the-better signal-to-noise (S/N) ratio is adopted, which is expressed in

Equation 1. Also, to get the maximum BL, the larger-the-better S/N ratio is used and can be expressed in Equation 2 [1].

Table 2. Experimental layout of L18 orthogonal array

Exp. No.	d (mm)	$\beta$ (degree)	FCAR (%)	t (mm)	FR (mm/min)	RS (rpm)
1	5.4	30	50	1	60	2500
2	5.4	30	75	3	140	1500
3	5.4	45	50	2	100	1500
4	5.4	45	100	1	140	3500
5	5.4	60	75	2	60	3500
6	5.4	60	100	3	100	2500
7	7.3	30	100	1	100	1500
8	7.3	30	100	2	60	3500
9	7.3	45	50	3	140	3500
10	7.3	45	75	2	100	2500
11	7.3	60	50	3	60	1500
12	7.3	60	75	1	140	2500
13	9.2	30	50	2	140	2500
14	9.2	30	75	3	100	3500
15	9.2	45	75	1	60	1500
16	9.2	45	100	3	60	2500
17	9.2	60	50	1	100	3500
18	9.2	60	100	2	140	1500

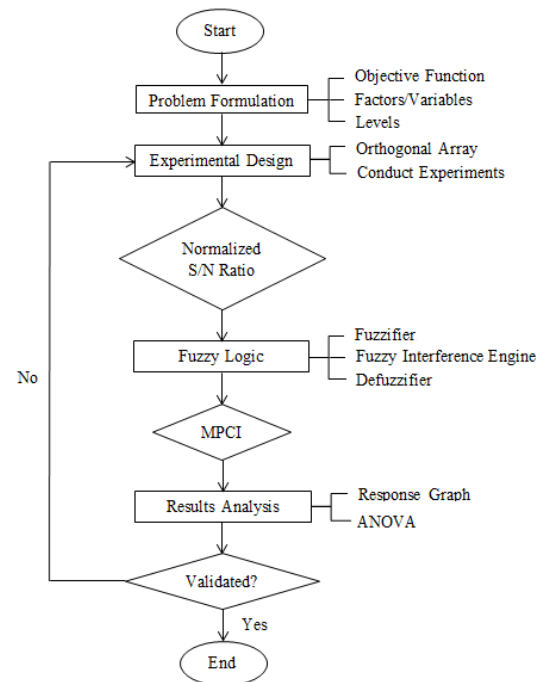


Figure 2. The optimal process parameters determination steps flow chart

$$S/N = -10 \log \frac{\sum_{i=1}^n y_i^2}{n} \quad (1)$$

$$S/N = -10 \log \frac{\sum_{i=1}^n y_i^{-2}}{n} \quad (2)$$

where  $y_i$  is the measured quality value, and  $n$  is the number of trails for each experiment ( $n = 3$  trails). Since the S/N ratios for the AF, RF, DE, RE, or BL are in different ranges, the S/N ratios are normalized to the range of 0–1. The normalized equation is expressed as [3]:

$$N\eta_p = \frac{(S/N)_p - (S/N)_{\min}}{(S/N)_{\max} - (S/N)_{\min}} \quad (3)$$

where  $N\eta_p$  is the normalized S/N ratio,  $(S/N)_p$  is the value of S/N for each experiment number  $p$ ,  $(S/N)_{\max}$  and  $(S/N)_{\min}$  are the maximum and minimum values of S/N for all experiments. Table 3 shows the resultant S/N and  $N\eta_p$  for the AF, RF, and DE. Noteworthy, the experiments 2, 11, and 18 didn't complete as

shown in Figure 3, because these experiments performed under the lowest rotational speed with higher workpiece thickness, so the heat produced due to friction is insufficient to completely perform the experiment.

**Table 3. S/N ratios and  $N\eta_p$**

Exp. No.	AF		RF		DE		RE		BL	
	S/N	$N\eta_p$	S/N	$N\eta_p$	S/N	$N\eta_p$	S/N	$N\eta_p$	S/N	$N\eta_p$
1	-50.07	1.00	-37.44	1.00	37.84	1.00	34.92	0.43	14.12	0.22
2	-	-	-	-	-	-	-	-	-	-
3	-59.72	0.37	-43.74	0.47	24.35	0.39	33.32	0.37	16.08	0.47
4	-51.68	0.89	-40.64	0.73	29.08	0.60	50.06	1.00	12.45	0.00
5	-56.66	0.57	-43.85	0.46	22.09	0.28	30.06	0.24	16.17	0.48
6	-64.65	0.05	-48.91	0.03	19.99	0.19	34.30	0.40	17.10	0.6
7	-51.13	0.93	-39.93	0.79	26.58	0.49	38.76	0.57	14.13	0.22
8	-55.62	0.64	-41.12	0.69	20.13	0.19	24.92	0.05	17.25	0.62
9	-61.69	0.24	-44.74	0.38	23.42	0.34	29.88	0.24	18.79	0.81
10	-58.09	0.48	-42.74	0.55	27.81	0.54	29.14	0.21	17.16	0.60
11	-	-	-	-	-	-	-	-	-	-
12	-51.94	0.88	-40.62	0.73	25.53	0.44	43.8	0.76	13.69	0.16
13	-57.62	0.51	-45.42	0.33	23.38	0.34	25.55	0.07	18.57	0.78
14	-59.43	0.39	-49.27	0.00	15.88	0.00	23.66	0.00	20.25	1.00
15	-51.44	0.91	-40.57	0.73	21.18	0.24	32.08	0.32	15.00	0.33
16	-65.36	0.00	-46.6	0.23	16.59	0.03	25.95	0.09	20.15	0.99
17	-50.22	0.99	-42.67	0.56	23.98	0.37	30.51	0.26	15.95	0.45
18	-	-	-	-	-	-	-	-	-	-



**Figure 3. Uncompleted experiments**

### 3.2. Fuzzy Logic Technique

The fuzzy inference system has four parts, the fuzzifier, fuzzy rule base, fuzzy inference engine, and defuzzifier as shown in Figure 4. The fuzzifier transforms crisp input into suitable semantic fuzzy information. The fuzzy rule base stores the rules and knowledge required for solving related problems, and describes the relationship between system input and output. The fuzzy inference engine is the core of the fuzzy system, and simulates thinking and decision-making models of humans via approximate reasoning or fuzzy inference, and finds solutions to existing problems. The defuzzifier transforms fuzzy information inferred by the fuzzy inference engine into crisp output. The defuzzifier uses the center of gravity to transform fuzzy information into crisp output.

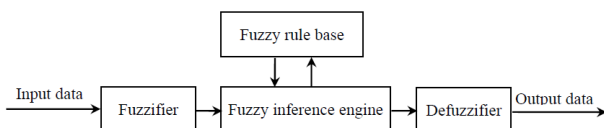


**Figure 4. Schematic of the fuzzy prediction system**

This study used MATLAB software to construct the inference model of the multiple performance characteristic index (MPCI), where  $N\eta_p$  of the AF, RF, DE, RE, and BL are taken as the input

variables for the fuzzy logic system, and the MPCI is the output variable. Table 4 shows the MPCI results and the total mean of the MPCI ( $\eta_m$ ) for all the 18 experiments.

**Table 4. Result for the MPCI**

Exp. No.	MPCI
1	0.76100
2	-
3	0.48600
4	0.63400
5	0.49900
6	0.24400
7	0.66400
8	0.43000
9	0.46900
10	0.50000
11	-
12	0.61800
13	0.50000
14	0.35000
15	0.60300
16	0.32900
17	0.62500
18	-
$\eta_m$	0.42844

Since the experimental design is orthogonal, it is then possible to separate out the effect of each process parameter at different levels. For example, the mean of MPCI for the cylindrical region

diameter parameter at levels 1, 2 and 3 can be calculated by averaging the MPCI for experiments 1-6, 7-12, and 13-18, respectively (Table 2), so the mean of MPCI for each level of the other process parameters can be computed in a similar manner. Then the results are summarized in a table called the response table (Table 5). Figure 5 shows the response graph for the MPCI mean. Basically, the larger the MPCI mean, the better the performance characteristic. However, the relative importance amongst the process parameters for the performance characteristic still needs to be known so that the optimal combinations of the process parameter levels can be determined more accurately.

**Table 5. MPCI mean response table**

Process Parameter	MPCI Mean			Max-Min	Rank
	Level 1	Level 2	Level 3		
d	0.4373	0.4468	0.4012	0.0457	6
$\beta$	0.4508	0.5035	0.331	0.1725	3
FCAR	0.4735	0.4283	0.3835	0.09	5
t	0.6508	0.4025	0.232	0.4188	1
FR	0.437	0.4782	0.3702	0.108	4
RS	0.2922	0.492	0.5012	0.209	2

### 3.3. Analysis of Variance

The statistical analysis of variance (ANOVA) is to investigate which process parameters significantly affect the performance

characteristics. This is accomplished by separating the total variability of the multi performance characteristics indexes, which is measured by the sum of the squared deviations from the total mean of the MPCI, into contributions by each of the process parameter and the error. The total sum of the squared deviations (SST) can be calculated as [13]:

$$SS_T = \sum_{j=1}^p (MPCI_j - \eta_m)^2 \quad (4)$$

where p is the number of experiments in the orthogonal array. SST is decomposed into two sources: the sum of the squared deviations due to each process parameter and the sum of the squared error. The percentage contribution by each of the process parameter in the total sum of the squared deviations can be used to evaluate the importance of the process parameter change on the performance characteristics. The results of ANOVA (Table 6) indicate that t and RS are the most significant process parameters in affecting the AF, RF, DE, RE, and BL together.

Based on the above discussion, the optimal process parameters combination is: d = 7.3 mm,  $\beta$  = 45°, FCAR = 50%, t = 1 mm, feed rate FR = 100 mm/min, and rotational speed RS = 3500 rpm, for the proposed experimental levels.

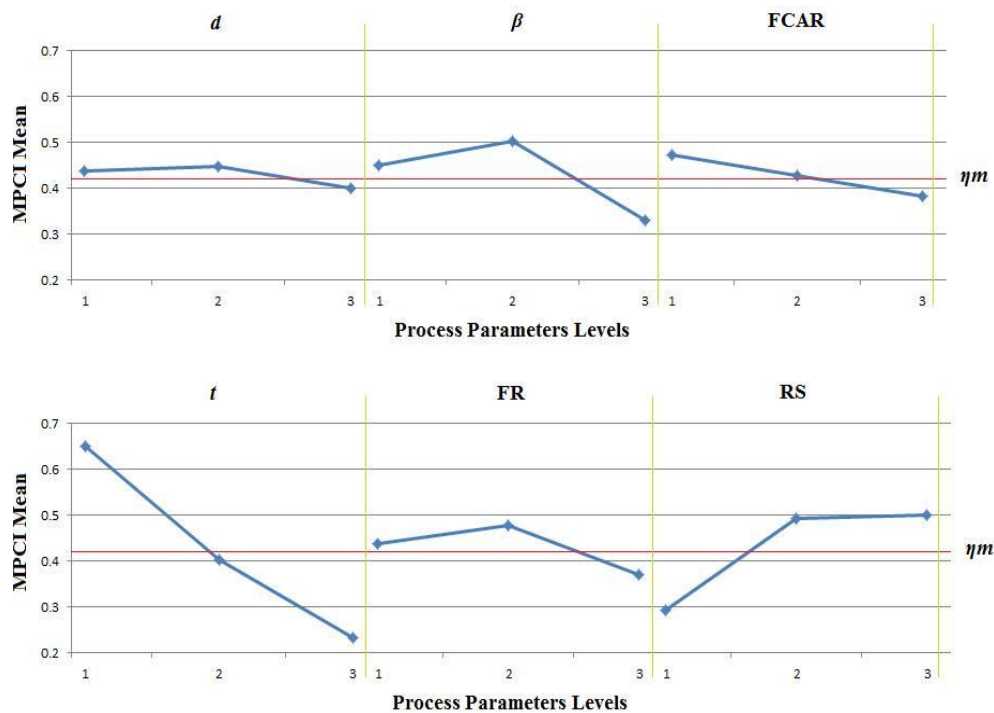


**Figure 5. MPCI mean response graph**

**Table 6. Result of ANOVA**

Process Parameters	Sum of Square	Contribution (%)
d	0.00697	0.7460
$\beta$	0.09378	10.037
FCAR	0.0243	2.6009
t	0.53232	56.975
FR	0.03565	3.8157
RS	0.1674	17.917

Error	0.07389	7.9086
Total	0.9343	100

### 3.4. Confirmation Test

Once the optimal level of the process parameters has been selected, the final step is to predict and verify the improvement of the performance characteristic using the optimal level of the process parameters. The predicted S/N ratio  $\hat{\eta}$  using the optimal level of the process parameters can be calculated as:

$$\bar{\eta} = \eta_m + \sum_{j=1}^q (\eta_j - \eta_m) \quad (5)$$

where  $\eta_j$  is the mean of the MPCFI at the optimal level, and  $q$  is the number of the process parameters that significantly affect the multiple performance characteristics. Table 7 displays the results of the confirmation experiment. This table indicates that the experimental observed values obtained from the optimal combination levels of process parameters were improved compared to the minimum trials mean results for each experiment of the performed 18 experiments at  $t = 1$  mm. Experiment number 17 achieved BL more than that of the optimal experiment, as it performed at  $d = 9.2$  mm, so more material is pushed leading to more BL, but still the BL produced in the optimal experiment more than five times the workpiece thickness. Also the DE produced in experiment number 1 is less than that of the optimal experiment, as it performed at smaller tool diameter  $d = 5.4$  mm so less error is produced, but still the increase in the DE at the optimal experiment is very small.

**Table 7. Results of the confirmation experiment**

Setting levels	Best Suitable Process Parameter Confirmation	
	Predicted	Experimental
MPCFI	$d2 - \beta2 - FCAR1 - t1 - FR2 - RS3$	
	0.72356	0.783
	Performed Experiments Results	
	Minimum of 1 mm experiments	Optimal experiment
AF	318.667 N	292 N
RF	74 N	50 N
DE	0.0092 mm	0.013 mm
RE	0.0031 mm	0.002 mm
BL	6.2733 mm	5.78 mm

#### 4. CONCLUSIONS

This paper has presented the use of Taguchi method and fuzzy logic technique for the optimization of the thermal friction drilling process of AISI 304 stainless steel. Experimental data and statistical results have supported the following conclusions:

- The workpiece thickness and the rotational speed are the most significant process parameters, which obviously affected the AF, RF, DE, RE, and BL together in thermal friction drilling for the proposed experimental levels.
- The optimal process parameters combination is:  $d = 7.3$  mm,  $\beta = 45^\circ$ ,  $FCAR = 50\%$ ,  $t = 1$  mm,  $FR = 100$  mm/min, and  $RS = 3500$  rpm, for the proposed experimental levels.
- The performance characteristics such as AF, RF, DE, RE, and BL are improved through this approach. The BL produced is more than five times the workpiece thickness.
- This study can be applied on the friction drilling of various malleable metals including mild steel, stainless steel, copper, brass, and aluminum to generate precision holes. Also different machining conditions can be considered, so as to build a Computer Aided Process Planning expert system of thermal friction drilling process with the goal of automation.

#### 5. ACKNOWLEDGEMENTS

The first author would like to acknowledge Flowdrill Company in Germany for offering the needed tools. Also she would like to acknowledge Shoman Company in Egypt for their great help and support in offering the facilities and tools needed to conduct this work.

#### 6. REFERENCES

- [1] Ross, P. 1988 Taguchi techniques for quality engineering: loss function, orthogonal experiments, parameter and tolerance design. second edition, McGraw-Hill book Co-Singapore Copyright © 1996, ISBN 0-07-114663-6.
- [2] Taguchi, G., Chowdhury, S., and Wu, Y. 2005 Taguchi quality engineering handbook. ISBN 0-471-41334-8, John Wiley & Sons, Inc.
- [3] Hsiang, S., and Lin Y. 2009 Optimization of the extrusion process for Magnesium alloy sheets using the fuzzy based Taguchi method. the Arabian journal for science and engineering, volume 34, number 1c.
- [4] Puri, Y., and Deshpande, N. 2004 Simultaneous optimization of multiple quality characteristics of WEDM based on fuzzy logic and Taguchi technique. Proceedings of the Fifth Asia Pacific Industrial Engineering and Management Systems Conference.
- [5] Yen, J., and Langari, R. 1999 Fuzzy Logic: intelligence, control, and information. Prentice hall, upper saddle river, New Jersey 07458, ISBN: 0-13-525817-0.
- [6] Wu, C., Fang, T., and Kuo, C. 2014 Atomistic simulation of nanodrilling mechanics and mechanism on Cu substrates. Appl. Phys. A, Materials science and processing, DOI 10.1007/s00339-014-8732-5.
- [7] Ku, W., Hung, C., Lee, S., and Chow, H. 2010 Optimization in thermal friction drilling for SUS 304 stainless steel. Springer-Verlag London Limited 2010, Int. J. Adv. Manuf. Technol. 53:935–944, DOI 10.1007/s00170-010-2899-5.
- [8] Miller, S., Tao, J., and Shih, A. 2005 Microstructural alterations associated with friction drilling of steel, aluminum, and titanium. JMEPEG 14:647-653 ©ASM International, DOI: 10.1361/105994905X645581 0599495.
- [9] Miller, S., Tao, J., and Shih, A. 2005 Friction drilling of cast metals. International Journal of Machine Tools & Manufacture 46 1526–1535, DOI 10.1016/j.ijmactools.2005.09.003.
- [10] Lee, S., Chow, H., and Yan, B. 2007 Friction drilling of IN-713LC cast superalloy. Materials and Manufacturing Processes, 22: 893–897, 2007, Copyright © Taylor & Francis Group, LLC, ISSN: 1042-6914 print/1532-2475 online, DOI: 10.1080/10426910701451697.
- [11] Lee, S., Chow, H., Huang, F., and Yan, B. 2008 Friction drilling of austenitic stainless steel by uncoated and PVD AlCrN- and TiAlN-coated tungsten carbide tools. International Journal of Machine Tools & Manufacture 49, 0890-6955/\$, Crown Copyright © Published by Elsevier Ltd., DOI: 10.1016/j.ijmactools.2008.07.012.
- [12] Ku, W., Chow, H., Lin, Y., Wang, D., and Yang, L. 2010 Optimization of thermal friction drilling using grey relational analysis. eAdvanced Materials Research Vols. 154-155 pp 1726-1738, Copyright © Trans. Tech. Publications, Switzerland DOI: 10.4028/www.scientific.net/AMR.154155.1726.
- [13] Tsai, P., Gilmour, S., and Mead, R. 2000 Projective three-level main-effects designs robust to model uncertainty. Biometrika, 87, 2 pp. 467-475 © Biometrika Trust printed in Great Britain.

# New Penta Bismuth Based Alloy for Shielding Blocks in Mega-Volt Radiotherapy

Abu Bakr El- Bediwi  
Metal Physics Lab., Physics  
Department, Faculty of Science,  
Mansoura University  
Mansoura, Egypt

Feryal Dawood  
Basic education college  
University of Diayala  
Iraq

Mustafa Kamal  
Metal Physics Lab., Physics  
Department, Faculty of Science,  
Mansoura University  
Mansoura, Egypt

**Abstract:** Microstructure, thermal, electrical and mechanical properties of penta Bi- Sn- Pb based alloys have been investigated. Matrix structure (Formed crystalline phases) and measured physical properties of Bi- Sn- Pb- In- X (X= Cd/or Zn) penta alloys changed with varying composition. The new penta fusible,  $\text{Bi}_{50}\text{Pb}_{15}\text{Sn}_{22}\text{Cd}_3\text{In}_{10}$ , alloy has best properties such as high density, low melting point and friendly environmental, (reduced toxicity elements Pb and Cd by 40% and 75%, compared used alloys), for shielding blocks in mega-volt radiotherapy. The melting temperature of  $\text{Bi}_{50}\text{Pb}_{15}\text{Sn}_{22}\text{Cd}_3\text{In}_{10}$  alloy is  $\sim 58^\circ\text{C}$  and its density is  $10.117\text{ gm/cm}^3$ . The elastic modulus of  $\text{Bi}_{50}\text{Pb}_{15}\text{Sn}_{22}\text{Cd}_3\text{In}_{10}$  is 29.03 Gpa. Vickers hardness and internal friction values of  $\text{Bi}_{50}\text{Pb}_{15}\text{Sn}_{22}\text{Cd}_3\text{In}_{10}$  alloy are  $9.72\text{ Kg/mm}^2$  and 0.085. The  $\text{Bi}_{50}\text{Pb}_{15}\text{Sn}_{22}\text{Cd}_3\text{In}_{10}$  alloy consists of rhombohedral Bi phase, tetragonal Sn phase, face centered cubic Pb phase, hexagonal Cd phase, face centered cubic In phase,  $\text{Pb}_7\text{Bi}_3$  and SnBi intermetallic compounds.

**Key words:** shielding blocks, fusible alloys, thermal and mechanical properties, electrical resistivity

## 1. INTRODUCTION

Over the past few years fusible alloys have become a hot subject because they are important for industrial and medical applications. Now is the time to understand the correlation between microstructure and physical properties of fusible alloys for solder, bearing and shielding blocks applications. There are an enormous number of alloys made by metals as bismuth, lead, tin and cadmium have in common the feature of a low melting point. In the past they were commonly known as Lipowitz's, Wood's, D'Arcet and Rose alloys and now they are known as Arconim's alloys. In our days other alloys having slightly different compositions in order to further improve their peculiarities had replaced them. Structure, growth properties and physical metallurgy of a series of Pb-Sn-Cd alloys containing up to 60- wt.% Bi and Pb-Sn-Bi were investigated [1]. The results showed that, formation of metastable crystalline phase in the range of composition investigated causes a pronounced increase in the electrical resistivity. Adding bismuth to PbCdSn had to the appearance of the crystalline metastable phase which produced a hardening effect [2]. Also bismuth atoms act as scattering centers and increasing their concentrations caused an enhancement of resistivity. The physical characteristics of Lipowitz's metal and bismuth-lead eutectic alloys as a shielding block for mega-voltage therapy machine were studied and analyzed. Internal friction of irradiated and non-irradiated alloys is sensitive to the chemical composition used alloys [3]. Structure, mechanical and electrical transport properties of  $\text{Pb}_{60}\text{Sn}_{38}\text{X}_2$  (X = Sb, Bi, or Ag in weight percent as ternary additions) were investigated. Ledbetter's theoretical values of the ratio of shear modulus to elastic modulus,  $\mu/E$ , are in a good agreement with the experimental results [4]. The crystalline metastable  $\chi(\text{Pb-Bi})$  phase was appeared in  $\text{Pb}_{50}\text{Sn}_{50-x}\text{Bi}_x$  ( $x= 30$  and  $50$  wt. %) alloys and the lowest value of Vickers hardness was attributed to the formation of intermediate metastable phases [5]. Mechanical and electrical properties of  $\text{PbBiSnCd}$  were dependence on tin content obtained [6]. The ductility of the binary Bi-Sn eutectic alloy has significantly improved by adding small amount Ag [7]. Metastable shift of the solubility limit in Sn-Bi alloys containing 15, 20 and 25 at. % bismuth was produced by splat quenching [8]. The effect of splat cooling on crystal structures and heats of formation of

non-equilibrium intermediate phases of Pb-Bi alloy was studied [9]. Solid solubility extension of Pb in Bi and formation and lattice parameter of several new metastable crystalline solid phases in Pb-Bi including complex Pb-Bi phases was reported [10]. The crystallographic relationship between the phases in the Cd-Zn eutectic alloys using standard x-ray techniques on selected areas of bulk eutectic specimens was examined [11]. Also the orientation characteristics of eutectic alloys of Bi-Cd, Cd-Sn, Sn-Zn and Al-Si were studied [12]. Microstructure, electrical, mechanical and thermal properties of rapidly solidified  $\text{Bi}_{58}\text{Sn}_{42}$  eutectic alloy have been investigated [13]. Thermal properties and microstructure of 58% Bi-42% Sn, 53% Bi-26% Sn-21% Cd, 70% In-30% Sn, 50% Sn-50% In and 3% Sn-37% Bi-10% In solder alloys have been studied and analyzed [14]. Attenuation coefficients, structure and physical properties of Bi-Pb-Sn fusible alloys were studied [15]. Microstructure, electrical, mechanical and thermal properties of melt spun bismuth-tin and bismuth-lead-tin eutectic alloys also investigated [16, 17]. Optical microscopy, X-ray diffractometry, double bridge method, Vickers microhardness testing and dynamic resonance techniques have been used to investigate structure, electrical resistivity, hardness, internal friction and elastic modulus of quenched Bi-Pb-Sn-Cd-Sb penta-alloys, Bi-Pb, Bi-Pb-Sn, Bi-Pb-Cd and Bi-Pb-Sn-Cd fusible alloys [18, 19]. The effect of the quenching rate on structure and some physical properties of the Pb-Sn-Cd melt spun fusible alloys have been investigated by El-Bediwi [20].

The aim of our research was to produce new bismuth based alloy with superior properties as shielding blocks in mega-volt radiotherapy

## 2. EXPERIMENTAL WORK

Using elements bismuth, tin, lead, indium, cadmium and zinc have a high purity, more than 99.95%. The used alloys,  $\text{Bi}_{50}\text{Pb}_{15}\text{Sn}_{22}\text{In}_{10}\text{X}_3$  and  $\text{Bi}_{50}\text{Pb}_{15}\text{Sn}_{28}\text{In}_4\text{X}_3$  (X=Cd or Zn), were molten in the muffle furnace. The resulting ingots were turned and re-melted several times to increase the homogeneity of the ingots. From these ingots, long ribbons of about 3-5 mm width and  $\sim 70\text{ }\mu\text{m}$  thickness were prepared as the test samples by directing a stream of molten alloy

onto the outer surface of rapidly revolving copper roller with surface velocity 31 m/s giving a cooling rate of  $3.7 \times 10^5$  k/s. The samples then cut into convenient shape for the measurements using double knife cutter. Structure of used alloys was performed using an Shimadzu x-ray diffractometer (DX-30, Japan) of Cu-K $\alpha$  radiation with  $\lambda=1.54056$  Å at 45 kV and 35 mA and Ni-filter in the angular range  $2\theta$  ranging from 20 to 100° in continuous mode with a scan speed 5 deg/min. Scanning electron microscope JEOL JSM-6510LV, Japan was used to study microstructure of used samples. The melting endotherms of used alloys were obtained using a SDT Q600 V20.9 Build 20 instrument. A digital Vickers micro-hardness tester, (Model-FM-7- Japan), was used to measure Vickers hardness values of used alloys. Internal friction  $Q^{-1}$  and the elastic constants of used alloys were determined using the dynamic resonance method [21- 23].

### 3. RESULTS AND DISCUSSIONS

#### Microstructure

X-ray diffraction patterns of  $\text{Bi}_{50}\text{Pb}_{15}\text{Sn}_{22}\text{In}_{10}\text{X}_3$  and  $\text{Bi}_{50}\text{Pb}_{15}\text{Sn}_{28}\text{In}_4\text{X}_3$  (X=Cd or Zn) alloys have lines corresponding to rhombohedral Bi phase, tetragonal Sn phase, face centered cubic Pb phase, hexagonal Cd phase, face centered cubic In phase,  $\text{Pb}_3\text{Bi}_3$  and SnBi intermetallic compounds as shown in Figure 1. X-ray analysis of  $\text{Bi}_{50}\text{Pb}_{15}\text{Sn}_{22}\text{In}_{10}\text{X}_3$  and  $\text{Bi}_{50}\text{Pb}_{15}\text{Sn}_{28}\text{In}_4\text{X}_3$  (X=Cd or Zn) alloys show that, the change in feature of formed phases (such as intensity, broadness of peak, miller indices, position ( $2\theta$ ), and area under peaks) correlates to the alloy composition. Lattice parameters, (a and c), and unit volume cell (V) of rhombohedral Bi phase in  $\text{Bi}_{50}\text{Pb}_{15}\text{Sn}_{22}\text{In}_{10}\text{X}_3$  and  $\text{Bi}_{50}\text{Pb}_{15}\text{Sn}_{28}\text{In}_4\text{X}_3$  (X=Cd or Zn) alloys were determined and then listed in Table 1a. Adding Cd/ or Zn to Bi- Pb- Sn- In alloys caused a little variation in Bi lattice parameters and unit cell volume. Crystal particle size of rhombohedral Bi phase in  $\text{Bi}_{50}\text{Pb}_{15}\text{Sn}_{22}\text{In}_{10}\text{X}_3$  and  $\text{Bi}_{50}\text{Pb}_{15}\text{Sn}_{28}\text{In}_4\text{X}_3$  (X=Cd or Zn) alloys are seen in Table 1b. Adding Cd to Bi- Pb- Sn- In alloys produced higher crystal size of Bi phase than Zn.

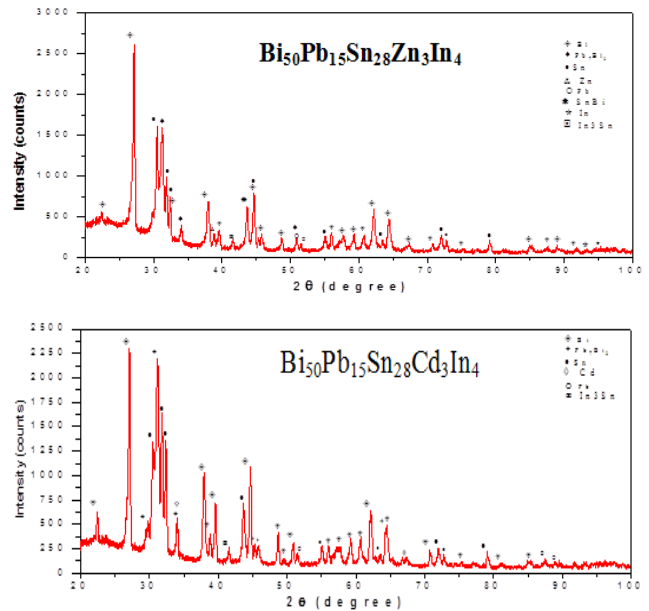


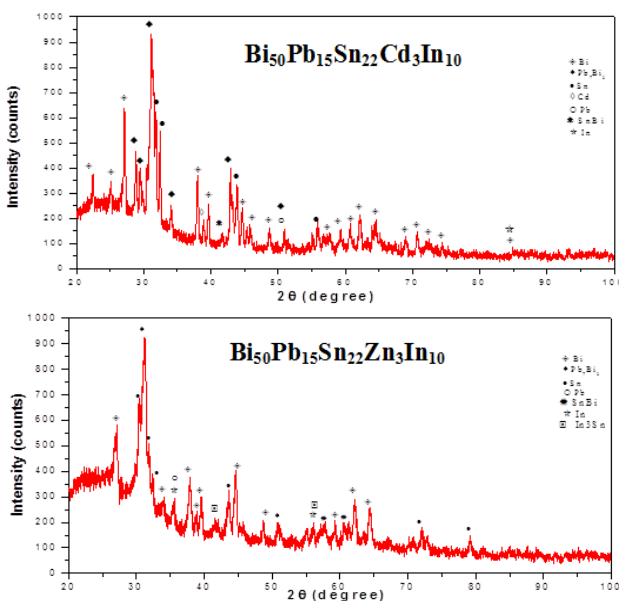
Figure 1:- x-ray diffraction patterns of penta Bi- Pb- Sn based alloys

Table 1a:-lattice parameters and unit cell volume of Bi in penta Bi- Pb- Sn based alloys

Samples	$a_{\text{rho}}$ Å	$c$ Å	$V$ Å <sup>3</sup>
$\text{Bi}_{50}\text{Pb}_{15}\text{Sn}_{22}\text{Cd}_3\text{In}_{10}$	4.748	11.87	70.766
$\text{Bi}_{50}\text{Pb}_{15}\text{Sn}_{22}\text{Zn}_3\text{In}_{10}$	4.816	12.106	71.962
$\text{Bi}_{50}\text{Pb}_{15}\text{Sn}_{28}\text{Cd}_3\text{In}_4$	4.754	11.886	70.994
$\text{Bi}_{50}\text{Pb}_{15}\text{Sn}_{28}\text{Zn}_3\text{In}_4$	4.753	11.879	71.014

Table 1b:- crystal particle size of  $\text{Bi}_{\text{rho}}$  in penta Bi- Pb- Sn based alloys

Samples	Particle size Å
$\text{Bi}_{50}\text{Pb}_{15}\text{Sn}_{22}\text{Cd}_3\text{In}_{10}$	357.64
$\text{Bi}_{50}\text{Pb}_{15}\text{Sn}_{22}\text{Zn}_3\text{In}_{10}$	264.646
$\text{Bi}_{50}\text{Pb}_{15}\text{Sn}_{28}\text{Cd}_3\text{In}_4$	372.43
$\text{Bi}_{50}\text{Pb}_{15}\text{Sn}_{28}\text{Zn}_3\text{In}_4$	339.46



Scanning electron micrographs, SEM, of  $\text{Bi}_{50}\text{Pb}_{15}\text{Sn}_{22}\text{In}_{10}\text{X}_3$  and  $\text{Bi}_{50}\text{Pb}_{15}\text{Sn}_{28}\text{In}_4\text{X}_3$  (X=Cd or Zn) alloys show heterogeneous structure as shown in Figure 2 and that agreed with x-ray analysis. Adding Cd/ or Zn to Bi- Pb- Sn- In alloys caused a change in matrix microstructure of Bi- Pb- Sn alloy.

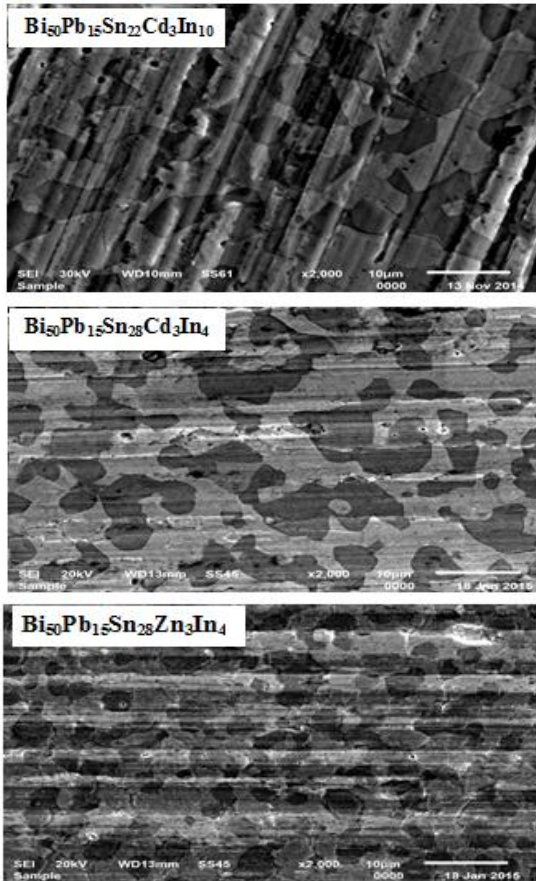


Figure 2:- SEM of penta Bi- Pb- Sn based alloys

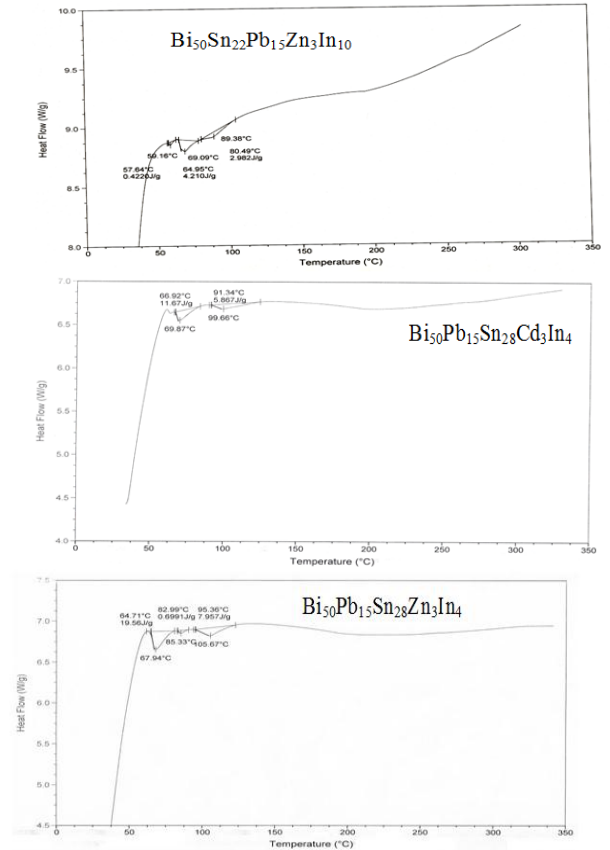


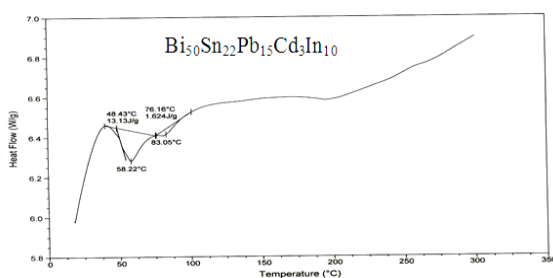
Figure 3:- DSC of penta Bi- Pb- Sn based alloys

### Thermal properties

Thermal analysis is often used to study solid state transformations as well as solid-liquid reactions. Figure 3 shows DSC thermographs of  $\text{Bi}_{50}\text{Pb}_{15}\text{Sn}_{22}\text{In}_{10}\text{X}_3$  and  $\text{Bi}_{50}\text{Pb}_{15}\text{Sn}_{28}\text{In}_4\text{X}_3$  ( $\text{X}=\text{Cd}$  or  $\text{Zn}$ ) alloys. Little variation occurred in exothermic peaks of  $\text{Bi}_{50}\text{Pb}_{15}\text{Sn}_{22}\text{In}_{10}\text{X}_3$  and  $\text{Bi}_{50}\text{Pb}_{15}\text{Sn}_{28}\text{In}_4\text{X}_3$  ( $\text{X}=\text{Cd}$  or  $\text{Zn}$ ) alloys after adding Cd/ or Zn. The melting temperature and other thermal properties of  $\text{Bi}_{50}\text{Pb}_{15}\text{Sn}_{22}\text{In}_{10}\text{X}_3$  and  $\text{Bi}_{50}\text{Pb}_{15}\text{Sn}_{28}\text{In}_4\text{X}_3$  ( $\text{X}=\text{Cd}$  or  $\text{Zn}$ ) alloys are listed in Table 2. Variation on melting temperature, specific heat, enthalpy and thermal conductivity of used alloys depend on its compositions.

Table 2:- melting point and other thermal properties of penta Bi- Pb- Sn based alloys

Samples	Melting point °C	$C_p$ J/g. °C	$\Delta S$ J/g. °C	K $\text{W.m}^{-1}.\text{K}^{-1}$
$\text{Bi}_{50}\text{Pb}_{15}\text{Sn}_{22}\text{Cd}_3\text{In}_{10}$	58.22	0.596	0.224	0.398
$\text{Bi}_{50}\text{Pb}_{15}\text{Sn}_{22}\text{Zn}_3\text{In}_{10}$	69.09	0.314	0.059	0.701
$\text{Bi}_{50}\text{Pb}_{15}\text{Sn}_{28}\text{Cd}_3\text{In}_4$	69.87	0.743	0.157	0.700
$\text{Bi}_{50}\text{Pb}_{15}\text{Sn}_{28}\text{Zn}_3\text{In}_4$	67.94	1.387	0.274	0.429



### Electrical resistivity

Plastic deformation raises the electrical resistivity as a result of the increased number of electron scattering centers. Also crystalline defects serve as scattering center for conduction electrons in metals, so the increase in their number raises the imperfection. The measured electrical resistivity of  $\text{Bi}_{50}\text{Pb}_{15}\text{Sn}_{22}\text{In}_{10}\text{X}_3$  and  $\text{Bi}_{50}\text{Pb}_{15}\text{Sn}_{28}\text{In}_4\text{X}_3$  ( $\text{X}=\text{Cd}$  or  $\text{Zn}$ ) alloys are shown in Table 3. Electrical resistivity of Bi- Pb- Sn- In alloys varied after adding Cd/ or Zn, which depend on alloys compositions.

Table 3:- electrical resistivity and electrical conductivity of penta Bi- Pb- Sn based alloys

Samples	$\rho \times 10^{-8} \Omega.m$	$\sigma \times 10^5 \Omega.m$
$Bi_{50}Pb_{15}Sn_{22}Cd_3In_{10}$	254.8	2.421
$Bi_{50}Pb_{15}Sn_{22}Zn_3In_{10}$	226.55	4.414
$Bi_{50}Pb_{15}Sn_{28}Cd_3In_4$	226.87	4.408
$Bi_{50}Pb_{15}Sn_{28}Zn_3In_4$	380.92	2.625

Table 5:- Vickers hardness and minimum shear stress of penta Bi- Pb- Sn based alloys

Alloys	$H_v \text{ kg/mm}^2$	$\mu_n \text{ kg/mm}^2$
$Bi_{50}Pb_{15}Sn_{22}Cd_3In_{10}$	$9.72 \pm 1.1$	3.21
$Bi_{50}Pb_{15}Sn_{22}Zn_3In_{10}$	$5.61 \pm 0.8$	1.85
$Bi_{50}Pb_{15}Sn_{28}Cd_3In_4$	$21.82 \pm 1.13$	7.2
$Bi_{50}Pb_{15}Sn_{28}Zn_3In_4$	$20.92 \pm 1.02$	6.9

### Mechanical properties

The elastic constants are directly related to atomic bonding and structure. Elastic moduli of  $Bi_{50}Pb_{15}Sn_{22}In_{10}X_3$  and  $Bi_{50}Pb_{15}Sn_{28}In_4X_3$  (X=Cd or Zn) alloys are listed in Table 4. Elastic modulus values of Bi- Pb- Sn- In alloys changed after adding Cd/ or Zn due to matrix structure change.

The resonance curves of  $Bi_{50}Pb_{15}Sn_{22}In_{10}X_3$  and  $Bi_{50}Pb_{15}Sn_{28}In_4X_3$  (X=Cd or Zn) alloys are shown in Figure 4. Calculated internal friction and thermal diffusivity  $Bi_{50}Pb_{15}Sn_{22}In_{10}X_3$  (X=Cd or Zn) alloys are listed in Table 4. Internal friction of Bi- Pb- Sn- In alloys varied after adding Cd/ or Zn.

Table 4:- elastic moduli, internal friction and thermal diffusivity of penta Bi- Pb- Sn based alloys

Samples	E GPa	$\mu$ GPa	B GPa	$Q^{-1}$	$D_{th} \times 10^{-8} \text{ m}^2/\text{sec}$
$Bi_{50}Pb_{15}Sn_{22}Cd_3In_{10}$	29.3	10.84	33.05	0.085	35.2
$Bi_{50}Pb_{15}Sn_{22}Zn_3In_{10}$	31.63	11.71	35.31	0.025	34.17
$Bi_{50}Pb_{15}Sn_{28}Cd_3In_4$	24.40	9.01	27.86	0.14	43.98
$Bi_{50}Pb_{15}Sn_{28}Zn_3In_4$	25.38	9.38	28.67	0.059	41.09

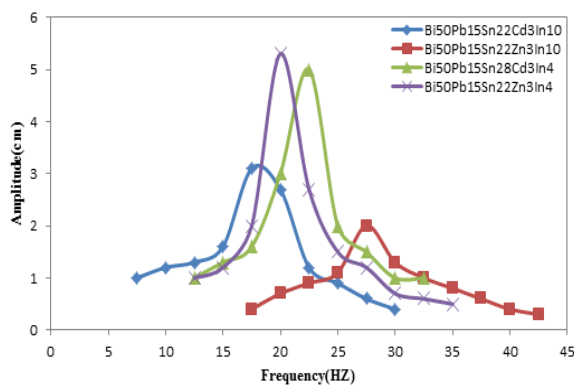


Figure 4:- resonance curves of penta Bi- Pb- Sn based alloys

### Vickers microhardness and minimum shear stress

The hardness is the property of material, which gives it the ability to resist being permanently deformed when a load is applied. Vickers hardness of  $Bi_{50}Pb_{15}Sn_{22}In_{10}X_3$  and  $Bi_{50}Pb_{15}Sn_{28}In_4X_3$  (X=Cd or Zn) alloys at 10 gram force and indentation time 5 sec are exposed in Table 5. The minimum shear stress ( $\tau_m$ ) of  $Bi_{50}Pb_{15}Sn_{22}In_{10}X_3$  and  $Bi_{50}Pb_{15}Sn_{28}In_4X_3$  (X=Cd or Zn) alloys was calculated and then listed in Table 5. Vickers hardness of Bi- Pb- Sn- In alloys depend on its compositions.

## 4. CONCLUSIONS

Microstructure (formed phases) of  $Bi_{50}Pb_{15}Sn_{22}In_{10}X_3$  and  $Bi_{50}Pb_{15}Sn_{28}In_4X_3$  (X=Cd or Zn) alloys depend on alloys compositions. Physical properties (thermal, electrical and mechanical) of Bi- Pb- Sn- In- X (X= Cd/ or Zn) alloys effected by alloys compositions. The new alloy,  $Bi_{50}Pb_{15}Sn_{22}Cd_3In_{10}$ , has better properties for shielding blocks in mega-volt radiotherapy.

## 5. REFERENCES

- [1] Kamal M, El-Bediwi A.B and Karman M.B, J. Mater. Sci.: Mater. Electro. 9 (1998) 425
- [2] Kamal M, Ewaida M. A, Elleithy M. A and Dawod T. A, Mans. Sci. Bull. C. Nat. Sci. and Phys. Sci 27: 1(2000)
- [3] Dawod T. A, M. SC. Thesis, Faculty of Science, Mansoura University, (2000)
- [4] Kamal M, Mazen S, El- Bediwi A. B and El- Naggar M, Radia. Eff. & Def. in Sol. 157 (2002) 467-474
- [5] Kamal M, El-Bediwi A. B, J. Mater. Sci.: Mater. Electro. 11 (2000) 519-523
- [6] Kamal M, Karman M. B and El-Bediwi A. B, U. Scientist Phyl. Sciences, 9: 2 (1997) 164
- [7] Mc Cormack M, Chen H. S, Kammalott G.W, Jin S. J. Electron. Mater. 26: 8 (1997) 954
- [8] Laine E, Lähteenmäki I, Lehtoranta I, J. Mater. Sci. 13 (1978) 108-112
- [9] Suryanara Yana C, Scripta Metall. 5 (1971) 337-40
- [10] Borromée-Gautier C, Giessen B. C and Grrant N. J, J. Chem. Phys. 48 (1968) 1905-11
- [11] Straumanis W and Brakss N; Z. Phys. Chem., 30B (1935) 17
- [12] Straumanis W and Brakss N;; Z. Phys. Chem. 38B (1937) 140
- [13] Kamal M, Mazen S, El-Bediwi A, Kashita E, Radia. Eff. & Def. in Sol. 161 (2006) 143-48
- [14] Chriastelova J, Ozvold M, J. of alloys and compounds 457 (2008) 323-328
- [15] Kamal M, Moharram B. M, Farag H, El-Bediwi A and Abosheiaasha H. F, Radia. Eff. & Def. in Sol. 161 (2006) 137- 142
- [16] Kamal M, Mazen S, El- Bediwi A. B, Kashita E, Radia. Eff. & Def. in Sol. 161 (2006) 143- 148
- [17] Kamal M, Moharram B. M, Farag H, El-Bediwi A and Abosheiaasha H. F, Radia. Eff. & Def. in Sol. 161 (2006) 421- 425
- [18] Kamal M, El-Bediwi A. B, Radia. Eff. & Def. Sol. 159: 11- 12 (2004) 651- 657
- [19] El-Bediwi A. B, A.M.S.E., 77: 4 (2004) Modelling A
- [20] El-Bediwi A.B, A.M.S.E., 75: 3 (2002) 1
- [21] Cullity B. D, "Element of x-ray diffraction" Ch.10 (1959) 297
- [22] Spinnert S and Teffit W. E, ASTM, Proc. 61 (1961) 1221
- [23] Schreiber E, Anderson O. L and Soga N, Elastic Constants and their Measurement, McGraw-Hill Book Company, Ch. 4 (1973)

# Influence of Titanium Oxide on Creep Behavior, Microstructure and Physical Properties of Tin-Antimony and Tin-Aluminum-Antimony Based Bearing Alloys

Abu Bakr El- Bediwi  
Metal Physics Lab., Physics  
Department, Faculty of Science,  
Mansoura University  
Mansoura, Egypt

Maison Hamid Grayb  
Ministry of education  
Iraq

Mustafa Kamal  
Metal Physics Lab., Physics  
Department, Faculty of Science,  
Mansoura University  
Mansoura, Egypt

**Abstract:** Influence of adding titanium oxide (TiO<sub>2</sub>) nanoparticles on creep behavior, structure, mechanical and thermal properties of tin-antimony-lead and tin-aluminum-antimony bearing alloys have been studied and analyzed. Stress exponent of tin- antimony- lead and tin-aluminum- antimony- lead alloys decreased after adding titanium oxide. Elastic modulus of tin- antimony- lead increased after adding titanium oxide. Internal friction of tin- antimony- lead and tin- aluminum- antimony- lead alloys varied after adding titanium oxide. Microstructure of tin-antimony- lead and tin- aluminum- antimony- lead alloys changed after adding titanium oxide. Strengths of tin- antimony- lead and tin- aluminum-antimony- lead alloys increased after adding titanium oxide. Thermal parameters of tin- antimony- lead and tin- aluminum- antimony- lead alloys varied after adding titanium oxide. The Sn<sub>79</sub>Sb<sub>15</sub>Pb<sub>5</sub>(TiO<sub>2</sub>)<sub>1</sub> alloy has better bearing properties such as lowest internal friction, high elastic modulus and higher thermal diffusivity for industrial applications

**Key words:** stress exponent, titanium oxide, bearing alloys, internal friction, creep indentation, thermal properties, mechanical properties

## 1. INTRODUCTION

Bearing is a device to allow constrained relative motion between two or more parts, typically rotation or linear movement. Bearing is a device used to transmit loads between relatively moving surfaces. The tribological properties of tin-based bearing alloys with different compositions, (7% and 20%), have been investigated [1]. Structure, electrical resistivity and elastic modulus of SnSb<sub>7</sub>X (X = 0, Cu, Ag, or Cu and Ag) and Pb<sub>63-x</sub>Sn<sub>30</sub>Sb<sub>7</sub>Cu<sub>x</sub> [x=0 or x≤2.5] alloys have been studied and analyzed [2, 3]. Electrical resistivity, elastic modulus and internal friction of Pb<sub>63</sub>Sn<sub>30</sub>Sb<sub>7</sub> decreases after adding Cu. Mechanical properties of Sn-Sb bearing alloy have been evaluated [4]. Mechanical properties of Sn-Sb improved after adding 1 wt. % of Cu or Ag. Also the elastic modulus, internal friction and stiffness of Sn-Sb based bearing alloys varied after annealing for 2 and 4 h at 120, 140 and 160 °C. Creep behavior of SnSb<sub>5</sub> alloy and SnPb<sub>40</sub>Sb<sub>2.5</sub> peritectic alloy were studied by long time Vickers indentation testing at room temperature [5- 7]. Increasing Sb content from 7.5% to 20% provided an increase in hardness. Tensile properties of SnSb<sub>5</sub>Bi<sub>1.5</sub> and SnSb<sub>5</sub>Cu<sub>1.5</sub> alloys have been studied at different strain rates ranging from 5×10<sup>-4</sup> to 1×10<sup>-2</sup> s<sup>-1</sup> over the wide temperature range of 298-400 K [8]. Strength and ductility of SnSb<sub>5</sub> improved after adding Bi and Cu. Creep behavior, elastic modulus and internal friction of SnSb<sub>10</sub>Cu<sub>2</sub>X<sub>2</sub> (X = Pb, Ag, Se, Cd and Zn) alloys have been investigated and stress exponents have been determined [9]. The effect of solidification rate, heating and micro additions on microstructure and hardness of tin-based white metals have been studied [10, 11]. Rapid cooling suppresses formation and growth of SbSn cuboids and increases hardness. Structure, hardness, mechanical and electrical transport properties of Sn<sub>90-x</sub>Sb<sub>10</sub>Bi<sub>x</sub> (x = 0, or x ≥1) alloys have been studied and analyzed [12]. Electrical resistivity and hardness of SnSb<sub>10</sub> increased after adding bismuth content. Internal friction, elastic modulus and thermal diffusivity of SnSb<sub>10</sub> decreased after adding bismuth content. The effects of small amounts of Ag and Cu on the as-cast microstructure and creep properties of the SnSb<sub>5</sub>

alloy have been investigated [13]. Small additions of Ag and Cu elements could effectively change the creep behavior of the SnSb<sub>5</sub> alloy. The friction coefficients of

SnSb<sub>20.2</sub>Pb<sub>16.6</sub>Cu<sub>2.6</sub> is lower than that of SnSb<sub>7.2</sub>Pb<sub>0.4</sub>Cu<sub>3</sub> under all scratch test conditions [14]. The directionally solidified microstructure of SnSb<sub>16</sub> hyperperitectic alloy has been investigated at various solidification rates using a high-thermal gradient directional solidification apparatus [15]. The volume fraction of the SnSb phase firstly decreased and then increased when the solidification rate increased. The aim of this work was to study and analyze the effects of adding titanium oxide nanoparticles on creep behavior, structure, mechanical and thermal properties of tin-antimony-lead and tin-aluminum-antimony based alloys.

## 2. EXPERIMENTAL WORK

Two groups of alloys, Sn<sub>80-x</sub>Sb<sub>15</sub>Pb<sub>5</sub>(TiO<sub>2</sub>)<sub>x</sub> (x= 0.5, 1 and 1.5 wt.%) and Sn<sub>60-x</sub>Al<sub>20</sub>Sb<sub>15</sub>Pb<sub>5</sub>(TiO<sub>2</sub>)<sub>x</sub> (x= 0.5, 1 and 1.5 wt.%), were molten in the muffle furnace. Using elements tin, antimony, lead, aluminum and titanium oxide have a high purity, more than 99.95%. The resulting ingots were turned and re-melted several times to increase the homogeneity of the ingots. From these ingots, long ribbons of about 3-5 mm width and ~ 70 μm thickness were prepared as the test samples by directing a stream of molten alloy onto the outer surface of rapidly revolving copper roller with surface velocity 31 m/s giving a cooling rate of 3.7 × 10<sup>5</sup> K/s. The samples then cut into convenient shape for the measurements using double knife cutter. Structure of used alloys was performed using an Shimadzu x-ray diffractometer (DX-30, Japan) of Cu-Kα radiation with λ=1.54056 Å at 45 kV and 35 mA and Ni-filter in the angular range 2θ ranging from 0 to 100° in continuous mode with a scan speed 5 deg/min. Scanning electron microscope JEOL JSM-6510LV, Japan was used to study microstructure of used samples. The melting endotherms of used alloys were obtained using a SDT Q600 V20.9 Build 20 instrument.

A digital Vickers micro-hardness tester, (Model-FM-7- Japan), was used to measure Vickers hardness values of used alloys. Internal friction  $Q^{-1}$  and the elastic constants of used alloys were determined using the dynamic resonance method [16-18].

### 3. RESULTS AND DISCUSSIONS

#### Structure

X-ray diffraction patterns of  $\text{Sn}_{80-x}\text{Sb}_{15}\text{Pb}_5(\text{TiO}_2)_x$  ( $x=0.5, 1$  and  $1.5$  wt.%) rapidly solidified alloys have lines corresponding to  $\beta$ -Sn, Pb, Sb and SbSn intermetallic phases as shown in Figure 1. X-ray analysis of  $\text{Sn}_{80}\text{Sb}_{15}\text{Pb}_5$  show that, formed phases (intensity, peak broadness, miller indices, position ( $2\theta$ ), and area under peaks) changed after adding of  $(\text{TiO}_2)_x$ . That is because  $\text{TiO}_2$  disappeared, dissolved in the matrix of alloy. Also crystal particle size of  $\beta$ -Sn in  $\text{Sn}_{80}\text{Sb}_{15}\text{Pb}_5$  alloy increased after adding  $\text{TiO}_2$  as seen in Table 1.

Table 1:- crystal particle size of  $\beta$ -Sn in  $\text{Sn}_{80-x}\text{Sb}_{10}\text{Pb}_5(\text{TiO}_2)_x$  alloys

Samples	Particle size $\text{\AA}$
$\text{Sn}_{80}\text{Sb}_{15}\text{Pb}_5$	317.25
$\text{Sn}_{79.5}\text{Sb}_{15}\text{Pb}_5(\text{TiO}_2)_{0.5}$	395.12
$\text{Sn}_{79}\text{Sb}_{15}\text{Pb}_5(\text{TiO}_2)_1$	448.06
$\text{Sn}_{78.5}\text{Sb}_{15}\text{Pb}_5(\text{TiO}_2)_{1.5}$	415.38

Scanning electron micrographs, SEM, of  $\text{Sn}_{80-x}\text{Sb}_{15}\text{Pb}_5(\text{TiO}_2)_x$  alloys show heterogeneous structure as shown in Figure 2 and that agreed with x-ray analysis. Adding  $\text{TiO}_2$  caused change in microstructure of  $\text{Sn}_{80}\text{Sb}_{15}\text{Pb}_5$  alloy.

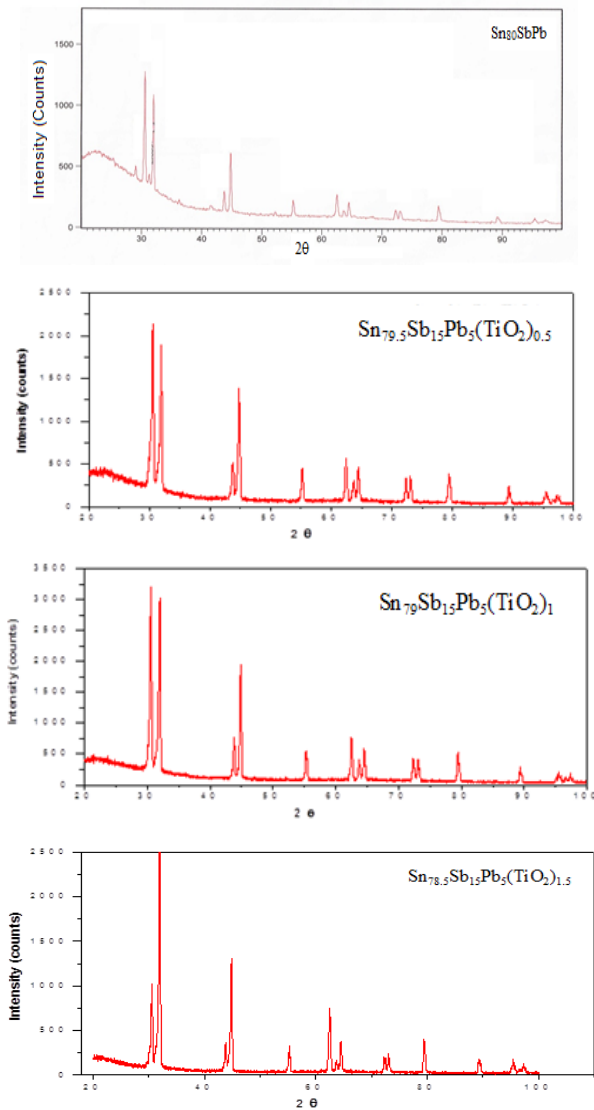


Figure 1:- x-ray diffraction patterns of  $\text{Sn}_{80-x}\text{Sb}_{10}\text{Pb}_5(\text{TiO}_2)_x$  alloys

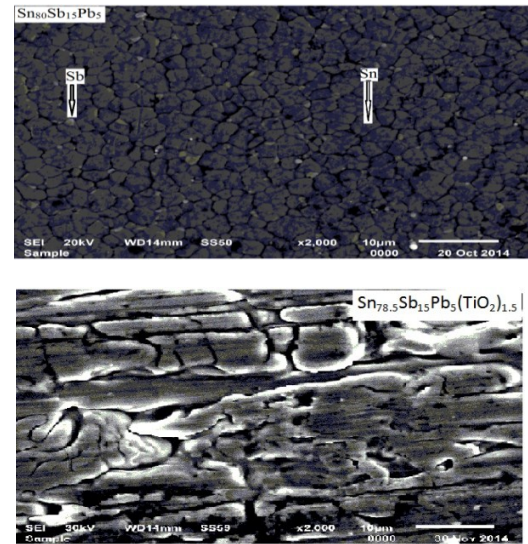
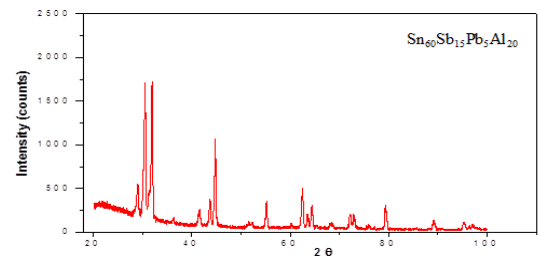


Figure 2:- SEM of  $\text{Sn}_{80-x}\text{Sb}_{10}\text{Pb}_5(\text{TiO}_2)_x$  alloys

X-ray diffraction patterns of  $\text{Sn}_{60-x}\text{Al}_{20}\text{Sb}_{15}\text{Pb}_5(\text{TiO}_2)_x$  ( $x=0.5, 1$  and  $1.5$  wt.%) rapidly solidified alloys have lines corresponding to  $\beta$ -Sn, Pb, Sb and SbSn intermetallic phases as shown in Figure 3. X-ray analysis of  $\text{Sn}_{60}\text{Al}_{20}\text{Sb}_{15}\text{Pb}_5$  show that, formed phases (intensity, peak broadness, miller indices, position ( $2\theta$ ), and area under peaks) changed after adding of  $(\text{TiO}_2)_x$ . That is because Al and  $\text{TiO}_2$  disappeared\ or not detected, dissolved in the matrix of alloy. Also crystal particle size of  $\beta$ -Sn in  $\text{Sn}_{60}\text{Al}_{20}\text{Sb}_{15}\text{Pb}_5$  alloy increased after adding  $\text{TiO}_2$  as seen in Table 2.



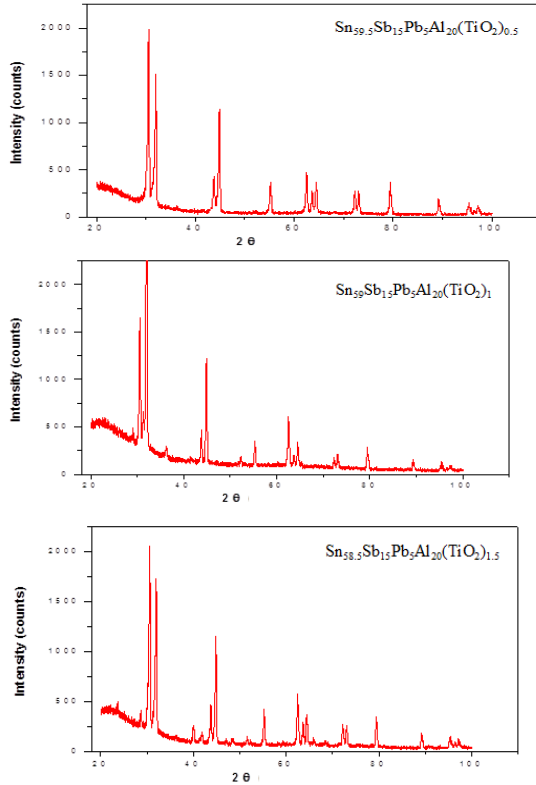


Figure 3:- x-ray diffraction patterns of  $\text{Sn}_{60-x}\text{Al}_{20}\text{Sb}_{15}\text{Pb}_5(\text{TiO}_2)_x$  alloys

Table 2:- crystal particle size of  $\beta$ - Sn in  $\text{Sn}_{60-x}\text{Al}_{20}\text{Sb}_{15}\text{Pb}_5(\text{TiO}_2)_x$  alloys

Samples	Particle size Å
$\text{Sn}_{60}\text{Al}_{20}\text{Sb}_{15}\text{Pb}_5$	337.70
$\text{Sn}_{59.5}\text{Al}_{20}\text{Sb}_{15}\text{Pb}_5(\text{TiO}_2)_{0.5}$	412.47
$\text{Sn}_{59}\text{Al}_{20}\text{Sb}_{15}\text{Pb}_5(\text{TiO}_2)_1$	409.78
$\text{Sn}_{58.5}\text{Al}_{20}\text{Sb}_{15}\text{Pb}_5(\text{TiO}_2)_{1.5}$	368.36

Scanning electron micrographs, SEM, of  $\text{Sn}_{60-x}\text{Al}_{20}\text{Sb}_{15}\text{Pb}_5(\text{TiO}_2)_x$  alloys show heterogeneous structure as shown in Figure 4 and that agreed with x-ray analysis.

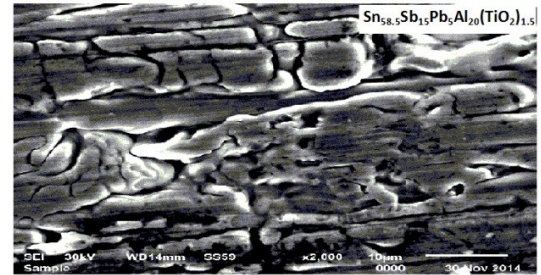
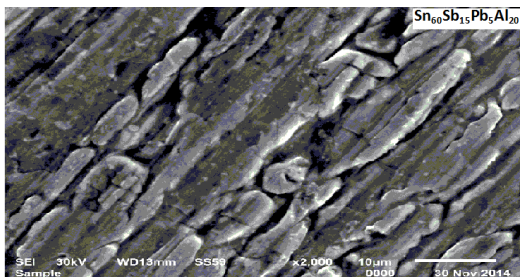


Figure 4:- SEM of  $\text{Sn}_{60-x}\text{Al}_{20}\text{Sb}_{15}\text{Pb}_5(\text{TiO}_2)_x$  alloys

### Mechanical properties

The elastic constants are directly related to atomic bonding and structure. Elastic moduli of  $\text{Sn}_{80-x}\text{Sb}_{10}\text{Pb}_5(\text{TiO}_2)_x$  alloys are listed in Table 3. Elastic modulus of  $\text{Sn}_{80}\text{Sb}_{10}\text{Pb}_5$  alloy increased after adding  $\text{TiO}_2$  nanoparticles.

The resonance curves of  $\text{Sn}_{80-x}\text{Sb}_{10}\text{Pb}_5(\text{TiO}_2)_x$  alloys are shown in Figure 5. Calculated internal friction and thermal diffusivity of  $\text{Sn}_{80-x}\text{Sb}_{10}\text{Pb}_5(\text{TiO}_2)_x$  alloys are listed in Table 3. Internal friction of  $\text{Sn}_{87}\text{Sb}_{10}\text{Pb}_3$  alloy varied after adding  $\text{TiO}_2$  nanoparticles. The  $\text{Sn}_{79}\text{Sb}_{15}\text{Pb}_5(\text{TiO}_2)_1$  alloy has better bearing properties such as lowest internal friction, high elastic modulus and higher thermal diffusivity for industrial applications.

Table 3:- elastic moduli, internal friction and thermal diffusivity of  $\text{Sn}_{80-x}\text{Sb}_{10}\text{Pb}_5(\text{TiO}_2)_x$  alloys

Samples	E GPa	$\mu$ GPa	B GPa	$Q^{-1}$	$D_{th} \times 10^{-8} \text{ m}^2/\text{sec}$
$\text{Sn}_{80}\text{Sb}_{10}\text{Pb}_5$	24.28	8.93	28.80	0.034	21.12
$\text{Sn}_{79.5}\text{Sb}_{10}\text{Pb}_5(\text{TiO}_2)_{0.5}$	32.96	12.18	37.49	0.036	17.7
$\text{Sn}_{79}\text{Sb}_{10}\text{Pb}_5(\text{TiO}_2)_1$	38.25	14.08	45.09	0.029	34.5
$\text{Sn}_{78.5}\text{Sb}_{10}\text{Pb}_5(\text{TiO}_2)_{1.5}$	42.67	15.71	50.12	0.041	12.3

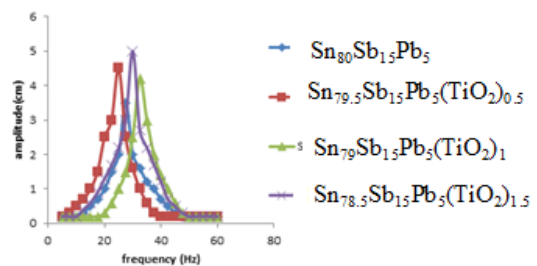


Figure 5:- resonance curves of  $\text{Sn}_{80-x}\text{Sb}_{10}\text{Pb}_5(\text{TiO}_2)_x$  alloys

Elastic moduli of  $\text{Sn}_{60-x}\text{Al}_{20}\text{Sb}_{15}\text{Pb}_5(\text{TiO}_2)_x$  alloys are listed in Table 4. Elastic modulus of  $\text{Sn}_{60}\text{Al}_{20}\text{Sb}_{15}\text{Pb}_5$  alloy varied after adding  $\text{TiO}_2$  nanoparticles.

The resonance curves of  $\text{Sn}_{60-x}\text{Al}_{20}\text{Sb}_{15}\text{Pb}_5(\text{TiO}_2)_x$  alloys are shown in Figure 6. Calculated internal friction and thermal diffusivity of  $\text{Sn}_{60-x}\text{Al}_{20}\text{Sb}_{15}\text{Pb}_5(\text{TiO}_2)_x$  alloys are listed in Table 4. Internal friction of  $\text{Sn}_{60}\text{Al}_{20}\text{Sb}_{15}\text{Pb}_5$  alloy varied after adding  $\text{TiO}_2$  nanoparticles.

The Sn<sub>59</sub> Al<sub>20</sub>Sb<sub>15</sub>Pb<sub>5</sub>(TiO<sub>2</sub>)<sub>1</sub> alloy has better bearing properties such as adequate internal friction, high elastic modulus and higher thermal diffusivity for industrial applications.

Table 4:- elastic moduli, internal friction and thermal diffusivity of Sn<sub>60-x</sub>Al<sub>20</sub>Sb<sub>15</sub>Pb<sub>5</sub>(TiO<sub>2</sub>)<sub>x</sub> alloys

Samples	E GPa	μ GPa	B GPa	Q <sup>-1</sup>	D <sub>th</sub> × 10 <sup>-8</sup> m <sup>2</sup> /sec
Sn <sub>60</sub> Al <sub>20</sub> Sb <sub>15</sub> Pb <sub>5</sub>	38.95	14.35	45.56	0.031	12.1
Sn <sub>59.5</sub> Al <sub>20</sub> Sb <sub>15</sub> Pb <sub>5</sub> (TiO <sub>2</sub> ) <sub>0.5</sub>	36.99	13.63	43.11	0.033	16
Sn <sub>59</sub> Al <sub>20</sub> Sb <sub>15</sub> Pb <sub>5</sub> (TiO <sub>2</sub> ) <sub>1</sub>	42.22	15.56	49.07	0.036	18.5
Sn <sub>58.5</sub> Al <sub>20</sub> Sb <sub>15</sub> Pb <sub>5</sub> (TiO <sub>2</sub> ) <sub>1.5</sub>	37.55	13.85	43.49	0.030	13.6

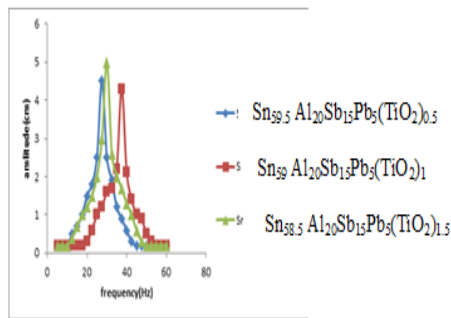


Figure 6:- resonance curves of Sn<sub>60-x</sub>Al<sub>20</sub>Sb<sub>15</sub>Pb<sub>5</sub>(TiO<sub>2</sub>)<sub>x</sub> alloys

### Thermal properties

Thermal analysis is often used to study solid state transformations as well as solid-liquid reactions. Figure 7 shows DSC thermographs for Sn<sub>80-x</sub>Sb<sub>10</sub>Pb<sub>5</sub>(TiO<sub>2</sub>)<sub>x</sub> alloys. Variation occurred in exothermal peak of Sn<sub>80</sub>Sb<sub>10</sub>Pb<sub>5</sub> alloy. The melting temperature and other thermal properties of Sn<sub>80-x</sub>Sb<sub>10</sub>Pb<sub>5</sub>(TiO<sub>2</sub>)<sub>x</sub> alloys are listed in Table 5. Melting temperature of Sn<sub>80</sub>Sb<sub>10</sub>Pb<sub>5</sub> alloy decreased after adding TiO<sub>2</sub> nanoparticles.

Specific heat, enthalpy and thermal conductivity of Sn<sub>80</sub>Sb<sub>10</sub>Pb<sub>5</sub> alloy varied after adding TiO<sub>2</sub> nanoparticles. That is because TiO<sub>2</sub> nanoparticles due change in matrix microstructure of Sn<sub>80</sub>Sb<sub>10</sub>Pb<sub>5</sub> alloy.

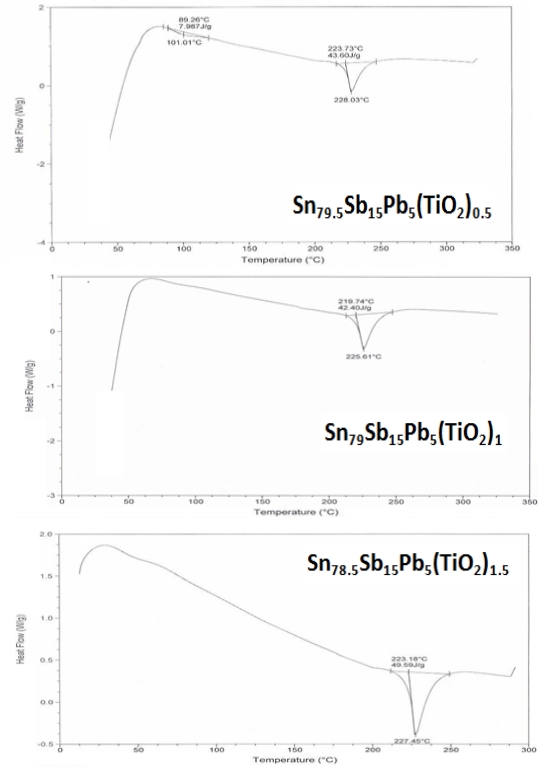
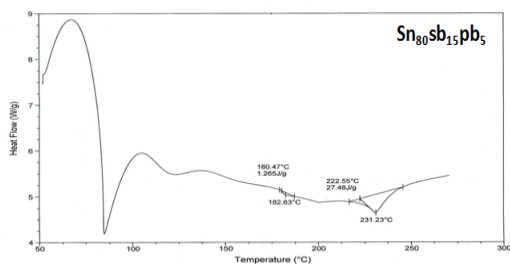


Figure 7:- DSC of Sn<sub>87-x</sub>Sb<sub>10</sub>Pb<sub>5</sub>(TiO<sub>2</sub>)<sub>x</sub> alloys

Table 5:- melting point and other thermal properties of Sn<sub>80-x</sub>Sb<sub>10</sub>Pb<sub>5</sub>(TiO<sub>2</sub>)<sub>x</sub> alloys

Samples	Melting point °C	C <sub>p</sub> J/g. °C	Δ S J/g. °C	K W.m <sup>-1</sup> .K <sup>-1</sup>
Sn <sub>80</sub> Sb <sub>15</sub> Pb <sub>5</sub>	231.23	0.12	1.57	1.65
Sn <sub>79.5</sub> Sb <sub>15</sub> Pb <sub>5</sub> (TiO <sub>2</sub> ) <sub>0.5</sub>	228.03	3.41	0.189	1.86
Sn <sub>79</sub> Sb <sub>15</sub> Pb <sub>5</sub> (TiO <sub>2</sub> ) <sub>1</sub>	225.61	2.53	0.185	1.46
Sn <sub>78.5</sub> Sb <sub>15</sub> Pb <sub>5</sub> (TiO <sub>2</sub> ) <sub>1.5</sub>	227.45	3.35	0.215	2.77

Figure 8 shows DSC thermographs for Sn<sub>60-x</sub>Al<sub>20</sub>Sb<sub>15</sub>Pb<sub>5</sub>(TiO<sub>2</sub>)<sub>x</sub> alloys. Variation occurred in exothermal peak of Sn<sub>60</sub> Al<sub>20</sub>Sb<sub>15</sub>Pb<sub>5</sub> alloy. The melting temperature and other thermal properties of Sn<sub>60-x</sub>Al<sub>20</sub>Sb<sub>15</sub>Pb<sub>5</sub>(TiO<sub>2</sub>)<sub>x</sub> alloys are listed in Table 7. Melting temperature of Sn<sub>60</sub> Al<sub>20</sub>Sb<sub>15</sub>Pb<sub>5</sub> alloy varied after adding TiO<sub>2</sub> nanoparticles.

Specific heat, enthalpy and thermal conductivity of Sn<sub>60</sub>Sb<sub>10</sub>Pb<sub>5</sub> alloy varied after adding TiO<sub>2</sub> nanoparticles. That is because TiO<sub>2</sub> nanoparticles due change in matrix microstructure of Sn<sub>60</sub> Al<sub>20</sub>Sb<sub>15</sub>Pb<sub>5</sub> alloy.

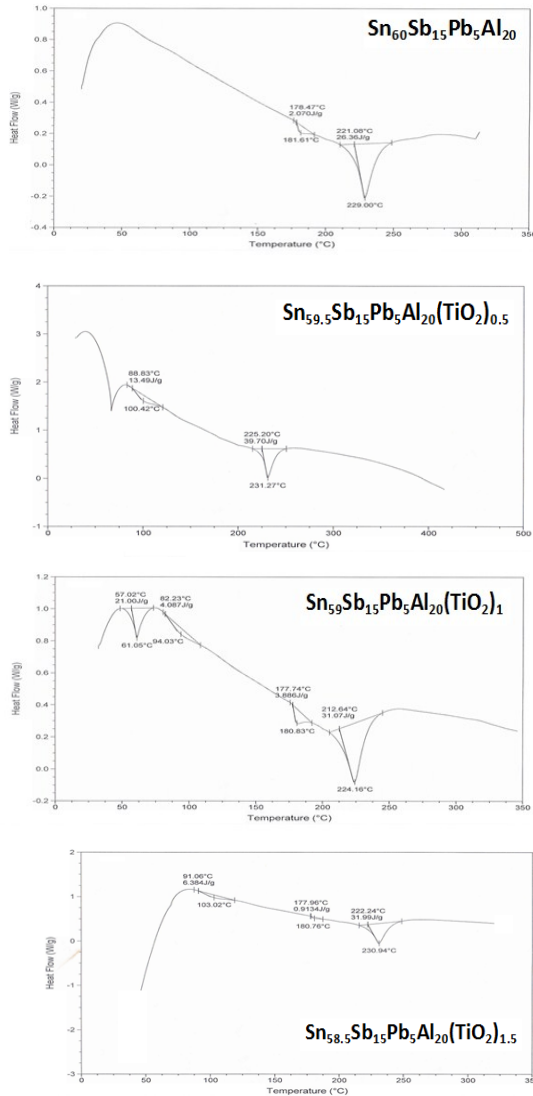


Figure 8:- DSC of  $\text{Sn}_{60-x}\text{Al}_{20}\text{Sb}_{15}\text{Pb}_5(\text{TiO}_2)_x$  alloys

Table 6:- melting point and other thermal properties of  $\text{Sn}_{60-x}\text{Al}_{20}\text{Sb}_{15}\text{Pb}_5(\text{TiO}_2)_x$  alloys

Samples	Melting point °C	$C_p$ J/g. °C	$\Delta S$ J/g. °C	K $\text{W.m}^{-1}.\text{K}^{-1}$
$\text{Sn}_{60}\text{Al}_{20}\text{Sb}_{15}\text{Pb}_5$	229	1.6	0.11	2.08
$\text{Sn}_{59.5}\text{Al}_{20}\text{Sb}_{15}\text{Pb}_5(\text{TiO}_2)_{0.5}$	231.27	2.46	0.18	2.28
$\text{Sn}_{59}\text{Al}_{20}\text{Sb}_{15}\text{Pb}_5(\text{TiO}_2)_1$	224.16	1.48	0.14	2.03
$\text{Sn}_{58.5}\text{Al}_{20}\text{Sb}_{15}\text{Pb}_5(\text{TiO}_2)_{1.5}$	230.94	1.97	0.14	1.62

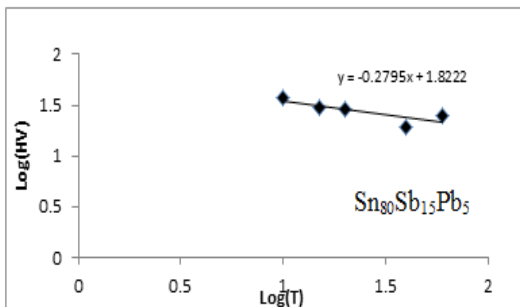
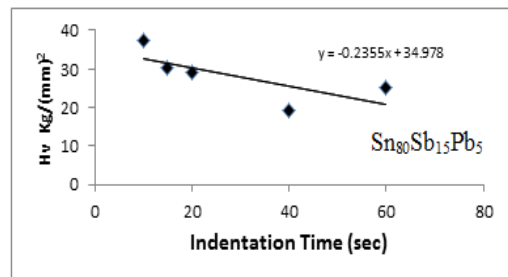
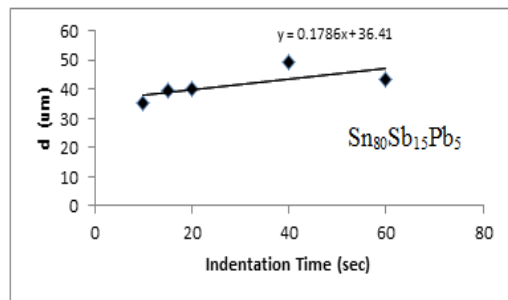
### Creep behavior

Creep behavior of  $\text{Sn}_{80-x}\text{Sb}_{10}\text{Pb}_5(\text{TiO}_2)_x$  and  $\text{Sn}_{60-x}\text{Al}_{20}\text{Sb}_{15}\text{Pb}_5(\text{TiO}_2)_x$  alloys were investigated by indentation method

(Vickers hardness test) performed at room temperature. The indentation creep data are shown in Figure 9, where the indentation length is plotted against the indentation time applying constant load of 10 g. The indentation length increases with the indentation time. In the Mulheam-Tabor method, Figure 9, Vickers hardness number of  $\text{Sn}_{80-x}\text{Sb}_{10}\text{Pb}_5(\text{TiO}_2)_x$  and  $\text{Sn}_{60-x}\text{Al}_{20}\text{Sb}_{15}\text{Pb}_5(\text{TiO}_2)_x$  alloys are plotted versus indentation time on log-log scale for the indentation data. It is observed that there exists a linear relationship between indentation time and hardness for all conditions. The slope of the resultant lines

according Mulheam-Tabor method is  $-\left(n + \frac{1}{2}\right)$  where n is the

stress exponent. The stress exponent values of  $\text{Sn}_{80-x}\text{Sb}_{10}\text{Pb}_5(\text{TiO}_2)_x$  and  $\text{Sn}_{60-x}\text{Al}_{20}\text{Sb}_{15}\text{Pb}_5(\text{TiO}_2)_x$  alloys are given in Table 7. These exponent values are in the range of 2.16 to 5.75 depending on the composition of used alloy and that agreed with the pervious results ( $n=4.5$  [19] and  $n \sim 5.3$  to 5.6 and 5.8 to 5.9 [20]). The change in stress exponent values are attributable to microstructural features (changing in  $\beta$  matrix such as change in the lattice parameters, solid solution, size and distribution of strengthening phases, intermetallic phases) and that is agree with the pervious results [21].



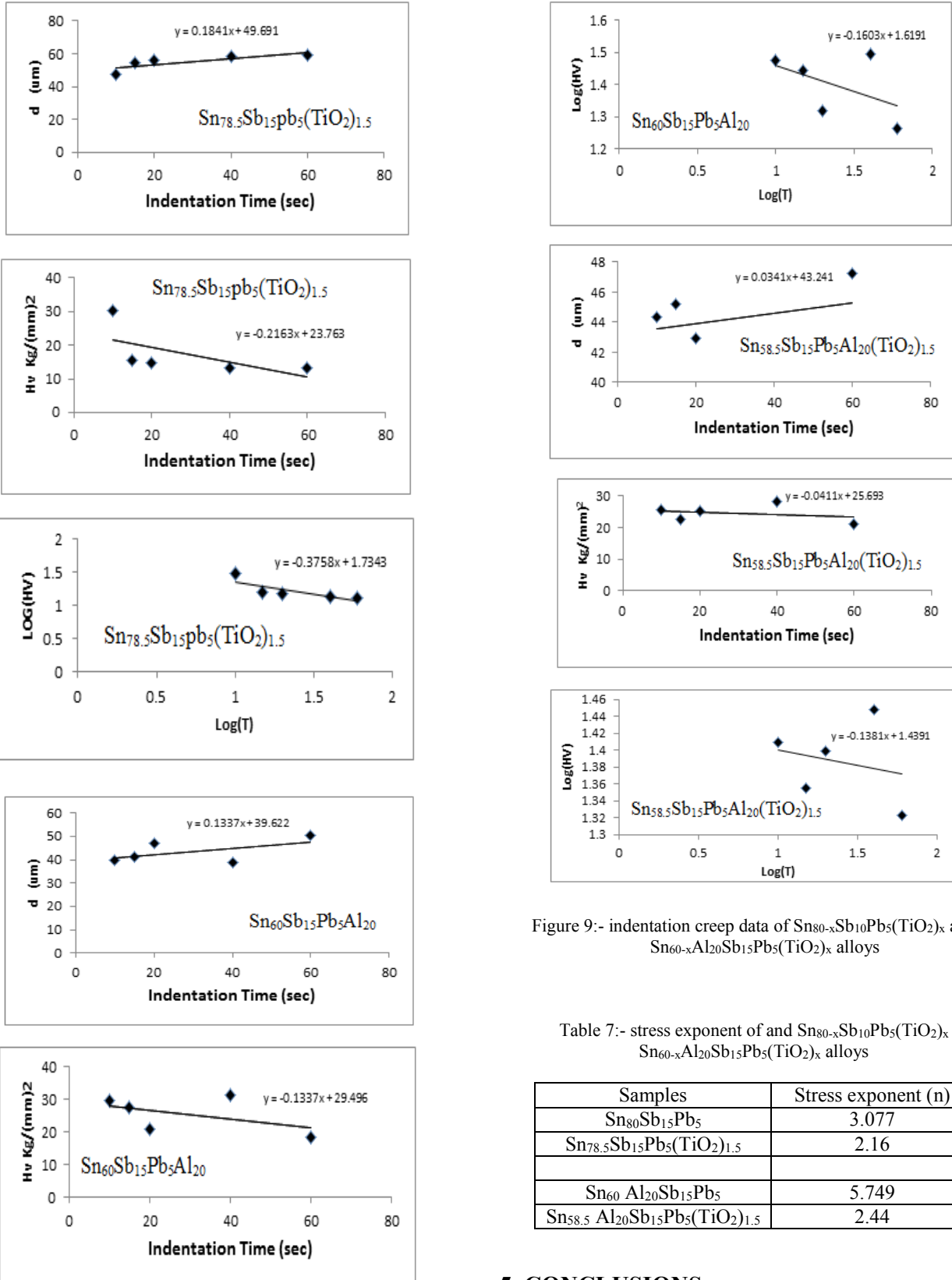


Figure 9:- indentation creep data of  $\text{Sn}_{80-x}\text{Sb}_{10}\text{Pb}_5(\text{TiO}_2)_x$  and  $\text{Sn}_{60-x}\text{Al}_{20}\text{Sb}_{15}\text{Pb}_5(\text{TiO}_2)_x$  alloys

Table 7:- stress exponent of and  $\text{Sn}_{80-x}\text{Sb}_{10}\text{Pb}_5(\text{TiO}_2)_x$   $\text{Sn}_{60-x}\text{Al}_{20}\text{Sb}_{15}\text{Pb}_5(\text{TiO}_2)_x$  alloys

Samples	Stress exponent (n)
$\text{Sn}_{80}\text{Sb}_{15}\text{Pb}_5$	3.077
$\text{Sn}_{78.5}\text{Sb}_{15}\text{Pb}_5(\text{TiO}_2)_{1.5}$	2.16
$\text{Sn}_{60} \text{Al}_{20}\text{Sb}_{15}\text{Pb}_5$	5.749
$\text{Sn}_{58.5} \text{Al}_{20}\text{Sb}_{15}\text{Pb}_5(\text{TiO}_2)_{1.5}$	2.44

## 5. CONCLUSIONS

Microstructure of tin- antimony- lead and tin- aluminum-antimony- lead alloys changed after adding titanium oxide. Stress exponent of tin- antimony- lead and tin- aluminum- antimony- lead alloys decreased after adding titanium oxide. Strengths of tin-antimony- lead and tin- aluminum- antimony- lead alloys increased after adding titanium oxide. Internal friction and thermal parameters of tin- antimony- lead and tin- aluminum- antimony- lead alloys varied after adding titanium oxide. The  $\text{Sn}_{79}\text{Sb}_{15}\text{Pb}_5(\text{TiO}_2)_1$  and  $\text{Sn}_{59}\text{Al}_{20}\text{Sb}_{15}\text{Pb}_5(\text{TiO}_2)_1$  alloys have better bearing properties for industrial applications

## 6. REFERENCES

- [1] Zeren A, Feyzullahoglu E, Zeren M, Mater. and Design 28 (2007) 318
- [2] El-Bediwi A, Radiation Effects & Defects in Solids 159 (2004) 125
- [3] El- Bediwi A, Cryst. Res. Technol 40: 7 (2005) 688
- [4] El-Bediwi A, Radiation Effects & Defects in Solids 159 (2004) 539
- [5] Mahmudi R, J. Mater. Sci. 40 (2005) 3361
- [6] Mahmudi R and Rezaee-Bazzaz A, Mater. Lett. 59: 13 (2005) 1705
- [7] Mahmudi R, Geranmay A.R, Bakher M, Allam M, Mater. Sci. and Eng. A 457 (2007) 173
- [8] Esfandyarpour M.J, Mahmudi R, Mater. Sci. and Eng. A 530 (2011) 402
- [9] El-Bediwi A, Lashin A.R, Mossa M, Kamal M, Mater. Sci. and Eng. A 528 (2011) 3568
- [10] Goudarzi M.M, Jahromi S.A.J, Nazarboland A, Mater. and Design 30 (2009) 2283
- [11] Kamal M, Abdel-Salam A, Pieri J.C, J. Mater. Sci 19 (1984) 3880
- [12] El- Bediwi A.B, El Said Gouda, Kamal M, AMSE, 65, n° 1, Modeling C- 2004
- [13] El-Daly A.A, Mohamad A.Z, Fawzy A, El-TaHER A.M, Mater. Sci. and Eng. A 528 (2011) 1055
- [14] Bora M.O, Coban O, Sinmazcelik T, Gunay V, Zeren M, Mater. and Design 31 (2010) 2707
- [15] Xiaowu H, Shuangming L, Lin L, Hengzhi F, The Chinese Journal of Nonferrous Metals 14:1 (2004) 93
- [16] Schreiber E, Anderson O. L and Soga N, Elastic constant and their measurements, McGraw-Hill, New York, (1973) 82
- [17] Timoshenko S and Goddier J.N, "Theory of elasticity, 2<sup>nd</sup> Ed", McGraw-Hill, New York, (1951) 277
- [18] Nuttall K, J. Inst. Met. 99 (1971) 266
- [19] Geranmayeh A. R, Mahmudi R, J Matter Sci. 40 (2005) 3361
- [20] Kangoie M, Mahmudi R and Geranmayeh A. R., J Electr. Matter. 39 (2010) 215
- [21] Deraki Rani S, Murthy G. S, Mate. Sci. Techn., 403 (2004) 20





# Automatic Technique for Measuring The Electro-Mechanical Characteristics Of Quantum Tunneling Composites (QTC)

M.M. El-Tonsy	H.A. Shaaban	O.M.Al-Aqbi	R.M. Felfel
Physics Department, Faculty of Science Mansoura University Mansoura, Egypt	Physics Department, Faculty of Science Mansoura University Mansoura, Egypt	Ministry of education Baghdad-Iraq	Ministry of education Misrata - Libya

**Abstract:** Electrically conductive composites consisted of conducting fillers and the insulating polymer matrix. These composites could serve in preparation of piezoresistive composites (i.e. quantum tunnelling composites (QTC) due to their flexibility, light weight, easy processing, low cost, greater resistance changes, and ease of spreading over arbitrary curved surfaces. QTC have attracted tremendous attention due to their potential applications in advanced stress and strain sensors. Recently, various types of conducting materials and many soft polymers have been utilized in the manufacture of QTCs. Characterization of such composites involves several physical parameters. Therefore, a low cost technique was designed and manufactures in order to measure most of electro-mechanical properties of the produced composites with good accuracy and repeatability. QTCs were prepared by mixing poly-dimethyl siloxane (PDMS) and with different concentrations of graphite flakes (1:0.75, 1:1, 1:1.5, 1:1.75 and 1:2). This study declared the efficiency of the suggested technique as well as some fundamental features of the prepared composite. For example, conductivity of the composites containing higher concentration of graphite was found to be independent on rate of pressing during the test. It was also found that the capacitive behavior of the sample interrupted the flow of current at the instant of removing the applied pressure. The suggested setup has several advantages such as simplicity, high accuracy and providing lots of technical data that required for development and confirmation of models for the quantum tunnelling process.

---

**Keywords:** QTC, electro-mechanical, piezo-resistance, polymer/graphite composite, compressive capacitance, pressure sensors

---

## 1. INTRODUCTION

Traditional electro-conductive rubber is typically produced with vulcanized rubber filled with a high percentage of carbon black. Conductive particles of carbon, metals, carbon fibres, graphite, pyrolytic carbons and carbon black (with different purity and morphology) have been used as fillers in polymeric composites since the 50s [1]. Mechanism of electrical conduction in traditional polymeric composites is based on percolation. There is a critical threshold for the filler at which the sample suddenly becomes an excellent conductor as a result of formation of at the least one whole conductive path ensuring charge transport through the metallic particles. Beyond this threshold, the sample conductivity increases further since new paths formed by adding more metal filler until the saturation was obtained.

The conductivity of electro-conductive percolation-based composites commonly changes with any mechanical interactions. For instance, number of touching filler particles increases by applying compression pressure and consequently the number of conductive paths increases because of a higher relative concentration ratio.

The Quantum Tunnelling Composites (QTC) show similar behaviour to traditional metallic filled polymer composites, but

conduction mechanism at the nano-scale is different. The conduction mechanism within QTC is based on quantum effects which makes them particularly suitable for specific applications. Two factors controlling the conductivity of the QTC;

- The presence of spiked metallic particles where the electrostatic fields strengthen and become able to conduct to another metal particle,
- The extreme wet ability (i.e. adhesion) between the metal particles and the polymeric matrix.

Within QTC, the conducting nano-particles will not touch even when the inter-particle distances diminished under compression. Therefore, classical conduction via percolation does not be valid. However, the charge transfer between the particles would be occurred through tunnelling at the spikes due to the decreased distances and extreme voltages.

QTC has extremely large and reversible changes in the electrical conductivity when twisted, bent, stretched, or compressed. This advantage would facilitate use of QTC in

development of very simple and highly effective sensing systems such as tactile sensors [2,3].

It is easy to predict the great efforts in future for studying, developing and producing more advanced QTC. Hence, the current work presents an automatic tool for direct dynamic measurement of some important physical quantities for QTC such as;

- a) sample current as function of applied ascending and descending pressure,
- b) sample resistance against applied pressure,
- c) sample current and sample resistance as function of the pressing rate,
- d) effect of viscoelastic relaxation properties of the host polymer matrix on the decay of sample resistance ,
- e) effect of curing period and temperature on sample conductivity at certain mechanical deformation,
- f) influence of composition (matrix/filler ratio) on the conductivity of composites,
- g) effect of sample thickness on the current and resistance at specific mechanical deformation,
- h) impact of multi-component composite (i.e. contains several conductive fillers) on the sample conductivity at mechanical deformation,
- i) influence of geometry of metallic particles on the conductivity against mechanical deformation.

Furthermore, many other physical parameters can be measured with reasonable accuracy and in short time. The suggested measuring setup could be easily modified by adding more options for wider ranges of measurements such as temperature and external magnetic field (Hall Effect) effects.

## 2. SET UP OF THE SUGGESTED INSTRUMENT

Figure 1 shows construction of the instrument.

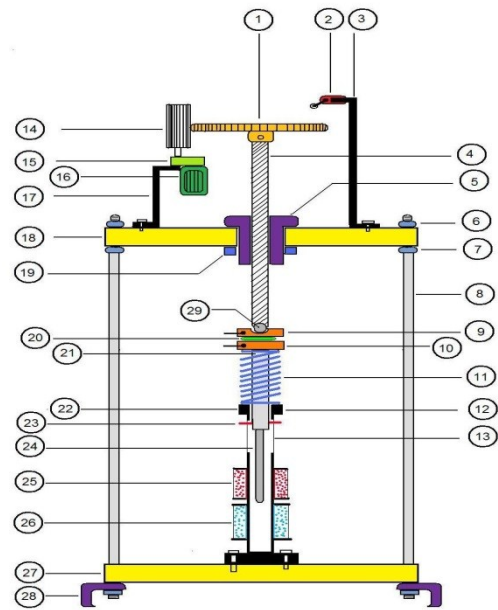


Figure 1: Schematic diagram of the measuring tool for characterising the physical properties of quantum tunnelling composites.

- |                                 |                                |
|---------------------------------|--------------------------------|
| 1 – Gear wheel                  | 2 – Automatic level switch     |
| 3 – Switch holder               | 4 – Screwed metallic rod       |
| 5 – Cylindrical nut with groove | 6 & 7 – Nuts                   |
| 8 – Thick steel rod             | 9 – Upper Cu disk electrode    |
| 10 – Lower Cu disk electrode    | 11 – Stiff steel spring        |
| 12 or 22 – Copper cylinder      | 13 – Two parallel slim windows |
| 14 – Long slim gear             | 15 – Gear box                  |
| 16 – DC motor                   | 17 – Motor holder              |
| 18 – Top plate (Teflon)         | 19 – Big nut                   |
| 20 – Sample                     | 21 – Copper rod                |
| 23 – Steel tip stopper          | 24 – Iron rod                  |
| 25 – Primary coil               | 26 – Secondary coils           |
| 27 – Base plate (Teflon)        | 28 – Hard rubber feet          |
| 29 – Steel ball                 |                                |

## 3 WORKING MECHANISM OF THE INSTRUMENT:

At the initial position, the gear wheel (1) is located at the most upper end of the long slim gear (14). The upper copper electrode (9) is now free to be removed and the sample (20) is placed over the lower copper electrode (10). The two electrodes are made of copper with highly polished surfaces and have screws for fixing connection wires. The lower electrode (10) is welded to long copper rod (21) in which another soft iron rod (24) is fixed tightly. A stiff spring (11) hangs up the lower electrode (10) and its rods and keeps the iron rod inside a copper cylinder with thick mouth (12, 22). The whole system is fully software controlled. The power control signals and the data signals are delivered from and to a computer system through an USB multi-channel interface (National Instruments

model NI6009). The motor (16) is activated by a running signal from the interface through a high power relay. The gear box (15) reduces the motor speed and increases its torque, then the cylindrical gear (14) rotates the disk gear (1) which, in turn rotates the screwed rod (4) through a big fixed nut (5). The result of these rotations is vertical down displacement of the rod (4) causing compression on the sample. This compression is conducted to the spring (11) which is contracted (strained) by a distance that is linearly proportional to the exerted force on the sample. The soft iron rod (24) moves down a distance exactly equals the strain of the spring.

A small transformer excites the primary coil (25) that is wound around the copper cylinder (22) using 3 volts and 60 Hz. This alternating low voltage produces alternating magnetic field in the soft iron movable core (24). The movement of the core (24) transfers the magnetic lines of force to cross the secondary coil (26) and hence an induced voltage appears between terminals of the secondary coil (26). The induced voltage on coil (26) is proportional to the depth of rod (24) inside the coil due to the continuous increase in the number of coil turns (26) that are crossed by the iron core. Finally, voltage drop across terminals of coil (26) is directly proportional to the force acted on the sample and this voltage can be easily calibrated to obtain the force directly. The voltage across coil (26) is delivered to an analog input channel of the interface while the calibration relation is included in the controlling software so that the force is measured immediately. Introducing the sample surface area to the software enables the software to calculate and save the net pressure applied on the sample.

Electrodes (9) and (10) are connected to DC-power supply of constant output voltage  $V_{cc}$  as shown in the circuit diagram [1].

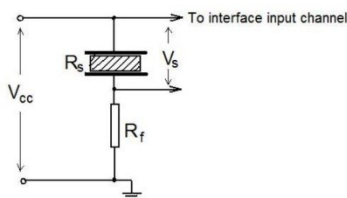


Figure 2: design of the circuit diagram 1

An interface input channel receives the voltage ( $V_s$ ) across the sample, while the current ( $I_s$ ) flows in the sample is calculated using the following relation:

$$I_s = \frac{V_{cc} - V_s}{R_f} \quad (1)$$

Where  $R_f$  is a constant resistance ( $25 \pm 0.01 \Omega$ ). Hence the sample resistance  $R_s$  could be calculated one by one, with sample rate of 10 Hz from the relation:

$$R_s = \frac{V_s}{I_s} = \frac{V_s \cdot R_f}{V_{cc} - V_s} \quad (2)$$

Upper and lower limits of some measured variables are hardware selected, which are:

1 – The DC motor speed, where the motor (16) is powered from external power supply across a potentiometer. The motor speed is controlled manually using a potentiometer.

2 – The force applied to the sample and the limits of the force are controlled by the stiffness of the spring (11) and it's allowed maximum compression strain. This strain is limited by the length of the window (13) that is grooved in the cylinder (12), and the steel stopper (23). The limits of applied force can be adjusted by exchange the spring only, where the maximum compressive strain is fixed.

3 - The applied pressure on the sample, where limits of applied pressure are controlled not only by limits of applied force but also by surface area of the sample. The diameter of the electrodes (9) and (10) is one inch (25.4 mm), hence the maximum surface area for the sample is 506.7 mm<sup>2</sup> and the smallest sample will be approximately  $4 \times 4 = 16 \text{ mm}^2$ . This means that the upper limit of the applied pressure can be over 30 times the lower limit according to the selected sample area. This technique is easy and fast for changing rang of applied pressure, since changing the force limits requires changing the spring and hence recalibrate the instrument.

4 – The total applied voltage  $V_{cc}$ , where its value is taken constant through a run; it can be adjusted from the source. The total applied voltage may be alternating with selectable frequency if the capacitive effect of the sample under variable pressure was a task.

#### 4. TECHNICAL MEASURES FOR HIGHER PERFORMANCE:

Some measurements have been considered to enhance the performance of the instrument;

1 – *Pressure release*: as the force acted on the sample reaches its maximum value, which is pre-identified through software, as the motor (16) is stopped and reverses the rotation direction. The steel stopper (23) is introduced in the instrument to force the motor to stop in case of software or computer failure. During the pressure release, the software continues data recording. This feature helps to detect the pressure – resistance hysteresis, which provides important knowledge about the electro – mechanical behaviour of the tested QTC samples.

2 – *Best insulation*: Teflon thick plates are used as very good insulator to prevent leakage of electric currents through movable or fixed parts of the instrument. General view of the instrument shows that the instrument is divided into two main parts, above each other separated by the sample only.

3 – *Smoothing the motion*: A small lubricated steel ball (29) is placed between the rotating screw bar (4) and the upper electrode (9) to prevent rotation of the electrode and to keep the force directed downward for always.

#### 5. TESTING THE INSTRUMENT

This instrument is designed and assembled specially to measure the electro-mechanical properties of any quantum tunnelling composites (QTC). In order to test the efficiency and performance of this instrument, it was essential to prepare a QTC samples and measure their physical properties.

### 1 – QTC samples preparation:

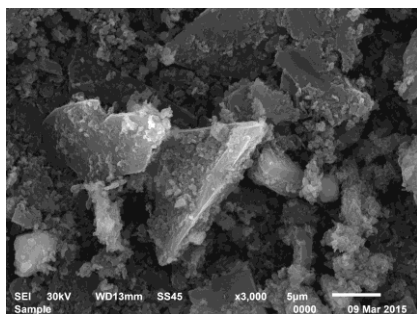
The common structure of a QTC is polymer-metal composite, or in more general consideration is polymer – conducting solid composite. The widely used polymer for QTCs is silicon rubbers. They consist of poly-dimethyl siloxane (PDMS), curing agent, fillers and additives. After application, they are cross-linked by contact with atmospheric moisture releasing by-products in the process. Cross-linking starts with the formation of a skin on the surface of the applied silicon rubber and gradually works its way into the compound. Their outstanding weathering and aging resistance is the result of their special chemical properties. Commercial silicon rubber is used in this work as a host polymer. Graphite was selected as a conducting component.

Commercial graphite rods were crushed manually in a mortar as trial to produce fine particles (flakes) with acute tips that may be equivalent to the spikes of other metals. Silicon rubber was mixed manually with different amount of graphite flakes to produces composite with different silicon rubber to graphite ratios (1:0.75, 1:1, 1:1.5, 1:1.75 and 1:2) as a weight fraction. The produced mixtures were then casted into Teflon mould and left overnight for curing. Afterwards, the composites were cut into discs with dimensions of 24.5 mm diameter and 2mm thickness.

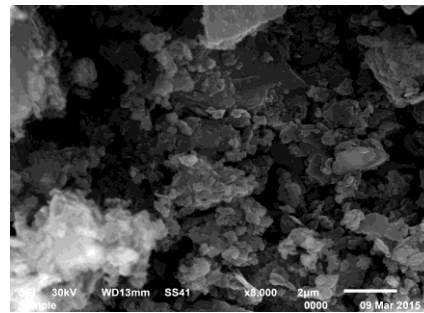
### Scanning electron microscopy (SEM):

Specimens were sputter-coated with gold and examined using a JEOL 6400 SEM at an accelerating voltage of 30 kV in secondary electron mode.

The SEM micrographs show the size and shapes of the used graphite powder (see figure 3).



(A)



(B)

Figure 3: SEM micrographs for the used graphite powder with two different magnifications.

Graphite flakes has range of sizes, ranged from submicron to several microns (~10µm). This wide range of sizes was attributed to the preparation method (i.e. manual crushing). It can be also observed that the flakes have irregular geometries with sharp tips which is essential for preparation of QTC.

These images show the sharp tips of the graphite fragments in both large and tiny fragments.

### 2 – Repeatability and accuracy of the instrument:

Two factors are indirectly affecting the electro – mechanical response of some QTCs; the rate of pressing and the maximum pressure acting on the sample.

#### a) The rate of pressing a sample:

The rate of pressing is directly proportional to the number of revolutions per minute (RPM) of the driving DC motor. The motor RPM is controlled manually from a power potentiometer. As the motor is excited by certain voltage, it rotates with a fixed speed unless its applied voltage is changed to another required value to acquire new speed, and so on. Many samples can be measured at the same pressing rate as long as the motor voltage is kept constant. By this feature, the electro – mechanical properties of different samples can be compared irrespectively to the effect of pressing rate. Figure 4 shows the determination method of the pressing rate, where the pressure is recorded as function of time through a complete cycle of pressing and releasing the sample, then the pressing rate was determined as (dp/dt) gradient. Figure 4 shows also that the pressure, acted on the sample is exactly linear with time, especially at higher speeds of the motor. At low speed, the little non-linearity is due to the mechanism of changing the motor speed. The RPM is reduced by lowering the driving power of the motor, while the mechanical resistance (stiffness of the spring (11) in Figure 1) still linear. The little shift from the zero point on the pressure axis in figure 4 was suggested to be due to the initial low pressure acted on the sample by the weight of the upper thick electrode (9) in figure 1. Figure 4 shows also the accuracy of the mechanical system in verifying the selected maximum pressure regardless to the selected pressing rate.

#### b) b. Selection of maximum applied pressure:

Most of QTC applications are sensing applications, where the sensing property of the sensor should be reversible. In the case of sensors for mechanical variables (force, pressure, strain,...etc), the applied stress to the sensing material should not exceed the yield point of the material. Therefore, the maximum pressure or force that applied on the sample during measurements should be adjustable either by the measuring hardware or the controlling software.

At this point, it should be differentiated between two maxima of pressure. The first is the maximum pressure can be applied by the instrument, which is determined by the stiffness and length of the spring (11) (see Figure 1). The second maximum pressure is that selected to be applied on the sample during a specific run. Therefore, the maximum pressure through a run is always less than the maximum pressure by the instrument. Figure 5 shows the pressure applied to a sample versus time for different runs each at different selected maximum pressure.

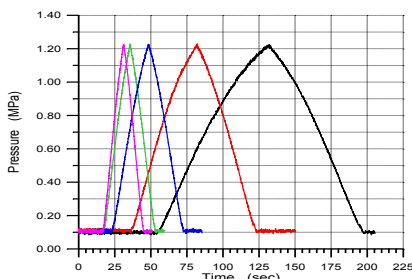


Figure 4: The applied pressure versus time at Different pressing rates and the same selected maximum pressure.

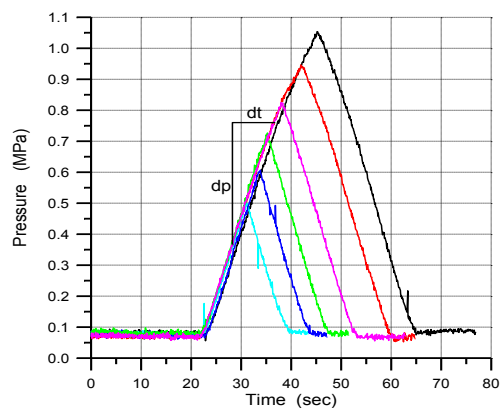
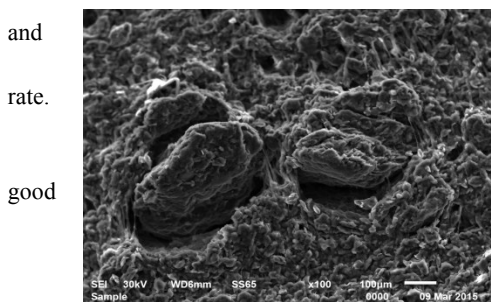


Figure 5: Applied pressure against time at different maximum pressure



repeatability of the pressing rate regardless the selected

maximum pressure. In the current instrument, the maximum pressure during a run is software selected.

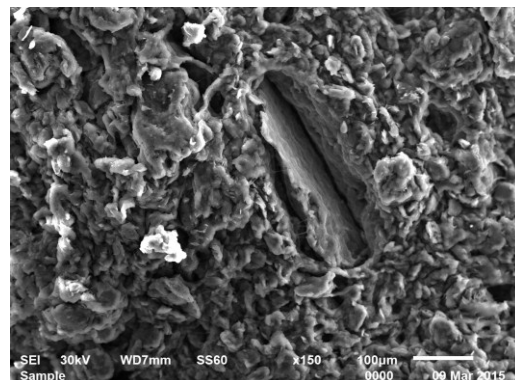
Now the instrument is qualified to be used satisfactorily for characterizing the electro-mechanical properties of quantum tunnelling composites

## 6. CASE STUDY:

Two kinds of piezoresistive composites should be distinguished based on the conduction mechanism through the dispersed phase. The former composite type, also known as pressure conductive rubber, exhibits a variation of the electrical conduction in response to a mechanical deformation, as a consequence of the contact change among the conductive particles. To describe the formation of conductive paths under external load, originated by intimately contacted particles, different percolation models have been proposed [4, 5].

Generally, these models fail below the percolation threshold where they predict that the composite is an insulator. The latter piezoresistive composite type (known as quantum tunnelling composite, QTC) show a conduction mechanism that can be well represented by field assisted Fowler-Nordheim tunnelling model, where the filler particles are well separated and being fully coated with the insulating polymeric matrix [6].

The prepared composites were used in the following study. Figure 6 represents SEM micrographs for silicon rubber/graphite composites showing the fully coating of graphite flakes with silicon rubber. Therefore, there is no potential for percolation to occur.



(b)

- a) Figure 6: SEM micrographs for silicon rubber/graphite composites with different compositions; (a) 1 : 2 and (b) 1 : 1.5. Graphite particles are imbedded and fully coated with the polymer matrix where

The automatic dynamic measurement of the QTC was used to record the sample current  $I_s$  during the continuous increase in the applied pressure at different pressing rates. Figure 7 illustrates change in  $I_s$  against applied pressure. Some remarkable notes can be drawn from this curve:

- a) The sample current and resistance are independent on the pressing rate. This statement appears in contrast with a well-

known viscoelastic concept, where the material shows more stiffness at faster rates of load application and vice versa. In fact, the current case is somewhat differs than the viscoelastic concept because the time interval between pressing and releasing is significantly shorter (see figure 5) than the mechanical relaxation time of the sample. In the current study, the relaxation process was measured statically and results can be seen in figure 8. Figure 8 shows that increasing the graphite content (filler concentration) causing increase in the stiffness of the sample and accordingly, the mechanical relaxation time decreased.

- b) Figure 7 also demonstrates good accuracy and repeatability in measurement of the sample current.
- c) The little fluctuations in Figure 7 was ascribed to non-homogenous distribution of graphite flakes within the specimens.

For some applications, the decay of sample current at removing of pressure is as important as the current growth during pressing. Therefore, it was necessary to record the current hysteresis (loading and unloading). The suggested low cost setup able to record the current flows in the sample during both stages of loading and unloading. From Figure 9, turn point of the pressure can be seen and highlighted inside the blue circle. It is clear that the current dropped exactly at the turn point of pressure and soon its value is recovered. Finally, it decayed as fast as the pressure decreased. The question arises here is; what is the source of charges that are compensated the blockage of charge flow due to the sudden increase of resistance at the turn point? The increase of current at the tipping point may be due to the capacitance of the sample between conductive electrodes. Chen *et al.* [7] cleared that the contact resistance of the electrodes  $R_e$  is negligible and then the sample may be considered as a parallel connection of a variable resistance and a variable capacitor (see Diagram 2). Therefore, it was essential to confirm this deduction by measuring the effect of capacitive feature of the sample on the measured sample current under different loads.

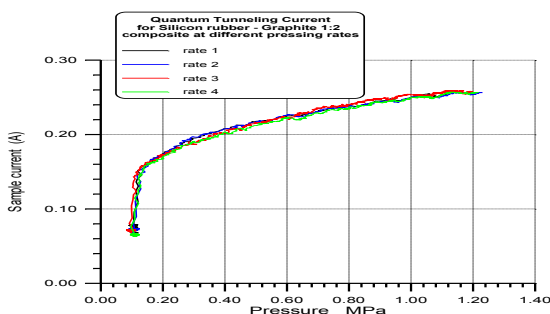


Figure 7 : Sample current as function of the applied pressure for 1 : 2 rubber : graphite composite.

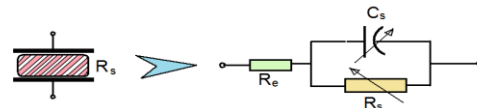


Diagram 2: The equivalent circuit diagram of the sample

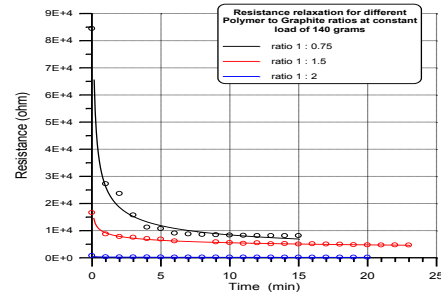


Figure 8: The relaxation of sample resistance for silicon rubber/graphite with different compositions under a constant load of 140 grams

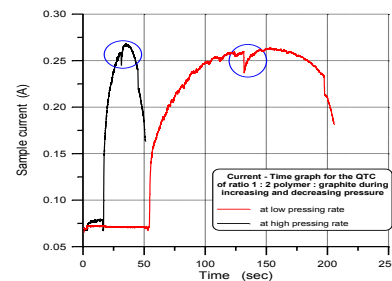


Figure 9: Current vs. time graph for the QTC of ratio 1 : 2 composite during loading and unloading stages at high and low rates showing the turn point.

Figure 10 shows the capacitance of the produced QTC with ratio of 1 : 1 at different applied loads. The capacitance was measured by a digital multi-meter while the sample was under static load. The readings were recorded after complete relaxation of the sample. As the load increased from 0.3 to 2.6 kg, the capacitance of the composite increased gradually (approximately linearly) from 25 $\mu$ F to reach 200 $\mu$ F at the load of 2.6kg. Figure 11 also demonstrates the change in capacitance against applied load for composites with higher rubber to graphite ratios. Comparing the load ranges and the corresponding change of capacitance in Figures 10 and 11, It can be deduced that composites with higher graphite concentrations possess higher sensitivity for capacitance change under loading, even if they have higher thickness. This was attributed to the existence of high amounts of conducting particles (graphite). Figures 10 & 11 show also that at zero load (un-deformation) the samples showed very low capacitance which started to increase by applying a load. This means that the QTC has a potential to be used as a pressure variable condenser.

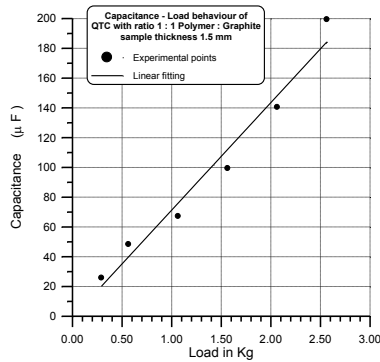


Figure 10: Change in the specimen capacitance versus load for composites of 1 : 1 ratio and 1.5 mm initial thickness.

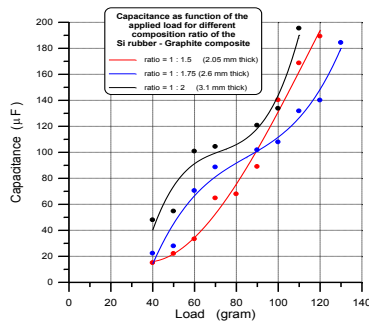


Figure 11: Capacitance as function of the applied load for different composition ratio of the silicon rubber - graphite composites

Changes in sample capacitance ( $C_s$ ) means changes in its reactance ( $X_s$ ), where  $X_s = 1/\omega C_s = 1/2\pi f C_s$  ( $\omega$  is the angular frequency and  $f$  is the frequency of applied voltage). Consequently, the sample current should also depend on the frequency of applied voltage. Change in sample currents against frequency for composites two different graphite concentrations at different loads is shown in Figure 12 and 13. These graphs clarify the current dependence on  $f$  and  $X_s$  separately. The position of a curve belongs to the effect of  $X_s$  by the applied load, while the trend of each curve belongs to the effect of the frequency of the applied voltage. Figure 13 shows that at higher graphite concentrations, the effect of different loads is minimized while the effect of frequency is sharpen up.

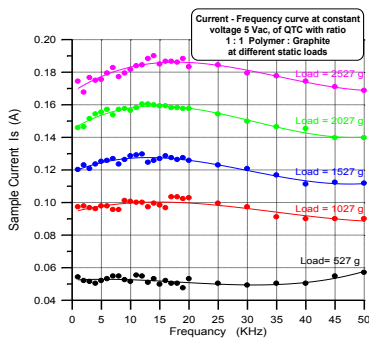


Figure 12: Sample current versus frequency of applied voltage to QTC with 1:1 ratio at different mechanical loads.

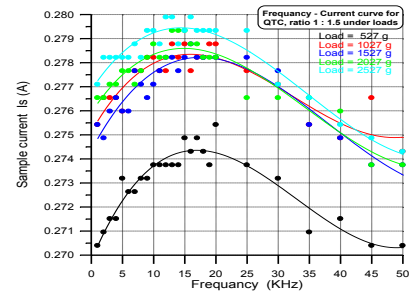


Figure 13: change in sample current against frequency of applied voltage to 1:1.5 composite at different mechanical loads.

## 7. CONCLUSION:

Carbon materials such as graphite, carbon black (CB) and carbon nano-tubes (CNTs) are widely used as fillers in conductive polymer composites due to low density and high conductivity. Many studies have recently demonstrated that polymers especially soft elastomers incorporated with these conducting fillers could show significant piezoresistive performance [8]. A low cost technique was introduced in this study to carry out most of the required measurements in order to characterize the electro-mechanical properties of QTC using both DC and AC applied voltage. The suggested setup provided a stream of data presenting many physical parameters with satisfactorily accuracy and repeatability. This data stream should be very helpful guide for scientists whom interested in developing QTC and modelling the process of quantum tunnelling in metal based composites.

## 8. REFERENCES:

- 1 - [www.nanolab.unimore.it](http://www.nanolab.unimore.it)
- 2 - D. Bloor, A. Graham, E. J. Williams, P. J. Laughlin, and D. Lussey, "Metal-polymer composite with nanostructured filler particles and amplified physical properties," *Applied Physics Letters*, vol. 88, no. 10, pp. 102103-102103-3, Mar. (2006).
- 3 - YWR Amarasinghe, AL Kulasekera, TGP Priyadarshana, Seventh International Conference on Sensing Technology, (2013)
- 4 - Hussain M., Choa Y.-H., Niihara K. "Conductive rubber materials for pressure sensors." *Journal of Materials Science Letters*, 20, pp. 525- 527 (2001)
- 5 - Ding T., Wang L., Wang P. "Changes in electrical resistance of carbon-black-filled silicone rubber composite during compression." *Journal of Polymer Science Part B: Polymer Physics*, 45, pp. 2700-2706 (2007)
- 6 - S. Stefano, G. Canavese, F. Cosiansi, M. Cocuzza, "An innovative Copper-PDMS Piezoresistive composite for

flexible tactile sensor” The  
15th EUROPEAN CONFERENCE ON COMPOSITE  
MATERIALS,  
Venice, Italy, 24-28 June (2012)

7 - Qian Chen, Yingying Sun, Ying Wang, Hongbin Cheng,  
Qing-Ming  
Wang, “ZnO nano-wires–polyimide nano-composite  
piezoresistive strain  
sensor”, *Sensors and Actuators A* 190, pp. 161– 167(2013)

8 - Wenting Cai, Ying Huang, Dayue Wang, Caixia Liu,  
Yugang  
Zhang, “Piezoresistive Behaviour of Graphene Nano-  
platelets/ Carbon  
Black/ Silicone Rubber Nano-composite” *J. APPL. POLYM.  
SCI.*  
(2013), DOI: 10.1002/APP.39778